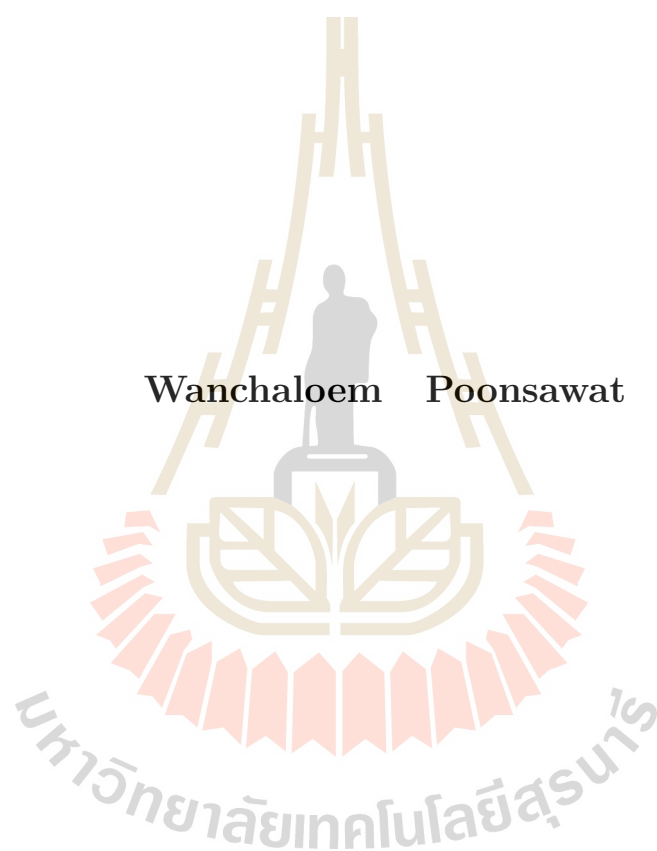# DETECTOR RESPONSE SIMULATION OF

THE ALICE ITS UPGRADE AT CERN

Wanchaloem   Poonsawat

A Thesis Submitted in Partial Fulfillment of the Requirements for the

Degree of Doctor of Philosophy in Applied Physics

Suranaree University of Technology

Academic Year 2018

การจำลองการตอบสนองระบบตรวจวัดชั้นในที่ปรับปรุงใหม่
ของหัววัดอลิซที่เซิร์น

นายวันเฉลิม พูนสวัสดิ์

DETECTOR RESPONSE SIMULATION OF

THE ALICE ITS UPGRADE AT CERN

Suranaree University of Technology has approved this thesis submitted in partial fulfillment of the requirements for the Degree of Doctor of Philosophy.

Thesis Examining Committee

_____

(Assoc. Prof. Dr. Sirichok Jungthawan)

Chairperson

_____

(Prof. Dr. Yupeng Yan)

Member (Thesis Advisor)

_____

(Asst. Prof. Dr. Chinorat Kobdaj)

Member

_____

(Asst. Prof. Dr. Ayut Limphirat)

Member

_____

(Asst. Prof. Dr. Pornrad Srisawad)

Member

_____

(Prof. Dr. Santi Maensiri)

Vice Rector for Academic Affairs

and Internationalization

_____

(Assoc. Prof. Dr. Worawat Meevasana)

Dean of Institute of Science

วันเฉลิม พูนสวัสดิ์ : การจำลองการตอบสนองระบบตรวจวัดชั้นในที่ปรับปรุงใหม่ของหัววัดอลิซที่เซิร์น (DETECTOR RESPONSE SIMULATION OF THE ALICE ITS UPGRADE AT CERN) อาจารย์ที่ปรึกษา : ศาสตราจารย์ ดร.ยูเป็ง แยน, 109 หน้า.

เป้าหมายของความร่วมมือกับ ALICE คือการศึกษาฟิสิกส์ของสสารที่มีปฏิสัมพันธ์อย่างแรง โดยใช้ผลการทดลองจากเครื่องตรวจจับไอออนหนัก Inner Tracking System (ITS) ซึ่งตั้งอยู่ในใจกลางของเครื่องตรวจจับ ALICE ในปัจจุบัน ALICE กำลังวางแผนที่จะปรับปรุง ITS สำหรับการวัดอนุภาคหายากที่มีโมเมนตัมตามขวางต่ำ โดย ITS ใหม่จะประกอบด้วยเซ็นเซอร์ชนิดซิลิคอนพิกเซลจำนวนเจ็ดชั้นบนโครงสร้างรองรับ เป้าหมายหนึ่งของการปรับปรุงคือการลดงบประมาณวัสดุ (X/X_0) ต่อชั้นให้เหลือเพียง 0.3% สำหรับชั้นในและ 0.8% สำหรับชั้นกลางและชั้นนอก ในวิทยานิพนธ์นี้ เราจะทำการจำลอง ITS โดยใช้รายละเอียดทางเรขาคณิตของโครงสร้างรองรับต่าง ๆ สำหรับส่วนตรวจวัดชั้นในและชั้นนอกโดยใช้โปรแกรม ALIROOT ที่ทำงานบนระบบ ROOT ซึ่งเป็นองค์ประกอบพื้นฐานที่ใช้สำหรับการจำลองการสร้างใหม่และการวิเคราะห์ จากผลการวิจัยระบุว่า สามารถลดงบประมาณวัสดุของส่วนตรวจวัดชั้นในและชั้นนอกให้เป็นไปตามค่าคาดการณ์สำหรับการผลิตต้นแบบดังกล่าวได้

ประการที่สอง ชั้นตรวจวัดจะได้รับการปรับปรุงเพื่อให้สามารถแสดงผลการติดตามทางเดินอนุภาคได้ดีขึ้น โดยยังคงมีค่าความละเอียดที่สูงและงบประมาณวัสดุที่ต่ำ จากความต้องการดังกล่าว นำไปสู่การใช้เทคโนโลยีเซ็นเซอร์แบบพิกเซลที่เรียกว่า Monolithic Active Pixel Sensors (MAPS) MAPS เป็นเซ็นเซอร์ที่สร้างขึ้นด้วยการรวมส่วนตรวจจับและระบบอ่านสัญญาณไว้ด้วยกัน โดย MAPS ได้รับการเสนอให้เป็นเซ็นเซอร์ในการตรวจจับอนุภาคพลังงานสูงที่มีประสิทธิภาพและมีความสำคัญอย่างยิ่ง ข้อมูลที่ได้จากการทดสอบจะถูกนำมาปรับปรุงเพื่อให้ได้เซ็นเซอร์ที่มีประสิทธิภาพตรงตามที่กำหนด โดยการทดสอบคุณลักษณะเฉพาะทางไฟฟ้าด้วยแหล่งกัมมันตภาพรังสีและลำอนุภาคโปรตอนพลังงาน 6 GeV จากการทดสอบแสดงให้เห็นว่า เซ็นเซอร์ดังกล่าวมีคุณสมบัติสอดคล้องกับความต้องการของ ALICE โดยเซ็นเซอร์ต้นแบบแรกที่มีขนาด 1.5×3.0 ตารางเซนติเมตร จะถูกผลิตเพื่อนำไปติดตั้งและทดสอบในช่วงการปิดปรับปรุงของเครื่องตรวจจับ ALICE ต่อไป

สาขาวิชาฟิสิกส์

ปีการศึกษา 2561

ลายมือชื่อนักศึกษา _____

ลายมือชื่ออาจารย์ที่ปรึกษา _____

ลายมือชื่ออาจารย์ที่ปรึกษาร่วม _____

WANCHALOEM POONSAWAT : DETECTOR RESPONSE
SIMULATION OF THE ALICE ITS UPGRADE AT CERN. THESIS
ADVISOR : PROF. YUPENG YAN, Ph.D. 109 PP.

DETECTOR MODELLING AND SIMULATIONS/ PARTICLE TRACKING
DETECTORS (SOLID-STATE DETECTORS)

The aim of the ALICE Collaboration is to study the physics of strongly
interacting matter by using the experimental results from a dedicated heavy-ion
detector. The Inner Tracking System (ITS) is located at the heart of the AL-
ICE detector surrounding the interaction point. Currently, ALICE is planning
to upgrade the ITS for rare probes at low transverse momenta. The new ITS
comprises seven layers of silicon pixel sensors on the supporting structure. One
goal of the new design is to reduce the material budget (X/X_0) per layer to 0.3%
for the inner layers and 0.8% for the middle and outer layers. In this thesis, we
firstly perform simulations based on detailed geometrical descriptions of different
supporting structures for the inner and outer barrels by using ALIROOT. This is
a fundamental framework used for simulation, reconstruction and analysis.. Our
results indicate that it is possible to reduce the material budget of the inner and
outer barrels to the expected value. Manufacturing of such prototypes is also
possible.

Secondly, the detection layers have been upgraded for the better tracking
peformance with high spatial resolution and low material budget. The require-
ment lead us to the pixel sensor technology called Monolithic Active Pixel Sensors
(MAPS). MAPS are image sensors built with on-chip integration of sensors and
a signal readout system. MAPS have recently been proposed as sensors to detect
high energy particles and their performance, critical to obtained information, must

be tested and improved to meet desired specifications. The sensors have been measured using radioactive sources and proton beam of 6 GeV. The results indicate that the sensors satisfy the ALICE requirements and first prototypes with the final size of 1.5×3 cm^2 have been produced for the LS2. The results will be used for improvement of sensor performances.
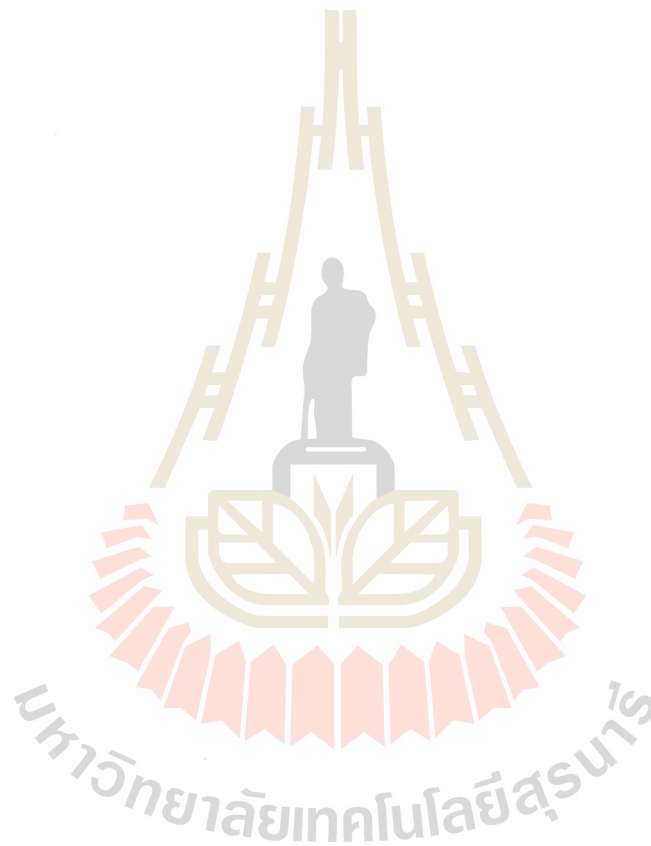
School of Physics

Academic Year 2018

Student's Signature _W. Poonsawat_

Advisor's Signature _____

Co-advisor's Signature _C. Kobdaj_

ACKNOWLEDGEMENTS

Wanchaloem Poonsawat

CONTENTS

CONTENTS (Continued)

CONTENTS (Continued)

CONTENTS (Continued)

LIST OF TABLES

LIST OF TABLES (Continued)

LIST OF FIGURES

LIST OF FIGURES (Continued)

LIST OF FIGURES (Continued)

LIST OF FIGURES (Continued)

LIST OF FIGURES (Continued)

LIST OF FIGURES (Continued)

LIST OF ABBREVIATIONS

ALICE   A Large Ion Collider Experiment

LHC   The Large Hadron Collider

CERN   the European Organization for Nuclear Research

QGP   Quark-gluon plasma

QCD   Quantum chromodynamics

ITS   Inner Tracking System

MAPS   Monolithic Active Pixel Sensors

O^2 ALICE Online and Offline Computing to a new common system

SPD   Silicon Pixel Detector

SDD   Silicon Drift Detector

SSD   Silicon Strip Detector

IP   Interaction point

SRP   Spreading Resistance Profiling

HIC   Hybrid Integrated Circuit

MIPs   Mminimum ionizing particles

MCCE   Matrix charge collection efficiency

MPV   Most Probable Value

V_{BB} Reverse bias voltage

CHAPTER I

INTRODUCTION

ALICE (A Large Ion Collider Experiment) is a detector located in the Large Hadron Collider (LHC) at CERN. ALICE is the experiment in heavy-ion collisions designed to study Quark-Gluon Plasma (QGP), which is a deconfined state of strongly interacting Quantum Chromodynamics (QCD) matter. The strong interaction ensures the stability of ordinary matter, confining quarks into hadron particles, such as the proton and neutron, the largest components of the mass of ordinary matter. Hadron is made of quarks held together by the strong force. They are categorized into two families: baryons, made of three quarks, and mesons, made of one quark and one antiquark. There are six types of quarks, known as flavors: u, d, s, c, t, and b. Up (u) and down (d) quarks have the lowest masses of all quarks. Because of this, u and d quarks are generally stable and the most common in the universe, whereas s, c, b, and t quarks can only be produced in high energy collisions. That is a reasonable challenge to study the heavy quarks of the ALICE detector at CERN. CERN is the European Organization for Nuclear Research which has the largest particle physics laboratory in the world, the Large Hadron Collider (LHC). LHC consists of four particle detectors; one is ALICE. A Large Ion Collider Experiment (ALICE) is designed to study Quark-Gluon Plasma (QGP), deconfined state of strongly interacting Quantum Chromodynamics (QCD) matter.

ALICE detector consists of eighteen systems. In this work, we focus on a central part of the ALICE detector called the Inner Tracking System (ITS)

consists of six silicon vertex detector layers. The main duty of ITS is aimed to detect the primary vertex and the secondary vertices where the unstable heavy particles decay after a flight distance of some hundreds of micrometers. Because of the high particle density at the vertex, the four innermost layers need to be high-resolution devices which record both x and y coordinates for each passing particle (Evans, 2009).

In this chapter, an overview of ALICE and its detectors, focusing on ITS and the ALICE software will be given.

1.1   ALICE detector

A Large Ion Collider Experiment (ALICE) is designed to study a deconfined state of strongly interacting matter. There are eighteen systems within the ALICE detector (as shown in Figure 1.1), but in this work, we are interested in the central part of the ALICE detector called the Inner Tracking System (ITS). The present ITS is composed of six layers exploiting three different silicon technologies. The main purpose of the ITS is to detect the primary (collision location) and secondary vertices (decay location of some unstable heavy particles after a flight distance of some hundreds of micrometers). The innermost layers are required to be high-resolution devices to record with the highest precision the coordinates of the points crossed by each passing particle (Evans, 2009).

The precision of the present ITS for detecting charm mesons is insufficient at low transverse momenta (< 1 GeV/c) and also for charm baryons. In the case of a charm baryon, the lowest-mass charm baryon is Λ_c with a rest mass of 2286.46 ± 0.14 MeV/c^2 (Nakamura et al., 2010). The important decay channel of its measurement is the decay of $\Lambda_c \to pK^-\pi^+$ with $5.0 \pm 1.3\%$ of branching ratio. The mean proper decay length ($c\tau$) of Λ_c is only 60 μm that is shorter than
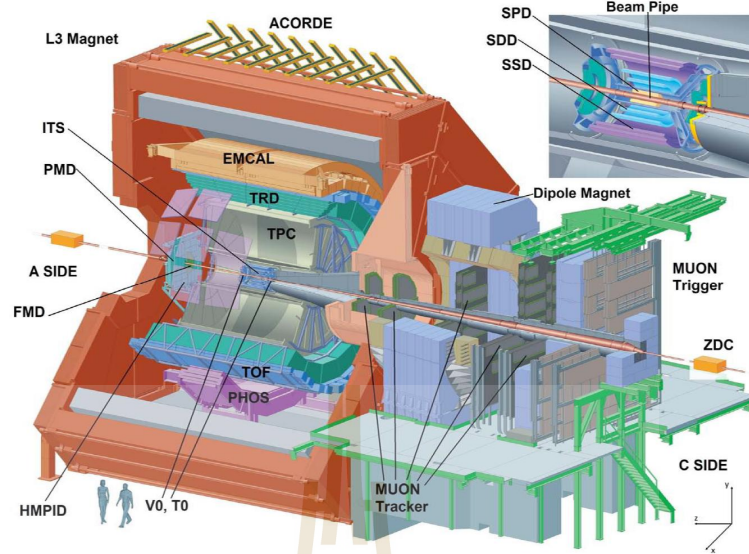
Figure 1.1 Layout of the ALICE apparatus (ALICE Collaboration, 2012)

the impact parameter resolution of the present ITS. Therefore, charm baryons are only partially accessible by the ALICE detector in central Pb–Pb collisions.

Current measurements of Pb–Pb collisions are characterized by a very small signal-over-background ratio, which requires large statistics. Thus, to achieve the goal of heavy quark measurement, the ALICE ITS must be upgraded (ALICE Collaboration, 2012).

1.2 ALICE software

The main task of the offline project of the ALICE experiment is to reconstruct and analyze data coming from real or simulated collisions. This is performed using programs based on Object-Oriented techniques. The software environment introduced in 1998 for the ALICE offline project is called AliRoot and is based on the ROOT framework. ROOT is an Object-Oriented program written in C++ language, and its architecture consists of about 650 classes. The ROOT structure is specifically designed to cope with vast amounts of data coming from high energy

physics experiments. For this reason, ROOT provides the packages which perform
the event generation, the detector simulation, the event reconstruction, the data
analysis, as it will be discussed in the following section. ALIROOT was developed
as an extension of ROOT to include the geometry of the detectors, their typology,
and their response to the passage of particles. In addition, AliRoot provides the
tools for the local reconstruction and analysis of each detector. The schematic of
the AliRoot framework is shown in Figure 1.2.
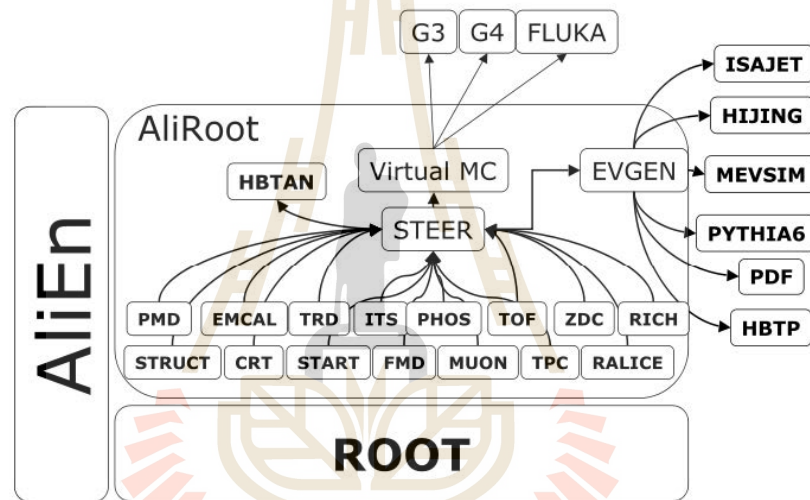
Figure 1.2 The AliRoot design architecture (Berzano, 2015)

This thesis is organized as follows: Chapter I gives an overview of ALICE
ITS; in Chapter II, the ITS upgrade details and requirement will be explained;
in Chapter III, the measurement of material budget for the new ITS prototypes
will be presented; Chapter IV describes the physics of pixel detectors with par-
ticular emphasis on Monolithic Active Pixel Sensors (MAPS); in Chapter V, the
development of TowerJazz 180 nm CMOS sensor technology for the ALICE pixel
detector (ALPIDEf) will be explained; Chapter VI presents the results obtained
in the laboratory and proton beam test at CERN on the pALPIDE-3 prototype;

Chapter VII concludes the thesis work giving a summary on what we have done and the plans for the future work.

The summary of this work has been presented in the Figure 1.3.
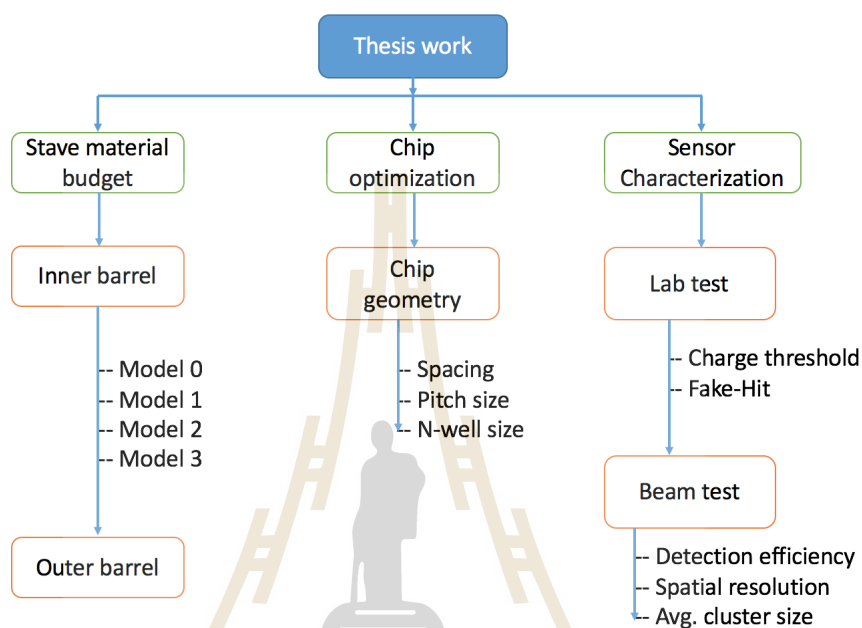
Figure 1.3 Summary of thesis work

CHAPTER II

ALICE INNER TRACKING SYSTEM UPGRADE

The ALICE detector will be upgraded to improve their physics capabilities during the second long shutdown in 2019-2020. The main purpose of the upgrade is to enhance the precision of rare processes measurement at low transverse momentum (low p_T). In this chapter, the upgrade schemes of the ALICE detector will be introduced with a focus on the Inner Tracking System (ITS). Moreover, the ITS upgrade requirement based on its design objective will be described.

2.1 The ALICE upgrade

The experiment data of Pb-Pb and p-Pb collision taking from ALICE can be used to confirm the results obtained from the other experiment, i.e., CERN SPS and BNL RHIC. Furthermore, these results show that the QGP is a strongly-coupled liquid plasma. Although the investigation of the ALICE detector is important, there are some issues that the present ALICE detector cannot figure out. Therefore, the ALICE subdetector will be optimized (ALICE Collaboration, 2014b). The main upgrades are as follow:

- Reduction of the new beampipe diameter

- ITS material improvement which allows the resolution increase by the factor of 3

- Replacement of the wire chambers with Gas Electron Multiplier (GEM) detectors and new pipelined read-out electronics of the Time Projection Chamber (TPC) to remove the TPC dead-time

- Optimization of Muon Forward Telescope (MFT) to increase more capabilities of vertex

- Upgrading of the read-out electronics to support high rate operation

- Upgrading of forwarding trigger detectors and analysis framework

- Upgrading of the online systems and offline computing system (O^2 project)

These upgrades will increase the luminosity up to 6×10^{27} cm$^{-2} \cdot$ s^{-1} related to the interaction rate of 50 kHz and cover more than 10 nb^{-1} of Pb-Pb collisions. However, in this thesis, we will focus on the hardware upgrade of the ITS that mainly affect the physics performance of the detector.

2.2   The Inner Tracking System

The Inner Tracking System (ITS) is the innermost tracking detector closed to the interaction point. It has several layers of silicon detector located at a minimum radius of 4 cm surrounded the beam pipe. The ITS competency are mainly to reconstruct the primary vertex of the collided particles carrying more than 1 GeV/c of transverse momentum and to identify the secondary vertices for D and B meson and hyperon decay process.

The current ITS (Figure 2.1) composes of 6 concentric barrels with three different technologies of sensor covers the vertices located within ± 60 mm from the interaction point ($|\eta| < 0.9$). The sensor technology used for the first two innermost layers is the Silicon Pixel Detector (SPD) which obtains the particle

with short decay length. For the next two layers equipped with Silicon Drift Detector (SDD) are provided for measurement of energy loss. Furthermore, two outer layers are designed to identify the type of particle which used of Silicon Strip Detector (SSD). More details were described as in (ALICE Collaboration, 2012).
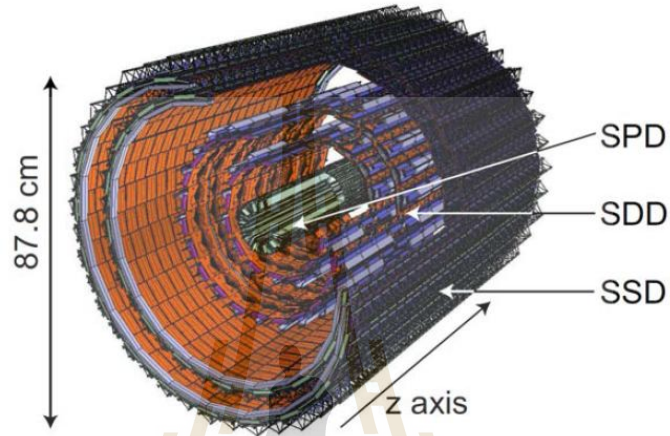
Figure 2.1 Layers of the present Inner Tracking System (ALICE Collaboration, 2012).

The precision of the present ITS determination of charm is insufficient at low transverse momentum (<1 GeV/c). In case of charm baryon, the lowest-mass charm baryon is the Λ_c with a rest mass of 2286.46 ± 0.14 MeV/c^2 (Nakamura et al., 2010). The most decay channel of its measurement is the decay of $\Lambda_c \to pK^-\pi^+$ with a branching ratio of 5.0 ± 1.3 % while its decay length, a key parameter of this context, is defined by

$$L = \beta c \tau \gamma, \tag{2.1}$$

where βc is the velocity of the decaying particle, τ is the proper lifetime, and γ is the Lorentz factor. Λ_c has a mean proper decay length (L) of only 60 μm. This length is lower than the impact parameter resolution of the current ITS in the low transverse momentum range where most of Λ_c daughter particles are produced

(Figure 2.2). Therefore, the charm baryons are presently not accessible by ALICE detector in central Pb-Pb collisions.

(a)   (b)
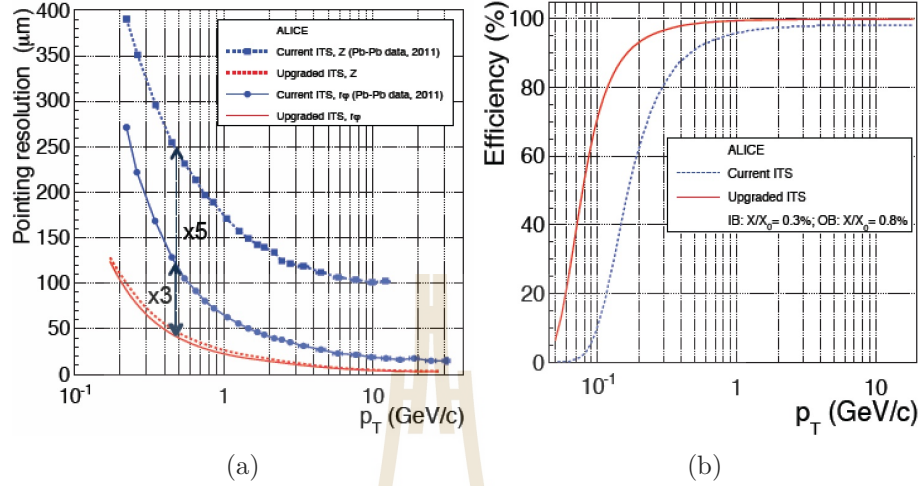
Figure 2.2 Performance of the current ITS in terms of (a) Pointing resolution and (b) Tracking efficiency as a function of transverse momentum compared to the expected performance of the upgraded ITS (ALICE Collaboration, 2014a).

Moreover, the collision rate delivered by the LHC is 8 kHz which more massive than the present ITS maximum read-out rate (1 kHz). In the case of the rare event that cannot be selected by the trigger, this establishes the limitation since the Pb-Pb collision luminosity is in contrast with the read-out rate of the detector. In order to overcome such limitation, the detector system must be located close to the interaction point which less than the decay lengths of the particles.

2.3 The ITS upgrade concept

The upgraded design is proposed to improve the tracking performance. Especially for inner barrel, a new layer is included as shown in Figure 2.3. This layer can increase the granularity for the innermost region. Moreover, the silicon sensor is replaced by Monolithic Active Pixel Sensors (MAPS). It will reduce the thickness of the detection layer. The optimized of new ITS inner barrel will allow

the overall material budget to be reduced.
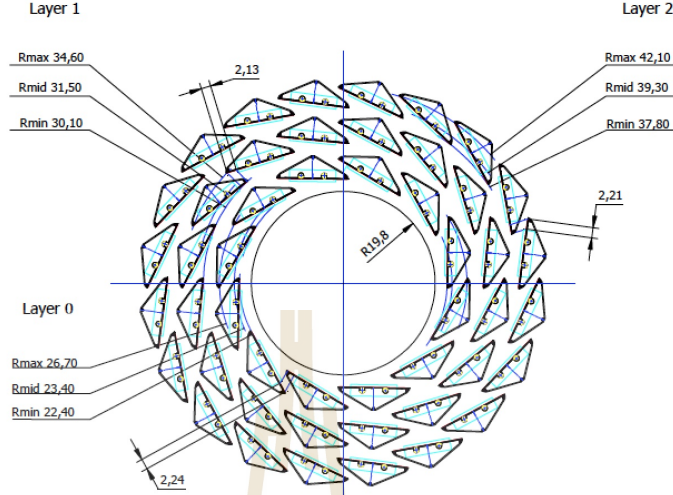
Figure 2.3 Layout of new ITS Inner Barrel (ALICE Collaboration, 2014a).

The objectives for the ITS upgrade are to provide more read-out rate for Pb-Pb and pp collisions and improve the pointing resolution of the physics events at transverse momentum $< 1\,\mathrm{GeV/c}$. The pointing resolution σ_p can be determined by the geometrical extrapolation error σ_p^x between the measured points along the particle's track and the interaction point (IP). It depends on the intrinsic resolution $\sigma_{x,i}$ and the range r of the detector.

The σ_p^x of two-layer detector can be defined by

$$\sigma_p^x = \sqrt{\left(\frac{r_2}{r_2 - r_1}\sigma_1\right)^2 + \left(\frac{r_2}{r_2 - r_1}\sigma_2\right)^2}, \tag{2.2}$$

where r_1 and r_2 are the radius of inner and outer layer, while σ_1 and σ_2 are the spatial resolution of these two detector.

The other parameter is the uncertainty (σ_p^{ms}) of multiple Coulomb scattering occurred in beam pipe and the detector layers close to IP. The deviation of pointing resolution will be deviated from zero points by multiple scattering because of the angle of deflection above the beam pipe radius. A particle tracking at angle

ϕ along the detection layer surface will be increased due to the increment of the amount of material and the radius. Thus, the contribution of multiple scattering for the uncertainty σ_p of a particle with unit charge can be written as

$$\sigma_p^{ms} \approx \frac{r_1}{sin^{3/2}\phi} \frac{13.6[MeV]}{\beta cp} \sqrt{x/X_0}. \tag{2.3}$$

Therefore, the pointing resolution σ_p can be obtained as below

$$\sigma_p \approx \sigma_p^x + \sigma_p^{ms}. \tag{2.4}$$

The Eq. (2.4) shows that the pointing resolution can be improved by reducing the inner radius (beam-pipe radius) and using the low material budget (X/X_0) for the innermost layer detector. Therefore, in the ITS upgrade, the simulation will be used to obtain the design parameters to be consistent with the physics objectives.

2.4   ITS upgrade requirement and design

In order to reach the physics performance for low transverse momentum range, the new ITS has to be designed as the following requirements (ALICE Collaboration, 2014a).

(I) The beam-pipe radius is reduced from 29 mm to 19 mm. It mainly affects the impact parameter resolution because the first detection layer can be located closer to the interaction point.

(II) Improved the ITS tracking efficiency by increasing the inner layer detector from 6 to 7. The present sensor will be replaced by Monolithic Active Pixel Sensors (MAPS) technology with new geometry optimization. This adoption will improve the impact parameter resolution of the new ITS.

Details of MAPS sensors will be given in the next chapter.

(III) The material budget will be reduced to $0.3\% X_0$ per layer for the three innermost layers and lower than $1.0\% X_0$ for the four outermost layers. To achieve the lower overall material budget, the MAPS technology sensors with 50 μm thickness will be used instead of the current detector. Moreover, its design is based on the low power consumption that allows the reduction of material budget distribution given by the cooling system. Furthermore, the pixel size will be reduced to around 30 μm × 30 μm.

(IV) The new ITS will be increased the maximum read-out rate from 1 kHz to 100 kHz in Pb-Pb collisions and 200 kHz in pp collisions consistent with the LHC luminosity.

The overall upgrade of the central barrel can improve the capabilities of vertexing and tracking of low p_T particles. Therefore, the physics performance of the detector is expected to be increased. As well as the measurements, they will be affected by the higher luminosity after the upgrade of ITS. The expected physics reach, in terms of pT interval and statistical uncertainties, for various measurements are summarized in Table 2.1.

In the next chapter, the details of optimizations according to this requirement and upgrade design will be significantly described.

Table 2.1 Summary of the physics reach foreseen after the ITS upgrade: minimum accessible p_T and relative statistical uncertainty in Pb-Pb collisions for an integrated luminosity of 10 nb^{-1}. For heavy flavour, the statistical uncertainties are given at the maximum between $p_\mathrm{T} = 2$ GeV/c and p_T^{min}. For elliptic flow measurements, the value of v_2 used to calculate the relative statistical uncertainty σ_{v_2}/v_2 is given in parenthesis. The case of the program up to Long Shutdown 2, with a luminosity of 0.1 nb^{-1} collected with minimum-bias trigger, is shown for comparison (ALICE Collaboration, 2014a).

Observable	Current, 0.1 nb^{-1}		Current, 10 nb^{-1}	
	p_T^{min} (GeV/c)	statistical uncertainty	p_T^{min} (GeV/c)	statistical uncertainty
Heavy Flavour				
D meson R_{AA}	1	10%	0	0.3%
D_s meson R_{AA}	4	15%	<2	3%
D meson from B R_{AA}	3	30%	2	1%
J/ψ from B R_{AA}	1.5	15%	1	5%
B^+ yield	not accessible		3	10%
Λ_c R_{AA}	not accessible		2	15%
Λ_c/D^0 ratio	not accessible		2	15%
Λ_b yield	not accessible		7	20%
D meson v_2 ($v_2 = 0.2$)	1	10%	0	0.2%
D_s meson v_2 ($v_2 = 0.2$)	not accessible		<2	8%
D from B v_2 ($v_2 = 0.05$)	not accessible		2	8%
J/ψ from B v_2 ($v_2 = 0.05$)	not accessible		1	60%
Λ_c v_2 ($v_2 = 0.15$)	not accessible		3	20%
Dielectrons				
Temperature (intermediate mass)	not accessible		-	10%
Elliptic flow ($v_2 = 011$)	not accessible		-	10%
Low-mass spectral function	not accessible		0.3	20%
Hypernuclei				
$^3_\Lambda H$ yield	2	18%	2	1.7%

CHAPTER III

ITS STAVE MODULE DESIGN AND

MATERIAL BUDGET CALCULATION

The upgraded ITS consists of Inner Barrel and Outer Barrel. Each barrel is located around the beam pipe. The ITS components consist of the mechanical supporting structure which provides the electrical frontend, the cooling system, and the sensitive layers. All components are designed under the purpose of optimizing the system which can reduce the overall material budget. In this chapter, some of the theoretical approaches and notation used for ITS staves material budget calculation will be described. The new ITS layout is shown in Figure 3.1.
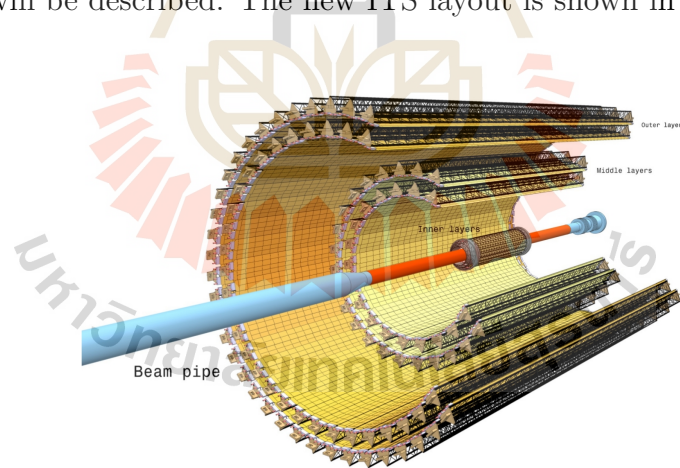
Figure 3.1 New ITS layout which consists of two innermost layers and four outer layers (ALICE Collaboration, 2012).

3.1 ITS barrel

Because of the reduction in the upgraded beam-pipe radius from 2.94 to 1.98 cm, it allows us to place the innermost layer closer to the interaction point. Hence, an extra layer is also introduced to increase the tracking efficiency of the new ITS. The new ITS has seven layers of the detector module. Each module called stave. The mechanical design of the new ITS has been focused on two different parts, inner barrel (layers 1 to 3) and outer barrel (layers 4 to 7), as seen in Figure 3.2, depends on the mechanical constraints. The design layout of the new ITS is shown in Table 3.1 with the expected material budget.
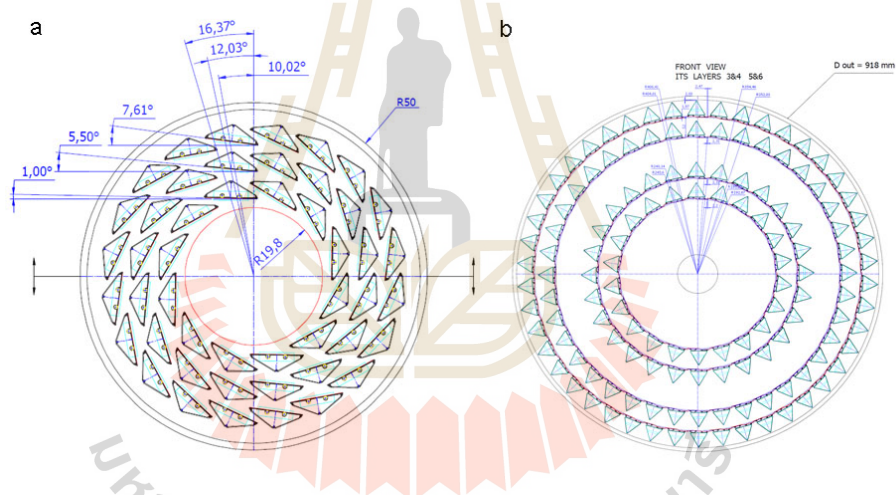
Figure 3.2 Schematic of cross-sectional layout of the inner barrel (left) and outer barrel (right) (ALICE Collaboration, 2014a).

The inner and outer barrel staves are positioned parallel to the beam direction and consist of the following components:

- Space Frame: a lightweight wound truss structure made of carbon fiber for mechanical support.

- Cold Plate: a carbon ply with embedded cooling units.

- Hybrid Integrated Circuit: an electronic circuit with a pixel sensor chip.

Table 3.1 Layout of the upgraded ITS inner barrel. The numbers in brackets refer to the case of the current detector.

Layer	Radius (cm)	Length (cm)	Material budget ($\%X_0$)
Inner barrel			
1-pixel (pixel)	2.2 (3.9)	22.4	0.3 (1.14)
2-pixel (pixel)	2.8 (7.6)	24.2	0.3 (1.14)
3-pixel (none)	3.6 (-)	26.8	0.3 (-)
Outer barrel			
4-pixel (driff)	20.0 (15.0)	78.0	0.8 (1.13)
5-pixel (driff)	22.0 (23.9)	83.6	0.8 (1.26)
6-pixel (strip)	41.0 (38.0)	142.4	0.8 (0.83)
7-pixel (strip)	43.0 (43.0)	148.6	0.8 (0.83)

The inner barrel (Figure 3.3) consists of nine pixel sensors connected to the electronics circuit. The cold plate and space frame is glued above the pixel chip. The stave material budget along the orthogonal direction is expected to lower than $1.14\%X_0$. The sensitive layer of the staves uses 50 μm thickness pixel sensors which are 20% of its total material budget.
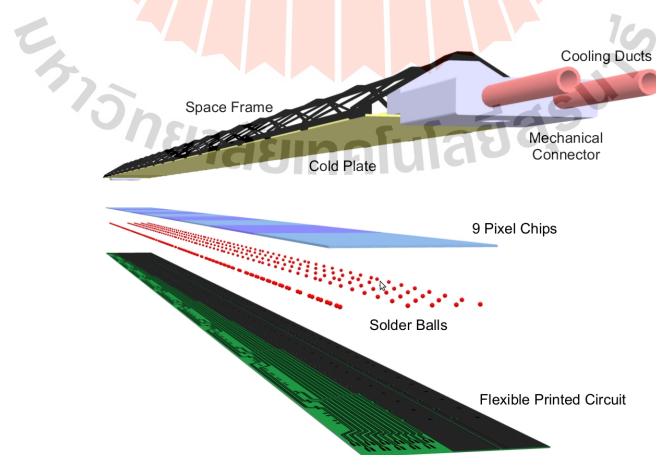
Figure 3.3 Representation of an inner barrel stave (ALICE Collaboration, 2012).

In Figure 3.4, the outer barrel stave has been presented. It has the same

structure but different of lengths. The outer barrel staves mainly difference compared to the inner barrel staves in the number of the sensitive row. They have divided azimuthally into two halves of seven chips which are approximately 3 cm wide and 21 cm long.
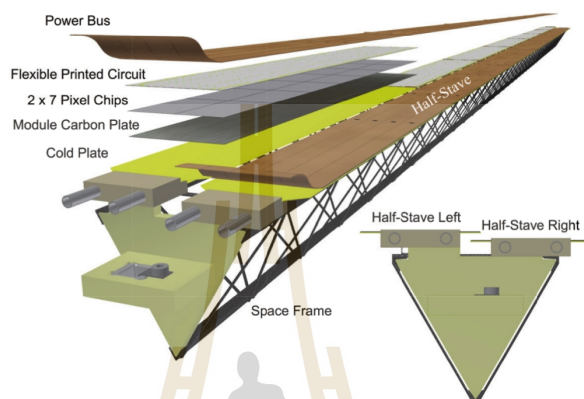
Figure 3.4 Representation of an outer barrel stave (ALICE Collaboration, 2014a).

In this work, both the inner and outer barrels have been studied for their material budget. The space frame of each stave is made of light filament-wound carbon. It is obtained by winding an M60J 3K (588 GPa) carbon rowing with respect to the stave axis with an angle of 45°. The winding angle and number of helices have been optimized to achieve the best compromise between the material budget and stiffness.

For the cooling system, a cold plate is used to remove the heat from sensors. The cold plate is made of a high thermally conductive carbon fiber laminate where the silicon chips are glued on top. The heat is conducted into the cooling pipes or microchannel embedded in the cold plate and is removed by the coolant. In order to maximize the cooling efficiency, the cold plates have been considered in four different models for the various geometrical designs and thermal constraints. The details of the mechanical structure design and the alternately cooling system

can be shown in the next section.

3.2 New stave design of upgraded ITS

The mechanical support structure is designed under technical constraints such as the detector layout, specific sensor chip size, and cooling technology requirements. The stave support structures have been categorized with different cooling technology as follows:

- Model 0: The wound truss structure with cooling pipes at the vertices

The winding carbon filaments with a diameter of 5 mm are used to construct the support structure. K13D2U is used for the wound truss structure instead of the M55J 6K carbon fiber for better thermal conductivity of the two embedded pipes, as shown in Figure 4.4(a). The use of the K13D2U carbon type can reduce the bending radius against the M55J 6K. The carbon fibers are wound with an angle of 23° along the stave axis to reduce the breaking of the production process. This prototype can reduce the weight of the structure while preserving a good stiffness. The pyramidal structure made by the carbon fiber filaments will be sufficiently strong to support the silicon sensors and the layer structure. The overall structure is suitable for low power consumption.

- Model 1: The wound truss structure with polyimide microchannel cooling

For this model, the same technique described for the wound truss structure has been used, but the cooling pipes have been replaced by a cold plate for a better heat distribution transferring over the pixel chip. A monophase or biphase refrigerant fluid is used in the cold plate flowing into 0.16 mm^2 of the polyimide microchannel cooling section (see Figure 4.4(b)).

- Model 2: The wound truss structure with a uniform carbon plate and poly-
  imide tubes in the middle

This model, obtained with the same technology described above, uses a uni-
form carbon plate for transferring heat to two embedded tubes. These polyimide
tubes are placed in the middle at the base of the stave structure. However, the
addition of a carbon plate may cause an increase in the amount of material.

In this model, two different outer radii, 0.15 and 0.10 mm, of the cool-
ing pipes are separately simulated for the material properties (see Figures 3.5(c)
and 3.5(d)).

- Model 3: The wound truss structure with the silicon microchannel

This model is the wound truss structure with the cold plate, made of a sil-
icon substrate (see Figure 3.5(e)). Based on etching technology, the microchannel
can be created on the silicon plate where the cooling fluid flows inside. The mi-
crochannels are fabricated in a clean-room of the Center of micro/nanotechnology,
Ecole Polytechnique Federale de Lausanne and Thai Microelectronics Center. Be-
cause of some complications in its fabrication process, only the prototype is being
developed, with a substantial cost.

- Model 4: The wound truss structure with a uniform carbon plate and poly-
  imide tubes in the middle (revisited)

The concept of this model is similar to Model 2 with an outer radius of 0.10
mm, but the structures are completely redesigned to make them more systematic
and similar to those in the outer barrel. Some inconsistencies such as the element
sequence and empty space are corrected (see Figure 3.5(f)).

(a) Model 0

(b) Model 1

(c) Model 2.1

(d) Model 2.2

(e) Model 3

(f) Model 4
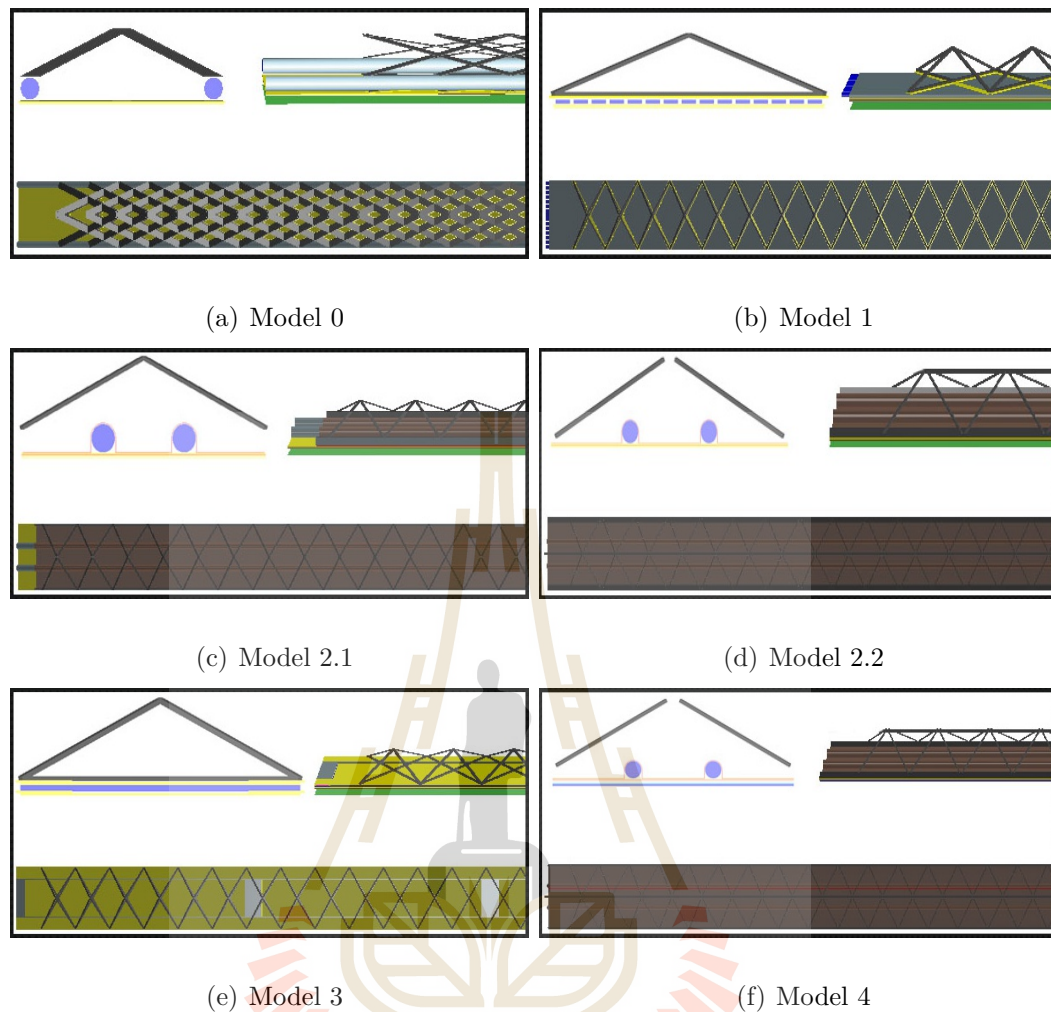
Figure 3.5 Assembly of the inner barrel stave prototype composed of the space frame, cooling structure, and sensor chip. For material analysis the different structures are being considered a) The wound truss structure with cooling pipes at the vertices, b) The wound truss structure with polyimide microchannel cooling, c) The wound truss structure with uniform carbon plate and 0.15 mm outer radius polyimide tubes in the middle, d) The wound truss structure with uniform carbon plate and 0.10 mm outer radius polyimide tubes in the middle, e) The wound truss structure with silicon microchannel and f) The wound truss structure with uniform carbon plate and polyimide tubes in the middle (revisited) (Poonsawat et al., 2019).

By coding a detailed geometrical description of all models in ALIROOT, the complete simulation of all stave models can be performed. All models have been considered for their material budget distribution.

3.3 Material budget (X/X_0) calculation of the ITS stave prototypes

The reduction of material budget for the ITS can increase the impact parameter resolution and the tracking efficiency in low transverse momentum region. In this section, we will study the material budget of the new ITS structure.

The probability of particles passing through the material interacting with the nuclei or electrons of the medium depends on the layer thickness and internal potential. However, the strength of the interaction can be expressed in terms of the cross-section (σ). The corresponding cross-section related to the interaction probability can be shown by

$$dW = dxN\sigma. \tag{3.1}$$

In a particular type of interaction, its partial cross-section presents the probability that the particles are scattered. One can also call it a differential cross-section. Therefore, the total cross-section can be given by

$$\sigma_{tot} = \int \frac{d\sigma}{d\Omega} d\Omega, \tag{3.2}$$

where $d\Omega = \sin\theta d\theta d\phi$.

The direction of charged particles changes because of the collided from nuclei. In small deviation angles, the direction deviation of a particle traversing in the material with thickness L can be obtained from the radiation length X_0. This X_0 represents the behaviors of particles interacting in a material. The radiation length is the mean path length required to reduce the energy of relativistic charged particles by a factor $1/e$ related to its energy loss (Olive, 2014). The radiation length of the material can be approximated with the expression of the atomic

number and atomic weight of the nucleus. The radiation length of a material for a single type of nuclei can be calculated by the following expression (Beringer et al., 2012)

$$X_0 = \frac{716.4 \cdot A}{Z(Z+1)\ln\frac{287}{\sqrt{Z}}} \quad \text{g} \cdot \text{cm}^{-2}$$

$$= \frac{1432.8 \cdot A}{Z(Z+1)(11.319 - \ln Z)} \quad \text{g} \cdot \text{cm}^{-2}, \tag{3.3}$$

where Z is the atomic number and A is the atomic weight or mass number of the nucleus.

In the case of a compound material or mixture, the radiation length can be estimated with the combination of all compound radiation lengths multiplied by the mass fraction (Gupta, 2010):

$$\frac{1}{X_0} = \sum_i w_i \left(\frac{1}{X_0}\right)_i, \tag{3.4}$$

where w_i is the fractional weight of component i.

For the stave prototypes, the material budget can be obtained from the radiation length of the material. The amount of material budget depends on the thickness (X/X_0) and percentage of surface covered ($X/X_0(\%)$). They can be calculated using the following expression

$$X/X_0 = \frac{\text{thickness}}{\text{radiation} \quad \text{length}}, \tag{3.5}$$

$$X/X_0(\%) = \frac{\text{thickness}}{\text{radiation} \quad \text{length}} \times \text{surface}(\%). \tag{3.6}$$

3.4   Material budget simulation

To show that the material budget can be reduced to 0.3%, we use ALIROOT software to calculate the material budget for all stave models.

The material budget of each stave model can be calculated from the radiation length of their components. It depends on either the thickness or percentage of the covered surface of the material. The material budget can be computed in ALIROOT by performing the fake particles with no charge, called "geantinos". They have shot straight the sensors without a deviation or any kind of energy loss. The volume crossed by geantinos can be restricted by adjusting the minimum radius $R_{\min}$ and maximum radius $R_{\max}$, the minimum and maximum ϕ values, and the range in Z, between $-Z_{\min}$ and $+Z_{\max}$, of the traversing region. The material budget will be determined in two methods: 1) the geantino tracks are generated perpendicular to the Z-axis of the staves; hence, the "actual" material budget can be determined; 2) all geantinos come from the interaction point, so the material budget is the same, as seen by real particles coming from the collisions depending on the provided η range.

The stave design accounts for the material budget requirement, which is limited to 0.3% for the inner barrel and 0.8% for the outer barrel (ALICE Collaboration, 2012).

3.4.1   Simulation results of inner barrel

The simulations include essentially all material properties used in each model. For the inner barrel, the properties of materials used in the ALICE ITS upgrade scenarios are listed in Table 3.2 and Table 3.3.

The results for the material budget calculation of different models for the inner barrel are presented in Figure 3.6. The highest peaks represent the overlap-

Table 3.2 List of the stave components and their thickness used in ALIROOT simulation. The numbers in brackets refer to the conceptual parameters in CDR.

Material	Model 0	Model 1	Model 2.1	Model 2.2	Model 3	Model 4
			Thickness [μm]			
Filament						
Top CFRP M60J 3K	70 (70)	200 (120)	200 (100)	200 (100)	200 (120)	200 (100)
Bottom CFRP M60J 3K	70 (-)	200 (240)	-	-	200 (240)	-
Cooling						
Pipe Kapton	70 (70)	-	130 (70)	130 (70)	-	130 (70)
water	1450 (1450)	-	1450 (1450)	940 (940)	-	940 (940)
Carbon plate	-	-	140 (140)	140 (140)	-	140 (140)
Sensor						
Glue	125 (200)	250 (200)	100 (200)	100 (200)	250 (200)	100 (200)
Silicon chip			50 (50)			
Flex cable			100 (-)			
Polyimide Microchannel	-	100 (100)	-	-	-	-
Silicon Microchannel	-	-	-	-	40 (40)	-
water	-	200 (200)	-	-	160 (160)	-

Table 3.3 List of the stave components and their contribution to the radiation length. The numbers in brackets refer to the approximation value in CDR.

Material	Model 0	Model 1	Model 2.1	Model 2.2	Model 3	Model 4
			X_0 [cm]			
Filament						
Top CFRP M60J 3K			19 (25)			
Bottom CFRP M60J 3K	19 (25)	19 (25)	-	-	19 (25)	-
Cooling						
Pipe Kapton	28.4 (28.6)	-	28.4 (28.6)	28.4 (28.6)	-	28.4 (28.6)
water	35.8 (36.1)	-	35.8 (36.1)	35.8 (36.1)	-	35.8 (36.1)
Amec Thermasol FGS 003	-	-	27 (25)	27 (25)	-	27 (25)
C Fleece	-	-	106 (25)	106 (25)	-	106 (25)
Sensor						
Glue			44.37 (44.37)			
Silicon chip			9.35 (9.36)			
Flex cable			13.3 (13.3)			
Polyimide Microchannel	-	28.4 (28.6)	-	-	-	-
Silicon Microchannel	-	-	-	-	9.35 (9.36)	-
water	-	35.8 (36.1)	-	-	35.8 (36.1)	-
K13D2U 2K	-	-	26 (25)	26 (25)	-	26 (25)
C Fleece	-	-	106 (25)	106 (25)	-	106 (25)

ping between each stave. In model 2.2, the location of the cooling pipes around the middle of the stave can help to enhance the thermal conductivity despite the higher material budget than model 0. The second highest peaks in Figure 3.6(c) and Figure 3.6(d) are due to the polyimide cooling pipes filled with water. Instead of cooling pipes, using the microchannel-filled water in model 1 or Freon in model 3 as a coolant can serve as a better average method to dissipate the heat from the sensors (Rossegger, 2013). However, model 1 has a higher material budget than model 2.2, while in model 3, the silicon microchannel is still in the R&D

phase and not yet ready for implementation due to the highest of production cost. All models have been considered and proceeded to calculate their material budget distribution.

A summary of material budget calculation for all stave prototypes are given in Table 3.4.

Table 3.4 Expected overall material budget obtained from ALIROOT simulation for different stave prototypes compared to the possible theoretical calculation in CDR (Poonsawat et al., 2019).

Stave prototype	X/X_0 [CDR] (%)	X/X_0 [ALIROOT] (%)
Model 0	0.26	0.284
Model 1	0.30	0.334
Model		
2.1	0.31	0.344
2.2	0.30	0.303
Model 3	0.25	0.249

3.4.2 Simulation results of outer barrel

The simulation results of the inner barrel shown that the material budget of model 2.2 is underestimated of the required value of the upgrade scheme while preserving a good thermal conductivity and production cost. Therefore, model 2.2 has been used as a starting prototype of the outer barrel because its conceptual design is similar. However, the bottom of the supporting part of the outer barrel stave is split longitudinally into two half-staves along the azimuthal direction, as shown in Figure 3.7. Each half-stave consists of seven sensor chips with integrated cooling pipes and cold plates. These two pipes have an inner diameter of 2.67 mm filled with water.

The stave structure of the outer barrels has been designed to achieve the required stiffness and thermal properties as expected in the inner barrels. Several

(a) Model 0

(b) Model 1

(c) Model 2.1

(d) Model 2.2

(e) Model 3
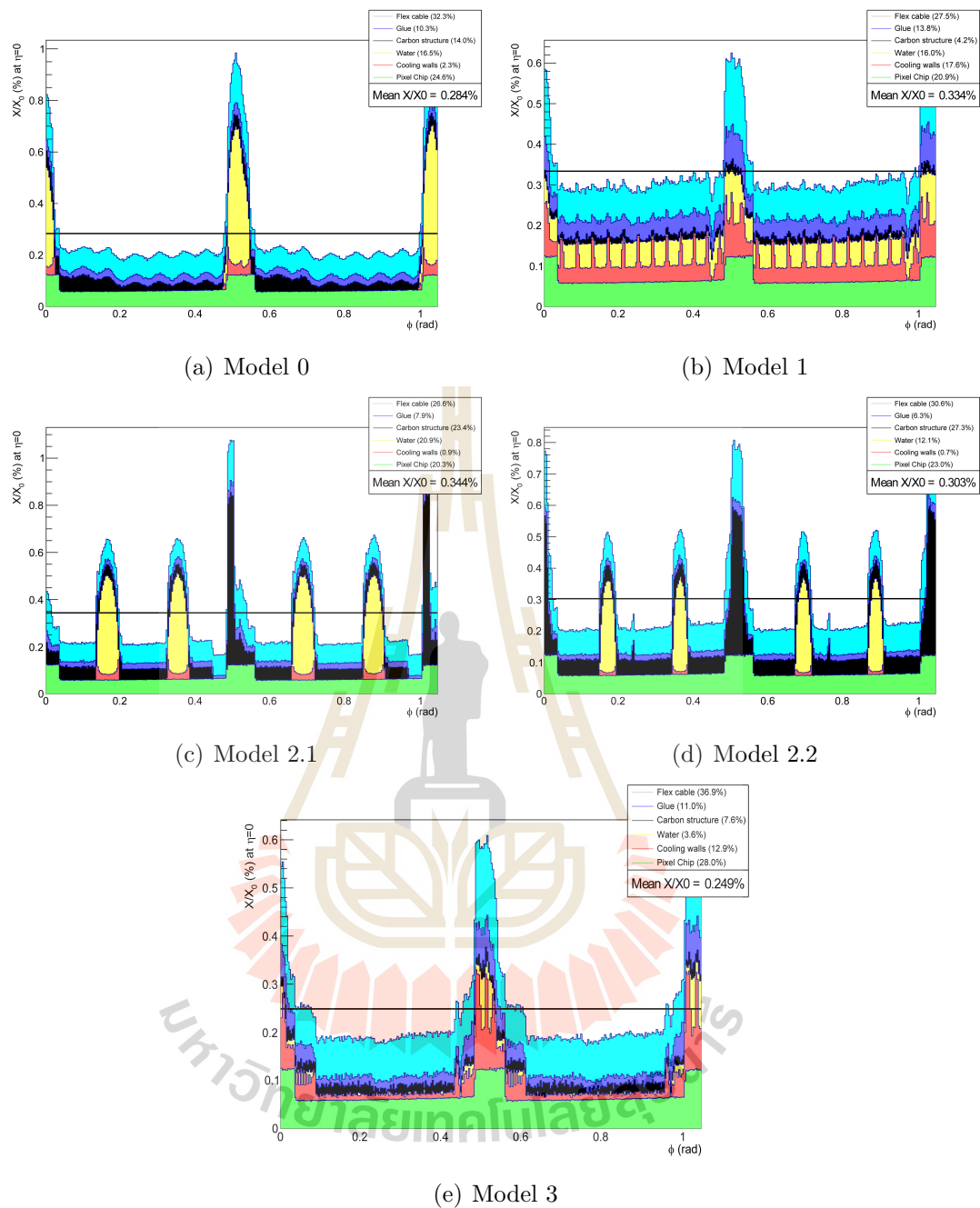
Figure 3.6 Our material budget distribution results of the stave prototype. The highest peaks for each subfigure correspond to the overlap of carbon structure at the edge of a) Wound truss structure with cooling pipes at the vertices, b) Wound truss structure with polyimide microchannel cooling, c) Wound truss structure with uniform carbon plate and 0.15 mm outer radius polyimide tubes in the middle, d) Wound truss structure with uniform carbon plate and 0.10 mm outer radius polyimide tubes in the middle and e) Wound truss structure with silicon microchannel (Poonsawat et al., 2019).
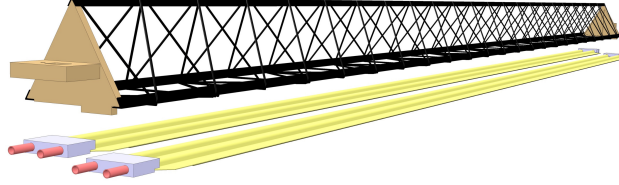
Figure 3.7 Schematic of the layout of the mechanical and cooling structure of the outer barrel stave (ALICE Collaboration, 2014a).

components, similar to the inner barrel, are used for prototyping the outer barrel stave. The estimates of the material budget contribution for the outer barrel stave are reported in Table 3.5.

Table 3.5 List of the outer stave components and their thickness and the estimated contributions to the material budget (ALICE Collaboration, 2014a).

Stave element	Component	Material	Thickness [μm]	X/X_0 [cm]	X/X_0 [%]
Module	FPC Metal layers	Aluminum	50	8.896	0.056
	FPC Insulating layers	Polyimide	100	28.41	0.035
	FPC Insulating layers	Polyimide	100	28.41	0.035
	Module plate	Carbon fiber	120	26.08	0.046
	Pixel Chip	Silicon	50	9.369	0.053
	Glue	Eccobond 45	100	44.37	0.023
Power Bus	Metal layers	Aluminum	200	8.896	0.225
	Insulating layers	Polyimide	200	28.41	0.070
	Glue	Eccobond 45	100	44.37	0.023
Cold Plate		Carbon fleece	40	106.80	0.004
		Carbon paper	30	26.56	0.011
	Cooling tube wall	Polyimide	64	28.41	0.013
	Cooling fluid	water		35.76	0.105
	Carbon plate	Carbon fiber	120	26.08	0.046
	Glue	Eccobond 45	100	44.37	0.023
Space Frame		Carbon rowing			0.080
Total					**0.813**

The simulation results of the material distribution across the outer barrel staves are presented in Figure 3.8. The half-staves are partially superimposed surrounding the detector, thus giving rise to the peaks at about $1.25\% X_0$. The highest peaks are due to the polyimide cooling pipes, filled with water, embedded in the cold plate. The estimated overall material budget is within reach of the expected 0.8%.
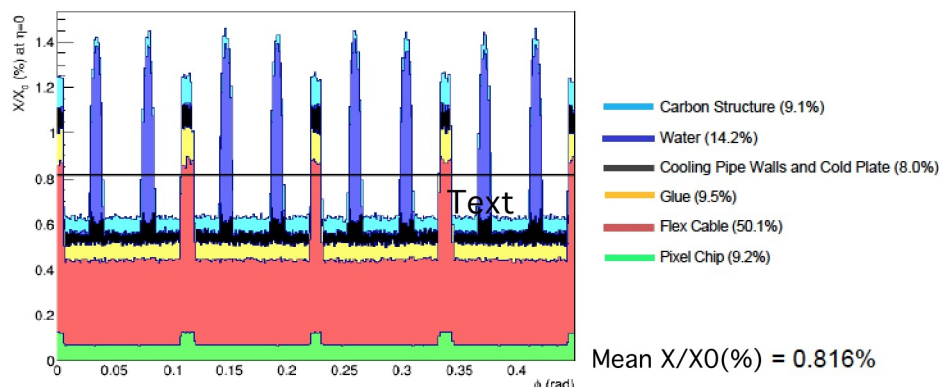
Figure 3.8 Material budget distribution of outer barrel prototype. The highest peaks correspond to the polyimide cooling pipes, filled of water, embedded in the cold plate (ALICE Collaboration, 2014a).

3.5 Study of silicon wafer

In this simulation, all the stave components have been simulated with the detailed geometry for their material budget distribution. The first two components of the stave (space frame and cold plate) have been considered as the support structure for the silicon detector. To reach the requirement of the material budget reduction, all components of the stave must be developed. The support structure can be reduced its material budget by using of the light filament-wound carbon. In the same context, the detector has to be thin while preserving the high resistivity.

The study of material properties can be helped to decide the starting materials used in the sensor production process. The thickness and quality of the epitaxial silicon detector indicate the overall performance of sensors. The high-resistivity (> 1 kΩ·cm) epitaxial wafers (see Figure 3.9), a substrate of a CMOS Monolithic Active Pixel Sensor designed for an upgrade of the ITS, has been chosen for this study. In this work, the 50 µm thickness prototypes (to keep minimum material budget) with 25 µm epitaxial layer thickness has been characterized. To ensure that the thin prototype chips can perform the high resistivity, there will

be tested with the Spreading Resistance Profiling (SRP) to obtain their physical changes and measure their resistivity after fabrication processes.
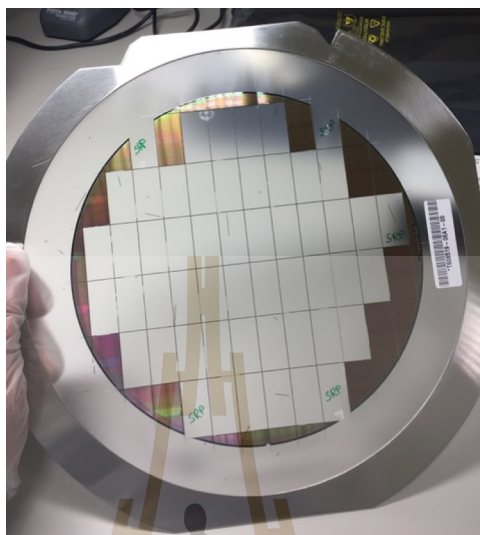
Figure 3.9 The 49 reticles cut on 8 inches blank wafer (Prabket et al., 2019).

3.5.1 Spreading Resistance Profiling (SRP)

The silicon sensors are an essential part of tracking and vertexing detectors. Their doping profile of the epitaxial layer is used for the selection process of their starting materials (Besson et al., 2017; Treberspurg et al., 2012). The doping profile of the Si sensor can be characterized by the Spreading Resistance Profiling or SRP technique (Mazur and Dickey, 1966) to measure the doping concentration in deeper structures of silicon. The measurement setup is shown in Figure 3.10. The bias voltage was applied to the two tungsten carbide probe tips pressed on the beveled semiconductor surface which generate the spreading current. The spreading resistance (R_{sr}) generated from this current is used to evaluate a depth profile resistivity (ρ) at each position. The relation between spreading resistance and resistivity is given by $R_{sr} = \frac{\rho}{2a}$, where a is the radius of probe tips.
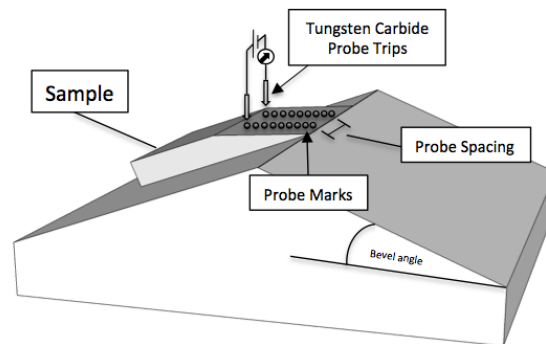
Figure 3.10 Two tungsten carbide probe tips are stepped along a beveled surface for resistance measurements.

The measurement resistance (R_m) will be defined as the combination of the spreading resistance, the resistance effected from the contacting surface (R_{bar}) and bulk resistance (R_p).

$$R_m = R_{sr} + R_{bar} + R_p \tag{3.7}$$

By asssuming that $R_p << R_{sr}$ and $R_p << R_{bar}$ due to the small space between probe and small contact radii (a), the Eq. 3.7 becomes (Sentech Instruments, 1994):

$$R_m = R_{sr} + R_{bar} = \frac{\rho}{2a}B(\rho), \tag{3.8}$$

where $B(\rho)$ is a calibration function depends on ρ.

The resistivity can be determined with a preceding calibration profile contains known ρ samples. For Si, the calibration profile of <100> or <111> orientation is offered in the calculation software.

3.5.2 Measurement results and discussion

The depth profile of wafer with 25 μm epitaxial layer thickness (see Figure 3.11) shows decreasing in resistivity after 20 μm depth. The spanning wide of high resistivity area represent the better thickness and quality of the epitaxial silicon sensing layer. The plot implies that the distribution of dopant, which is boron in our case, at the deeper level is more dense than the shallow one. Therefore, this wafer possesses high resistivity more than 1 kΩ·cm which is sufficient to be used as a starting material for the new sensor production for ALICE ITS upgrade.
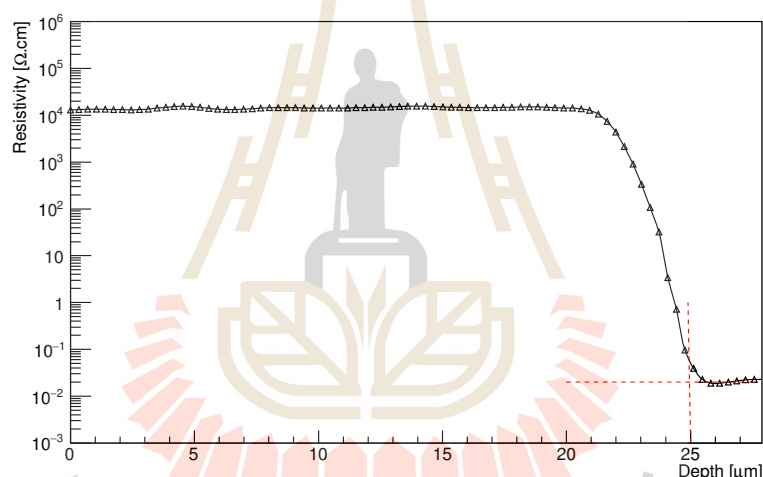
Figure 3.11 SRP: depth profile of 25 μm pitaxial layer thickness and average resistivity 9.03 kΩ·cm (Prabket et al., 2019).

3.6 Summarry

The simulation of stave prototypes and the application of a new cooling system by ALiROOT can perform a reduction in the material budget for the new ITS. The results show that the use of lightweight carbon structure with polyimide cooling pipes can reduce the material budget to 0.3% per layer in model 2 for the inner barrel and 0.8% for the outer barrel. The addition of an innermost layer and

the use of smaller pixel size CMOS sensors can extend the coverage radius and perform the coverage pseudo-rapidity ($|\eta| \leq 1.22$). The used of thin silicon sensor will keep the low material budget while preserving the high resistivity profile. The simulation results can guarantee that the conceptual design used in the new ITS satisfies the requirements of the upgraded ALICE detector.

Although the new design of the stave prototype is underestimated the upgrade requirement, the effect of the detectors must be considered for their performance. The most important key of this work is the pixel sensor characterization that we will describe in the next section.
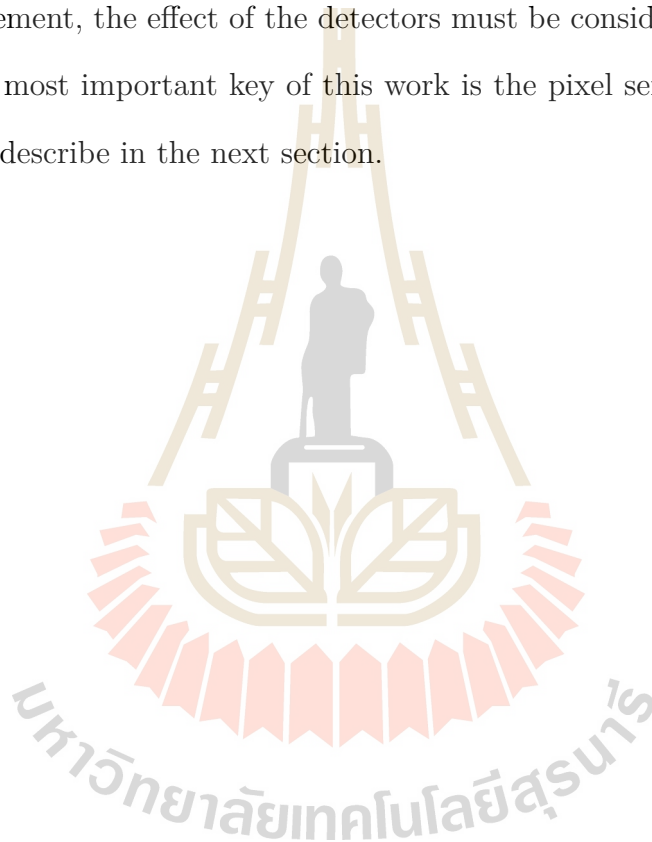
CHAPTER IV

PIXEL SENSOR

The Monolithic Active Pixel Sensor (MAPS) (Havránek et al., 2015) is chosen to be used in the new ALICE ITS staves. MAPS has been developed since the late 1990s based on silicon substrates with a thin epitaxial layer. Each pixel chip consists of single silicon die of 15 mm×30 mm with high-resistivity epitaxial layer form as the sensor unit.

In this chapter, an overview of pixel sensors for high energy physics experiments will be proposed. The chapter starts with the interaction of radiation with matter. The principle of pixel sensors detection is then presented. Finally, the description of Monolithic Active Pixel Sensors (MAPS) and their development for the new ITS of the ALICE experiment will be explained.

4.1 The interaction between radiation and matter

When a beam of radiation traversing the matter, it will be either absorbed or scattered with the atom. These process can be explained in term of the interaction between particles in the beam of radiation and particles in the material. There are two main effects that can be used to characterize the passage of a charged particle through a thickness of material, one is the energy loss by the particle, and the other is a deflection of the same particle from its incident direction. The interaction depends on the energy, the mass and the charge of the incoming particle and the characteristics of the medium. For semiconductor detectors, the energy deposited from the moving particles will be converted into the signal which can

be used to analyze for their properties such as the energy or the position. The mechanisms of energy loss of charged particles and photons will be described in the next section.

4.1.1 Energy loss of charged particles

In inelastic collisions with atomic electrons, the energy of charged particles will suffer a loss when traversing matter. The Bethe-Bloch formula can describe the mean energy per unit length (in MeV g^{-1} cm^2), often called stopping power, in the following equation,

$$-\frac{dE}{dx} = 2\pi N_a r_e^2 m_e c^2 \rho \frac{Z}{A} \frac{z^2}{\beta^2} \left[\ln \frac{2m_e c^2 \beta^2 \gamma^2 T_{\max}}{I^2} - 2\beta^2 - \delta - 2\frac{C}{Z} \right], \qquad (4.1)$$

where N_a is Avogadro's number; r_e is electron radius (2.817×10^{-13} cm); $m_e c^2$ is electron rest mass energy; ρ is density of absorbing material; Z and A (in g mol^{-1}) are the atomic number and atomic weight of the material, respectively; z is the charge of the particle; β is v/c of traversing particle; I is the mean excitation potential; γ is Lorentz factor $\left(\frac{1}{\sqrt{1-\beta^2}} \right)$; δ is called the density correction caused by the fact that the electric field of the particle polarizes the material and hence causes a shielding of the particle's electric field and $T_{\max}$ is the maximum kinetic energy transfer in a single collision. The maximum energy transfer is given by

$$T_{\max} = \frac{2m_e c^2 \beta^2 \gamma^2}{1 + 2\gamma \frac{m_e}{M} + \left(\frac{m_e}{M} \right)^2}, \qquad (4.2)$$

where M is the incident particle mass.

In Figure 4.1, the energy loss of low energy particles depends on velocity ($1/\beta^2$ factor) and mass of the incoming particles. It decreases with increasing velocity. For velocity (β) about $0.96c$, the energy loss is the minimum. The particles at this point are called the minimum ionizing particles (MIPs). The

minimum energy loss of different particles is different which can be used to identify the type particles. The correction terms in Eq. 4.1 refer to the energy of particles. The density correction is generally used for high particle energies and the shell correction for lower energies (Nakamura et al., 2010).
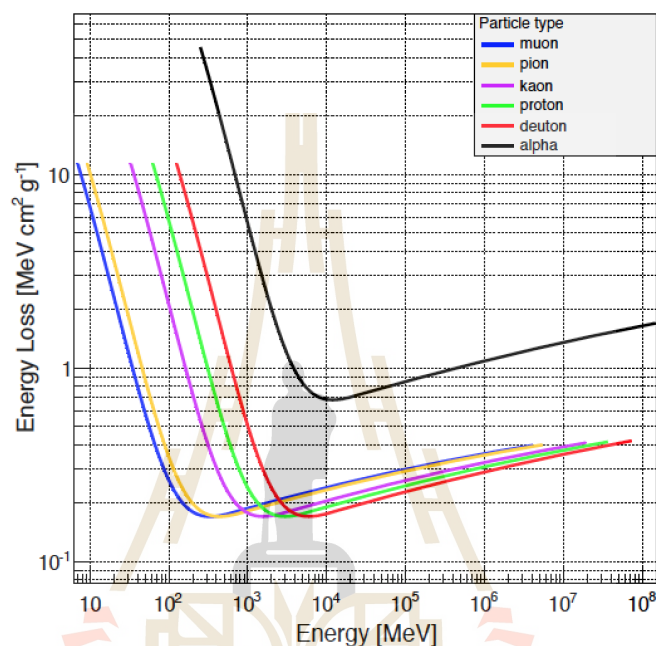
Figure 4.1 Average energy loss according to Eq. 4.1 as a function of energy for protons, pions and muons. The density correction is not considered (Leo, 1987).

For electrons and positrons, which interact with identical particles in the medium, the Bethe-Bloch formula must be modified due to their low mass. In energy range around a few MeV, the collisional energy loss due to the electromagnetic emission (bremsstrahlung) of such particles can be ignored. However, in high energy above a few tens MeV, the dominant of electromagnetic radiation will enlarge the collisional energy loss. This loss is proportional to the incoming particles energy and the atomic electron energy in the absorber which decreases exponentially respect to the medium depth. Therefore, the energy loss only depends on the material type and the thickness of absorber in term of its radiation

length.

The Bethe-Bloch formula can be used to obtain the average energy loss of an incident particle as a distribution due to the statistical fluctuations. The energy loss distribution of thick absorbers is well defined by a Gaussian distribution while the Landau distribution (Landau, 1944) is better described for the thin absorber according to the small number of collisions and the energy transferred in each collision. Moreover, charged particles traversing a detector are subjected to the Multiple Coulomb Scattering that provides the small deviations of the track as a symmetry angle along the incident direction. The scattering angle under the Gaussian distribution is defined by

$$\theta_{RMS} = \frac{13.6 MeV}{\beta pc} z\sqrt{x/X_0}[1 + 0.38 \ln{(x/X_0)}], \tag{4.3}$$

where β is the velocity, p is the momentum, and z is the charge of the particle. The thickness of the absorption medium is related to the term x/X_0 (material budget) of Eq. 4.3 which effects to the radiation of an incident particle. Thus, this defection must be reduced by decreasing the detector material budget.

The signal of the amount of the electron-hole pairs generated in the medium can be evaluated by dividing the deposited energy with 3.6 (3.6 eV is the mean energy needed for ionization in silicon). The mean deposited energy can be obtained from Eq. 4.1.

4.1.2 Energy loss of photons

The traversing photon from the electromagnetic radiation can interact with the absorbing medium via three possible processes (Nakamura et al., 2010; Rossi et al., 2006). The photon will be scattered with a large angle in the Compton effect process, or completely absorbed in photoelectric effect and pair production

process. A monochromatic photon beam remains unchanged in absorption probability (energy) while its intensity will be decreased with the penetration depth of the absorption layers, according to

$$I(x) = I_0 e^{-\mu x}, \tag{4.4}$$

where I_0 is the intensity of the initial photon beam and I is the beam intensity after traversing a medium of thickness x and μ is the linear attenuation coefficient which depends on the material type and the incident photons energy.

In these processes, the incident photon energy is the key to occurring interaction. The photoelectric process dominates at the low energy range below 100 keV while the Compton effect dominates, in the range between a few hundred keV and a few MeV. For high energy above 100 MeV, pair production becomes dominant. Therefore, the low energy photons from the radioactive source are used to study the detector responsibility. For soft X-rays energy below 10 keV (e.g., [55]Fe), the primary electron emitted from the photoelectric effect will generate the $e - h$ pairs along its path, less than 1 μm for a 6 keV electron (Thompson et al., 2001)) in silicon. This distance is minimal compared to the sensor size. Hence, the generation of $e - h$ pairs is considered as the point-like process.

The average number of the $e-h$ pair generated by a photon can be obtained from the net energy required for an electron-hole pair production as follow:

$$N_{e-h} = \frac{E_{ph}}{\omega}, \tag{4.5}$$

where N_{e-h} is the average number of the electron-hole pair, E_{ph} is the photon energy and ω is 3.6 eV in silicon.

4.2 Pixel detectors

The pixel sensor is a semiconductor detector with two-dimensional segmentation of the sensitive area. This area consists of the matrix of square pixels of the same size which surrounded by the control modules at the bottom edge of the chip. Next, the power supply unit and data transmission are located for allowing the detector to interface with an external DAQ system.

The active areas consist of sensitivities elements or sensors where an output signal is generated and amplified with the front-end circuit. All pixels are usually grouped into columns with a shared readout circuity to reduce the readout time. Data readout by the chip peripheral will be compressed and buffered and send to the external data acquisition system. Moreover, the effects of radiation will be considered due to the sensor efficiency depends on the radiation gain.

4.2.1 Collection diode

A signal of the generated electron-hole pair will be collected within the electric field inside the depletion layer of the silicon sensor. It is called collection diode. This part consists of a junction between an n-well (n$^+$, $N_D \approx 1 \times 10^{17}$ cm^3) on its top and the p-type epitaxial layer (p$^-$, $N_A \approx 1 \times 10^{12}$ cm^3) called p-n junction. This junction is generally used for signal simplification where the doping concentration is constant on both sides.

The electric field in p-n junction will be built up by a so-called built-in voltage (V_{BI}). In thermal equilibrium and the doping concentration is constant on both sides, V_{BI} of an abrupt planar p-n junction can be expressed as

$$V_{BI} = \frac{k_B T}{q} \ln\left(\frac{N_D N_A}{n_i^2}\right), \tag{4.6}$$

where N_D is the concentration of donors (n-type), N_A is the concentration of acceptors (p-type), n_i is the intrinsic carrier concentration, k_B is the Boltzmann constant, q is the unit charge, and T the temperature. The depletion volume of the sensor depends on the doping concentration on both sides of the junction. It can be enlarged the width by applying an external reverse bias voltage (V_{RB}). The depletion width can written as

$$d = d_n + d_p$$

$$= \sqrt{\frac{2\epsilon}{q} \frac{N_A}{(N_A + N_D)\, N_D} (V_{BI} - V_{RB})} + \sqrt{\frac{2\epsilon}{q} \frac{N_D}{(N_A + N_D)\, N_A} (V_{BI} - V_{RB})}$$

$$= \sqrt{\frac{2\epsilon}{q} \left(\frac{1}{N_A} + \frac{1}{N_D}\right) (V_{BI} - V_{RB})} \qquad (4.7)$$

where d_n and d_p are the width of the depletion on n-doped and p-doped region respectively, and ϵ is the dielectric constant in silicon ($\epsilon = \epsilon_0 \epsilon_{Si}$. If the depletion volume goes into the lowest side of the epitaxial layer, the term $1/N_D$ in Eq. 4.7 can be ignored.

The silicon wafer from the manufacturing has a specific resistivity (ρ). This value is related to the doping concentration described below.

$$\rho = \frac{1}{N\mu q}, \qquad (4.8)$$

where μ is the mobility of the respective carrier and N is the doping concentration of the material. Hence, the width of the depletion zone in Eq. 4.7 can be written in the proportional term as

$$d \propto \sqrt{\rho \, (V_{BI} - V_{RB})}. \qquad (4.9)$$

Thus, the increasing of reverse bias voltage or resistivity will extend the volume of the depletion region.

In p-n junction with reverse bias voltage can constitute the capacitance C. The optimized capacitance can increase the gain of the sensor. For p-n junction with depletion thickness d, the capacitance can be obtained by

$$C = \epsilon \frac{A}{d} = A\sqrt{\frac{\epsilon q N_A}{2\Delta V}} \tag{4.10}$$

where $\Delta_V = V_{BI} - V_{RB}$ of the junction area A, ϵ is dielectric constant, and d is the depletion layer width. Eq. 4.10 shows that the increase of the reverse bias voltage leads to a decreasing in capacitance.

4.2.2 Leakage current

When the charge carriers generated by ionizing radiation in the depletion layer of a reversely biased diode, they will be collected by the electrode and produce the current. In the case of non-radiation, the current still occurs due to the spread of the free carriers outside the depletion region in the sensor called leakage current. The charge carriers gathered in the depletion layer will cause the rising thermal. This thermal is proportional to the depleted volume represented by the volume generation current J_{vol} which is a temperature dependence (Rossi et al., 2006). It can be obtained by

$$J_{vol} \propto T^2 e^{-E_g(T)/2k_B T}, \tag{4.11}$$

where E_g is the energy range (bandgap) between the conduction band and valence band.

4.3   Monolithic Active Pixel Sensors for the new ITS

The Monolithic Active Pixel Sensors is the combined of sensitive elements and readout electronics in one chip. Its thickness is thinner than the hybrid pixel sensors. Thus, it is suitable for applications which low material budget is required. MAPS consist of a highly doped p^{++} substrate with the thickness lower than 20 μm. It is implanted with the donors which will provide a thin epitaxial layer with low p-doped. Hence, the free electrons from an impinging particle inside the epitaxial layer cannot lose in the substrate which leads to a weak signal to noise ratio because it will be reflected at the interface with the bulk.

The created n-well in an epitaxial layer will produce the collection diode which allows a low input capacitance (~ 10 fF) due to the thickness of the sensitive volume.

The LHC experiments are presently using the hybrid pixel sensor in particles tracking. According to their low capacitance and high radiation tolerance there provide the high signal to noise ratio but the thickness of hybrid pixel structure leads to a larger material budget. In order to achieve the goal of physics performance of the upgraded ITS, a total material budget per layer in the inner layers must lower than $0.3\% X_0$. Therefore, the new sensor thickness design is reduced to 50 μm by using MAPS instead. The summary of sensor thickness presently used in the LAHC experiment is shown in Table 4.1.

Table 4.1 Thickness of the pixels of ALICE (present), ATLAS and CMS.

Experiments	Total pixel chip thickness [μm]
ALICE pixels (present)	350
ATLAS pixels	430
CMS pixels	430

The monolithic active pixel sensors are firstly used in the heavy-ion experiment at RHIC, called the Ultimate sensor. It is developed for the Heavy Flavor Tracker by the STAR experiment (Valin et al., 2012). However, this sensor technology is not satisfying of the ALICE ITS upgrade regarding the radiation hardness and the readout time. Thus, the ALICE team decide to use the CMOS imaging sensor technology provided by TowerJazz which is solved the radiation hardness requirements (Hillemanns et al., 2013) due to its thin gate oxide (4 nm thick). Its advantages are as follow:

- The thickness the epitaxial layer is only 18 μm that thin enough for the required material budget.

- It is allowed for low reverse bias voltages which will provide the shorter charge collection times of the high resistivity epitaxial layer (1 kΩcm - 6 kΩcm).

- The implanted deep p-well under the PMOS transistors can improve more charge collection of PMOS n-wells and the other n-wells (Figure 4.2). Together with the full CMOS circuits, the fast readout will be allowed.
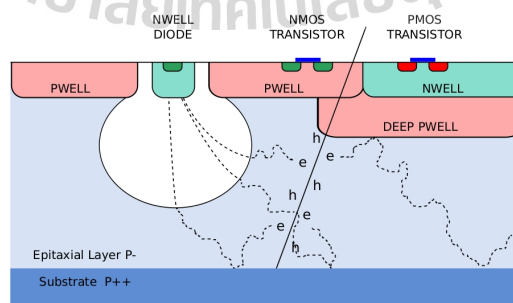
Figure 4.2 Schematic cross sectional of the TowerJazz 0.18 μm imaging sensor technology (ALICE Collaboration, 2014a).

The requirements on the pixel chips are shown in Table 4.2.

Table 4.2 General pixel-chip requirements (ALICE Collaboration, 2014a).

Parameter	Inner Barrel	Outer Barrel
Chip dimensions	15mm $\times$ 30mm ($r\phi \times z$)	
Sensor thickness	50μm	
Spatial resolution	5μm	10μm
Detection efficiency	> 99%	
Fake-hit rate	$< 10^{-5}$ event^{-1}pixel^{-1}	
Integration time	$< 30\mu$s	
Power density	< 300mW/cm^2	< 100mW/cm^2
Temperature	20°C to 30°C	
TID radiation hardness	2700 krad	100 krad
NIEL radiation hardness	1.7×10^{13} 1MeVn$_{eq}$/cm^2	1×10^{12} 1MeVn$_{eq}$/cm^2

4.3.1 Pixel architectures

There are two main architectures developed for the new ITS, MISTRAL and ALPIDE. MISTRAL (MImosa Sensor Tracker Alice) is the optimized version of the MIMOSA28 sensor designed for the STAR-PXL detector in the readout architecture (Schambach et al., 2015). The first prototype of MISTRAL is MISTRAL-O (O is outer). It has 36×64 μm^2 of pitch size, power consumption of 97 mW/cm^2, 1.7 mm $\times$ 30 mm of the dead area, and covered by 15 mm $\times$ 30 mm of sensitive are, as shown in Figure 4.3.
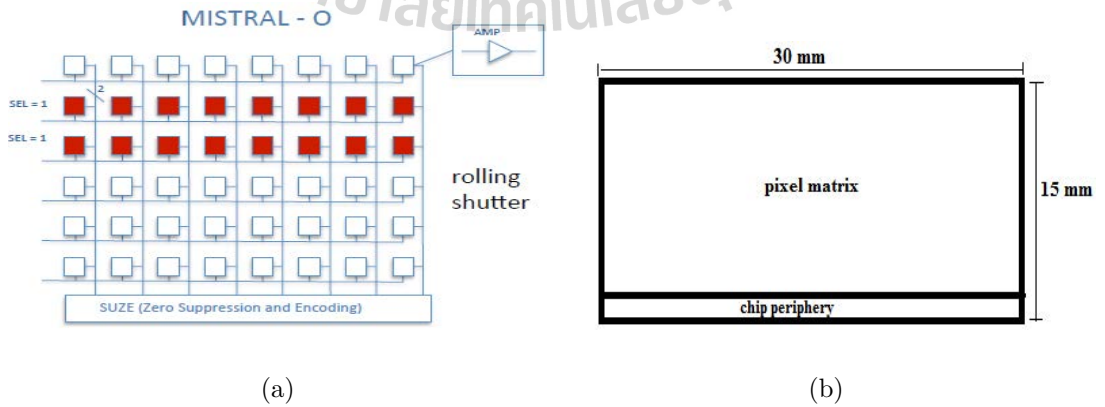
Figure 4.3 Mistral-O pixel matrix (a) and its structure (b) (Hu-Guo et al., 2013).

Mistral uses a rolling shutter readout architecture with two rows processed simultaneously and they are read sequentially. The signal will be amplified within the matrix pixels and then transfers to the chip periphery. In this part, the large amount of readout data will be discriminated and then compressed by the zero-suppression algorithm (pixels without hit will be reset). The readout time for all the matrix is approximately 20 μm before sent out of the chip.

For the ALPIDE (ALice PIxel DEtector) architecture, the peripheral circuits are contained in a pixel, eg., the amplifier, the multiple hit buffers, and the zero-suppression performed within the matrix. All of these features are controlled by an Address-Encoder Reset-Decoder (AERD) circuit which takes care of propagating the addresses of hit pixels to the end-of-column. The readout of a pixel in this technology is operated with an external trigger combined with short shutter windows or in the continuous acquisition mode.

The first prototype of the ALPIDE is pALPIDEfs. It has been developed for the ITS upgraded requirement which are the low power consumption of $\sim$40 mW/cm^2 and fast readout. A pixel pitch of pALPIDEfs is 28×28 μm while its chip size is 15×30 mm^2. The pixel matrix of the chip is organized with 512×1024 (row $\times$ column) an and a dead area of 1.1×30 mm^2, as shown in Figure 4.4.

(a)   (b)
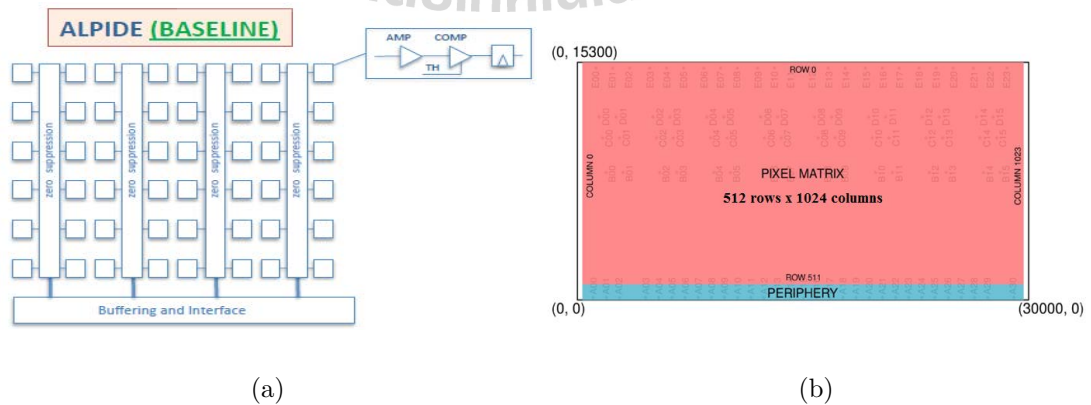
Figure 4.4 pALPIDE pixel matrix (a) and its structure (b) (Hu-Guo et al., 2013).

As a consequence described above, the characteristic properties of the ALPIDE is better than the MISTRAL regarding the integration time and power consumption. Therefore, the ALPIDE chips will be chosen for the new ITS. The summary of the chip characteristic between MISTRAL and ALPIDE are shown in Table 4.3.

Table 4.3 ALPIDE and MISTRAL characteristic parameters (Kofarago, 2015).

Parameter	ALPIDE	MISTRAL-O
Pixel pitch	28×28 mm^2	36×64 mm^2
Integration time	< 2 μs	~ 20 μs
Power consumption	39 mW/cm^2	73-97 mW/cm^2
Dead area	1.1×30 mm^2	1.7×30 mm^2
Readout mode	Priority encoder	Rolling shutter
Discriminator position	Pixel level	Column level

4.3.2 ALPIDE chips development

The CMOS Monolithic Active Pixels Sensors (MAPS) are often used in most of the current particle trackers. According to its advantage concerning granularity, material thickness, readout speed, power consumption, and radiation hardness, ALICE chooses the TowerJazz 0.18 μm CMOS Imaging Process of MAPS (ALICE Collaboration, 2014a) for the new ITS, called ALPIDE. It has been R&D for several years to meet ITS and MFT requirements. The high resistivity epitaxial layer provided by TowerJazz is about 1-6 kΩcm while its thickness can be expanded from 18 μm to 40 μm. Therefore, the depletion layer and the radiation hardness can be extended. Moreover, the charge collection efficiency and the SNR can be improved due to a located deep p-well inside the epitaxial layer.

ALPIDE has been developed for several prototypes during the R&D under the collaboration from CCNU (Wuhan, China), CERN, INFN (Italy), and Yonsei

(South Korea) to optimize the new chip corresponds to the ITS upgrade requirement. The various prototype of the ALPIDE and their specification are presented in Table 4.4.

In the next chapter, the prototype chips of the ALPIDE sensor will be characterized to obtain their detection performance.
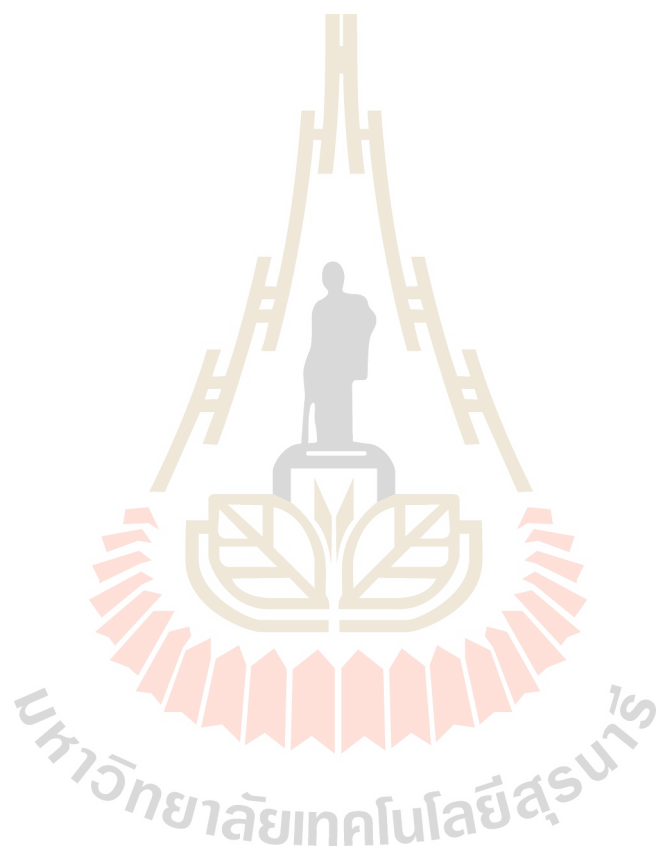
Table 4.4 The prototypes of the ALPIDE family and their goals (Rinella, 2017).

Submission	Prototype	Specification & Purpose
2012	Explorer	• pixel size: 20×20 μm^2 and 30×30 μm^2 (analogue readout) • chip size: 1.8×1.8 mm^2 • For: study of pixel geometry, starting material, and radiation
2013	pALPIDEss-0	• matrix: 64 512 • pitch size: 22×22 μm^2 • chip size: 11×1.8 mm^2 • in-pixel discrimination and buffering, zero suppression
2014	pALPIDE-1	• First full scale prototype • pitch size: 28×28 μm^2 • chip size: 15×30 mm^2 • four sectors with variants, 1 register/pixel, no final interface
8/2015	pALPIDE-2	• Full scale prototype • four sectors with variants, optimisation of circuits, integration in modules, no high speed serial output
10/2015	pALPIDE-3	• Full scale prototype • eight sectors with variants, all communincation features, no ADC, no temperature sensor
8/2016	ALPIDE	• Final chip

CHAPTER V

OPTIMIZATION OF SENSITIVE LAYER AND

CHARGE COLLECTION ELECTRODE

The ALPIDE sensors are the integrated of sensitive area and the readout circuit in the same die. To offer the most effective of the sensor, ALPIDE must be developed and optimized in the sensitive layer and the charge collection electrode independently of the readout circuit.

In this chapter, we will provide ALPIDE development and optimization. To determine the character and performance of the pixels, there will be characterized in the following parameter: 1) Spacing between the collection n-well and the surrounding p-well, 2) Collection n-well size, 3) Pixel pitch, 4) Epitaxial layer thickness and resistivity, and 5) Reverse bias voltage on the collection diode. The prototype used in this work is Investigator-0 provides 134 different pixel matrices of 20 μm to 50 μm thickness with analog readout.

5.1 Matrix charge collection efficiency

The sensor will be characterized by using soft X-ray sources or minimum ionizing particles (MIPs). The conversion process from X-rays emission is used to identify the energy loss and the signal of e-h pairs. The photon energy from soft X-ray source is close to the most probable energy loss of a MIP which is about 4.12 keV in a sensor of 20 μm thickness. This photon source is ^{55}Fe which emits the photon in two modes, 5.9 keV and 6.5 keV (Bé et al., 2006). The photon with

this energy can traverse in the silicon for 29 μm and 37 μm (Henke et al., 1993) that long enough for ALPIDE thickness. To assess the performance of prototypes from the ALPIDE development, the Matrix charge collection efficiency (MCCE) will be considered.

MCCE is defined as the ratio of the detected charge and the charge produced by an impinging particle. This observable is used to describe the performance of the sensor in term of the charge collection in a pixel. It depends on the sensor parameter, e.g., the pixel pitch, collection electrode geometry and the properties of the epitaxial layer (thickness and resistivity), as shown in Figure 5.1.
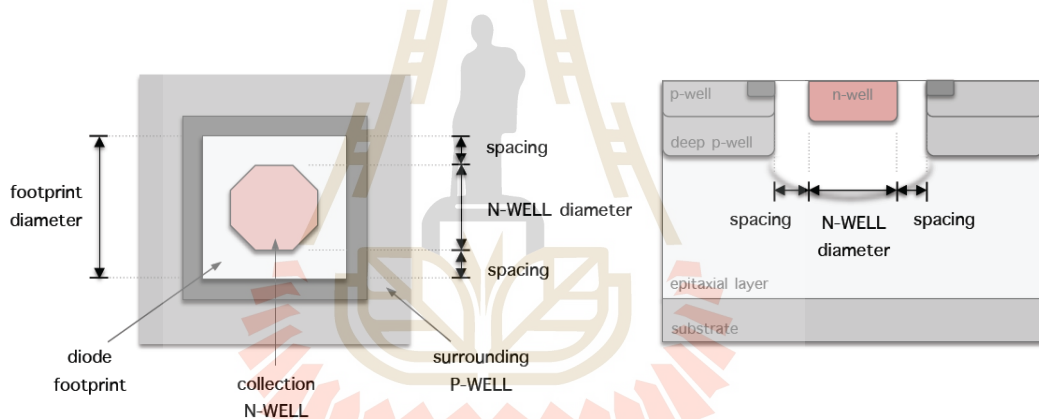
Figure 5.1 Schematical representation of the collection diode (van Hoorne et al., 2015).

MCCE can be measured by comparing the mean amount of collected charge when 5.9 keV ^{55}Fe photons are converted either inside or near the depleted volume and in the undepleted volume of the epitaxial layer. Therefore, the matrix charge collection efficiency can be expressed by:

$$\text{Matrix CCE} = \frac{\text{MPV of matrix signal}}{\text{MPV of single signal}}, \tag{5.1}$$

where matrix signal is a summation of the signals of an n × n pixel matrix centered

around the seed pixel and single-pixel cluster signal is the number of charges created by ionizing radiation in the sensor (shared from several pixels). The group of a pixel which shows a signal over the threshold is called a cluster.

Therefore, the matrix charge collection efficiency of the sensor will be measured on the following sensor parameters.

5.1.1 Spacing parameter

The geometrical parameter such as spacing between the n-well and the surrounding p-well influences the size of the depletion region, as well as the reverse bias. In this case, the ch_212 chip will be characterized by a certain pitch and n-well size. The variation of the spacing has been shown in the Table 5.1.

Table 5.1 Features of ch_212 chip with different spacing.

Label	Pitch	Electrode size	Electrode shape	Spacing
0	20	3	octagonal	1
1	20	3	octagonal	2
2	20	3	octagonal	3
3	20	3	octagonal	4
4	20	3	octagonal	5

The matrix signal distribution significantly shows the event of X-ray conversion occurred in the epitaxial layer. Almost all generated charge carriers are collected in the depletion zone. The enlargement of the space leads to the increasing of matrix signal regarding the higher V_{BB}.

The performance of pixel in term of the matrix charge collection efficiency will be improved due to the larger of the space because of the reduction for the single signal (shown in Figure 5.2 and 5.3). Moreover, the higher reverse bias

voltage can maximize the matrix CCE. The measurement results are shown in Figure 5.4.

(a) VBB-0.0

(b) VBB-1.0

(c) VBB-3.0

(d) VBB-6.0

Figure 5.2 Comparison of the matrix signal of ch_5 with various spacing values. Our results show the matrix signal distribution of a pixel with 20 μm × 20 μm octagonal pitch size and 3 μm n-well size at (a) VBB =0V, (b) VBB =-1V, (c) VBB= -3V, and (d) VBB= -6V.

5.1.2 N-well size

The optimization of the collection diode geometry one can be obtained by the investigation of the collection n-well size. The study of the n-well size, in this case, takes place on chip_212 with the precise spacing between the n-well and surrounding p-well and pitch size. The variation of the n-well size is shown in Table 5.2.

(a) VBB-0.0

(b) VBB-1.0

(c) VBB-3.0

(d) VBB-6.0

Figure 5.3 Comparison of the single signal of ch_5 with various spacing values. Our results show the single signal distribution of of a pixel with 20 μm × 20 μm octagonal pitch size and 3 μm n-well size at (a) VBB =0V, (b) VBB =-1V, (c) VBB= -3V, and (d) VBB= -6V.

Table 5.2 Features of ch_212 chip with different electrode size.

Label	Pitch	Electrode size	Spacing shape	Electrode
5	20	1	octagonal	3
6	20	2	octagonal	3
2	20	3	octagonal	3
7	20	4	octagonal	3
8	20	5	octagonal	3

The performance of a pixel sensor for different n-well size in term of the matrix charge collection efficiency shows that the increase of the n-well size will reduce the single signal. In the other hand, the higher reverse bias voltage can

Figure 5.4 Our comparison result of the matrix charge collection efficiency as a function of spacing for different reverse bias voltage.

increase the matrix signal up to a limit value of the reverse bias voltage. The measurement results are shown in Figure 5.5 and 5.6.

The observation results show that the enlargement of the n-well size leads to a reduction of the single signal. Moreover, the higher reverse bias voltage effect on the increasing of matrix CCE. The results are shown in Figure 5.7.

5.1.3 Pitch size

The implement of the collection electrode geometry and epitaxial layer properties can be studied by the increasing of the pixel pitch. In this case, the measurement of chip_5 with the certain spacing between the n-well and surrounding p-well and the same n-well size will be taken place. The variation of the octagonal pitch size is shown in Table 5.3.

The performance of pixel sensors with different pixel pitch size in term of the matrix charge collection efficiency shows that the enlargement of the pixel pitch will increase the single signal (shown in Figure 5.8 and 5.9). Moreover, the

(a) VBB-0.0

(b) VBB-1.0
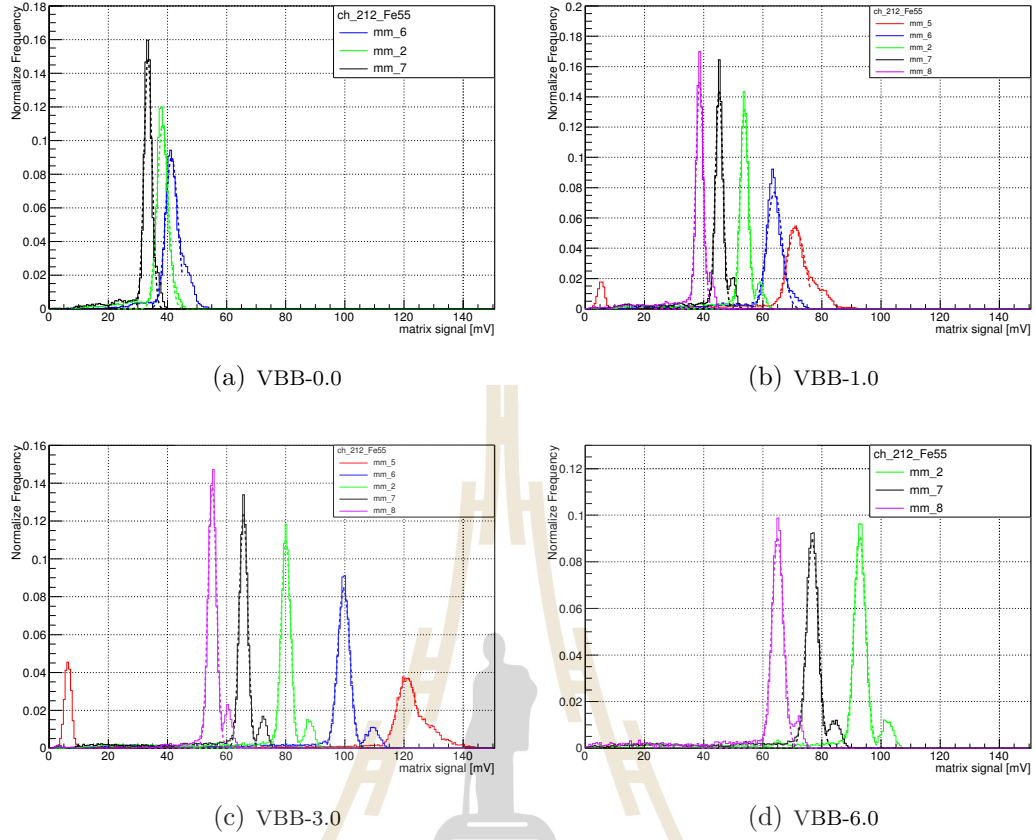
(c) VBB-3.0

(d) VBB-6.0

Figure 5.5 Comparison of matrix signal of ch_212 with various octagonal n-well size. Our results show the matrix signal distribution of a pixel with 20 μm × 20 μm octagonal pitch size and 3 μm spacing at (a) VBB =0V, (b) VBB =-1V, (c) VBB= -3V, and (d) VBB= -6V.

Table 5.3 Features of ch_5 chip with different pitch size.

Label	Pitch	Electrode size	Electrode shape	Spacing
34	20	3	octagonal	3
47	22	3	octagonal	3
80	28	3	octagonal	3

higher reverse bias voltage will reduce the matrix CCE. The measurement results are shown in Figure 5.10.

(a) VBB-0.0

(b) VBB-1.0
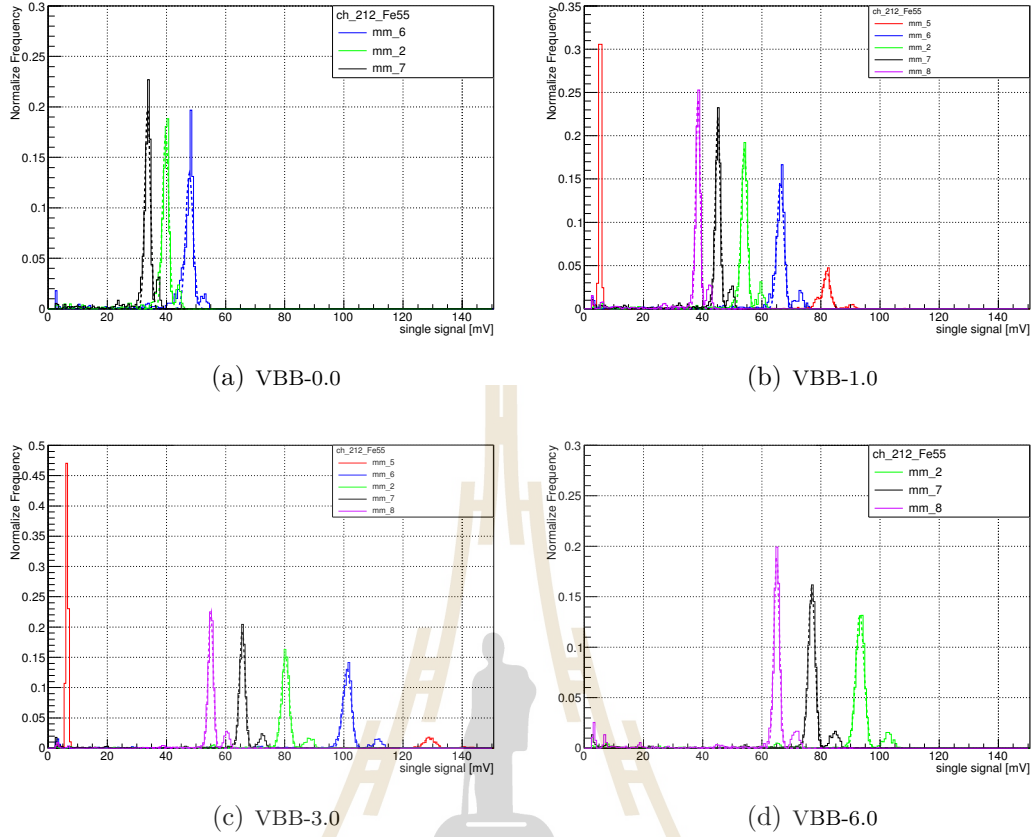
(c) VBB-3.0

(d) VBB-6.0

Figure 5.6 Comparison of single signal of ch_212 with various octagonal n-well size. Our results show the single signal distribution of a pixel with 20 μm × 20 μm octagonal pitch size and 3 μm spacing at (a) VBB =0V, (b) VBB =-1V, (c) VBB= -3V, and (d) VBB= -6V.

5.2 Calibration peak

In the measurement of the cluster signal, the highest signal from one pixel becomes dominant, called seed signal. For seed signal distribution, there are two significant peaks. The first one is the *collection peak* represents the MPV of the charge collected from the neighbor at the seed pixel that remains 35% to 50% of the total deposited charge. The smaller peak, called *calibration peak*, refers to the total charges collected in the seed pixel which deposited by the 5.9 keV photons inside the depletion volume. This photon can generate approximately 1640 *e-h* pairs. Both peaks depend on the size of the depletion region which relates to the
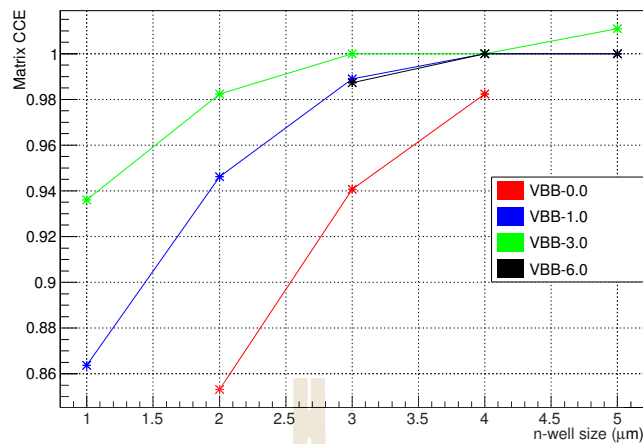
Figure 5.7 Our comparison result of the matrix charge collection efficiency as a function of n-well size for different reverse bias voltage.

following parameters.

5.2.1 Spacing parameter

The calibration peak as a function of spacing is related to the depletion region. The enlargement of space has an influent to the calibration peak shifts to lower while the increase of reverse bias can expand the calibration peak. The result is shown in Figure 5.11.

The increasing of space will extend the depletion region that leads to a reduction of the calibration peak.

5.2.2 N-well size

The calibration peak is more prominent with the more significant collection of n-well size because the depletion region will be extended with the increasing of n-well size, as shown in Figure 5.12.

The calibration peak is a decreasing function of the larger collection n-well
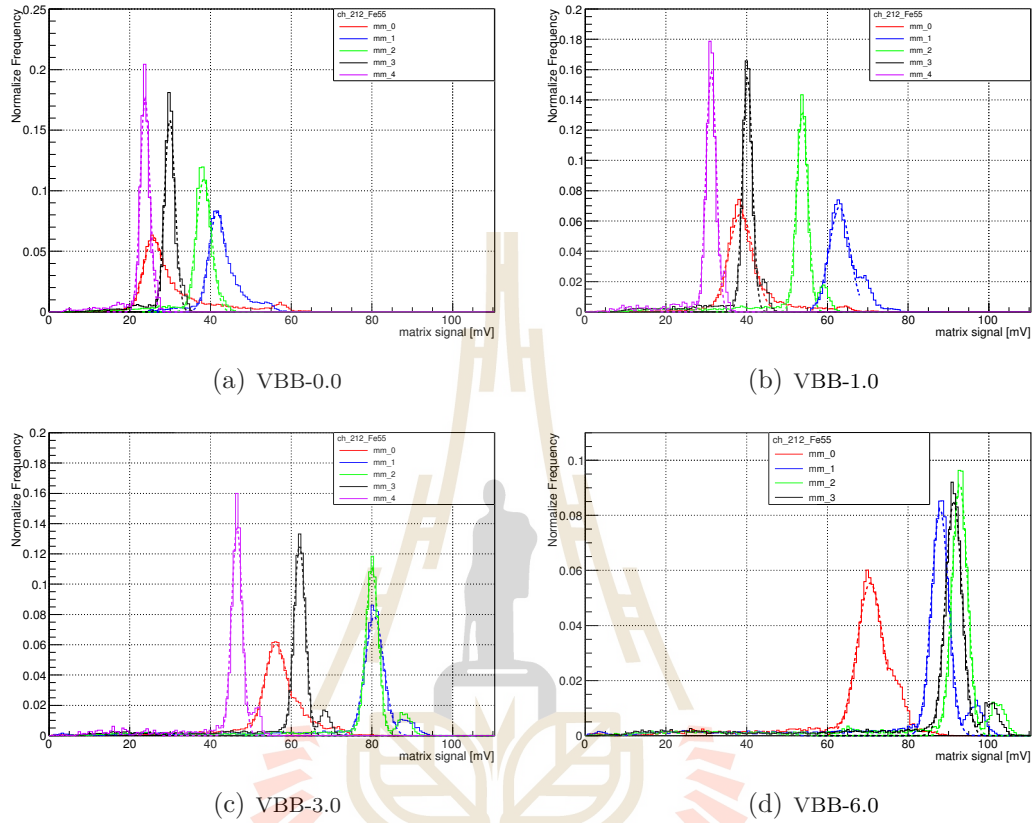
(a) VBB-0.0

(b) VBB-1.0
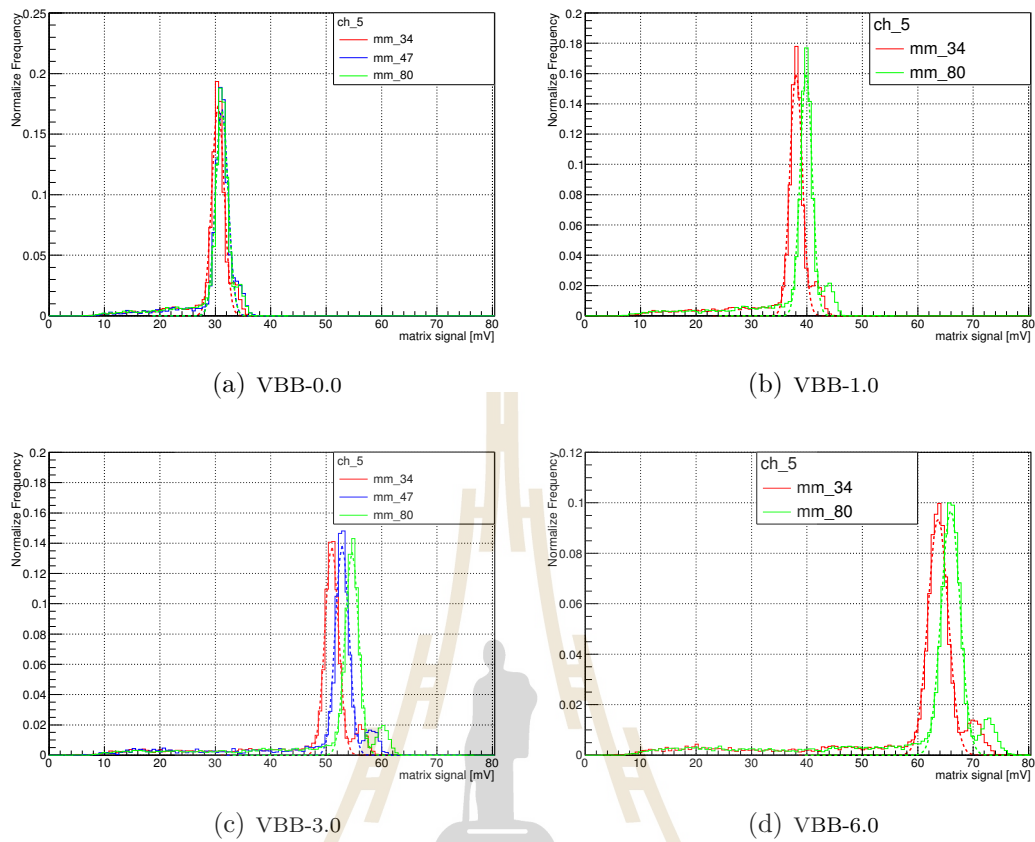
(c) VBB-3.0

(d) VBB-6.0

Figure 5.8 Comparison of matrix signal of ch_5 with various pixel pitch size. Our results show the matrix signal distribution of a pixel with 3 μm^2 n-well size and 3 μm spacing at (a) VBB =0V, (b) VBB =-1V, (c) VBB= -3V, and (d) VBB= -6V.

size because the enlargement of collection n-well can reduce the number of the pixel with shared charge.

5.2.3   Pitch size

In the case of three different pixel pitches with the same collection electrode geometry, the calibration peak is remained not to change. Thus, the pixel pitch does not affect with the pixel input capacitance, but the larger of the reverse bias can increase the calibration peak signal of the pixel (see in Figure 5.13).
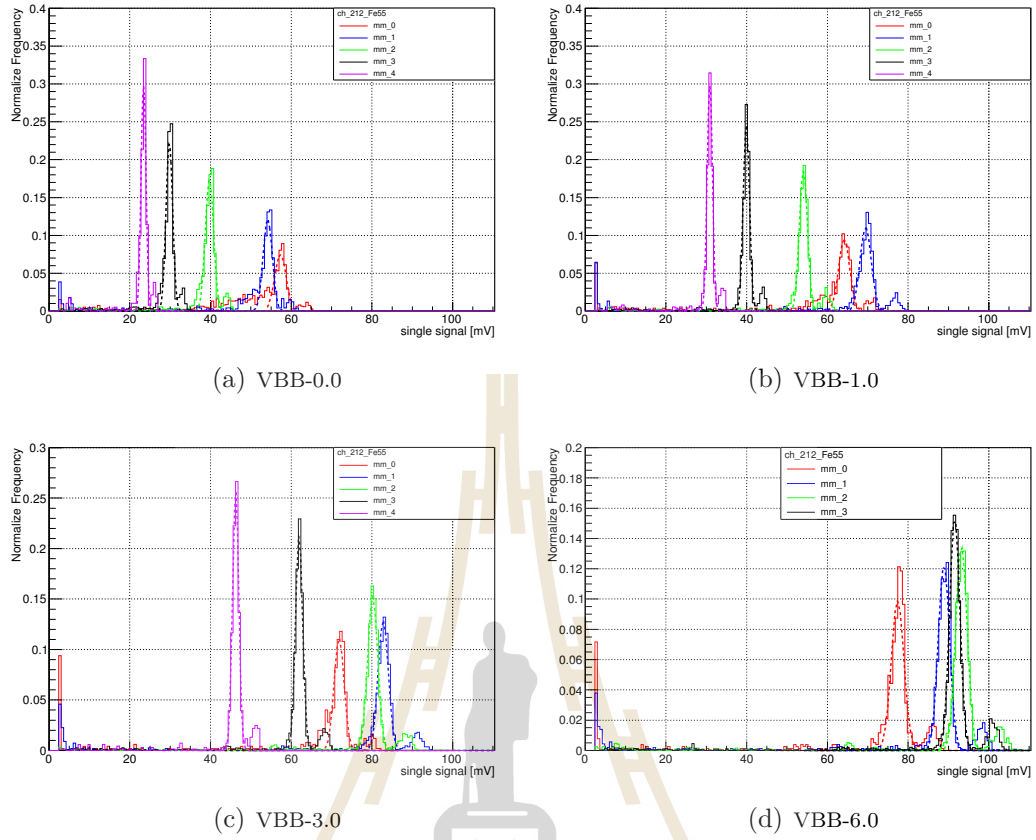
(a) VBB-0.0

(b) VBB-1.0
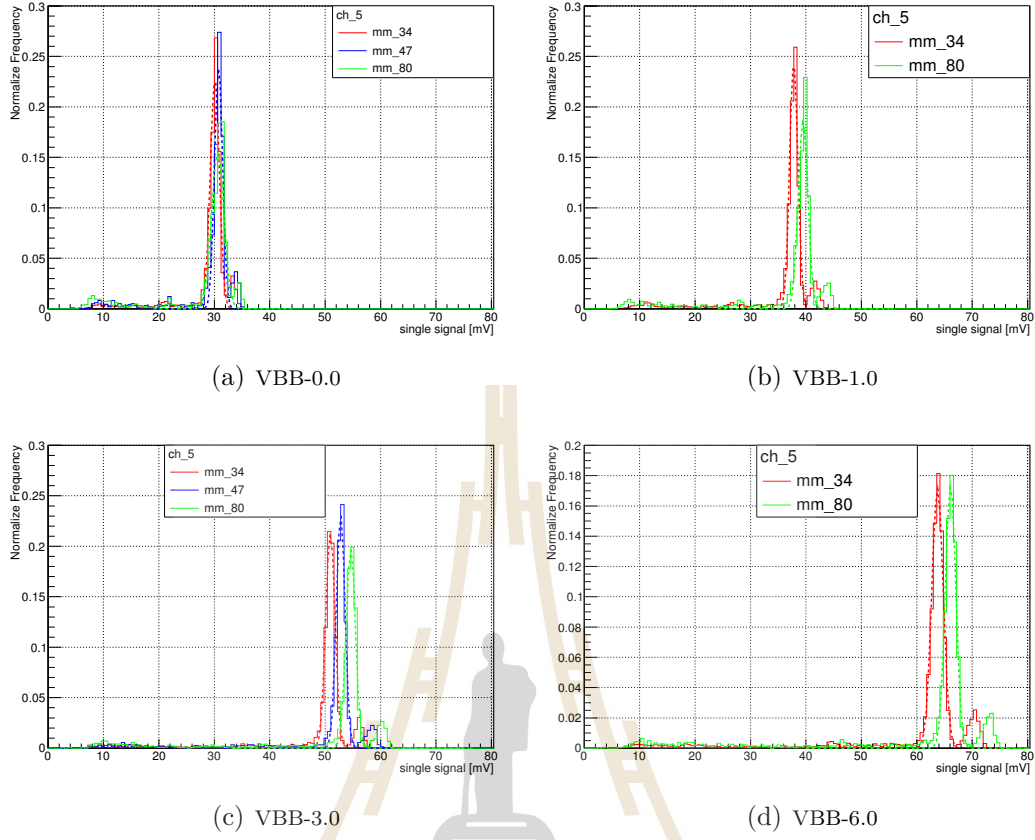
(c) VBB-3.0

(d) VBB-6.0

Figure 5.9 Comparison of single signal of ch_5 with various pixel pitch size. Our results show the single signal distribution of a pixel with 3 μm^2 n-well size and 3 μm spacing at (a) VBB =0V, (b) VBB =-1V, (c) VBB= -3V, and (d) VBB= -6V.

5.3 Relative depletion region analysis

The relative depletion volume (r_{depl}) is defined by the ratio of the number of events in which the X-ray conversion took place within the depletion volume (N_{depl}) that all deposited charge is collected by a single pixel and the number of total events in which the photoconversion occurs within the epitaxial layer (N_{tot}). r_{depl} can be expressed by

$$r_{\mathrm{depl}} = \frac{N_{\mathrm{depl}}}{N_{\mathrm{tot}}}. \tag{5.2}$$

The number of events refers to the integrals below each of N_{depl} and N_{tot} peaks. These peaks can be estimated by fitting their contribution with a function
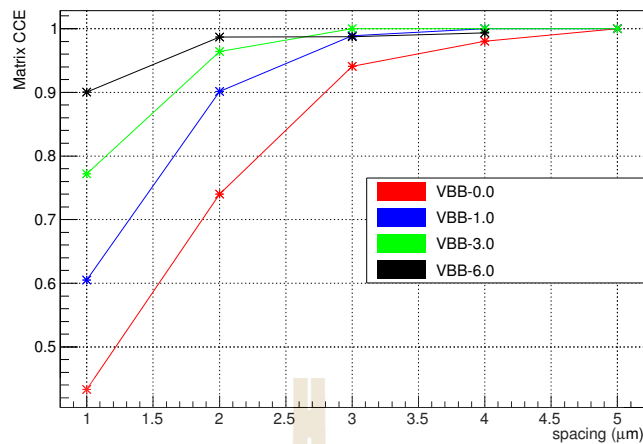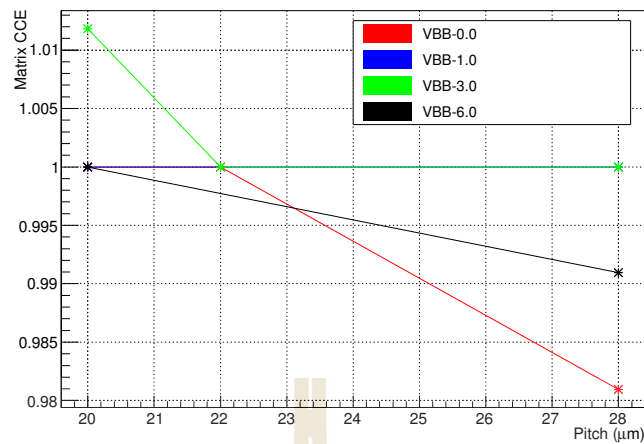
Figure 5.10 Our comparison result of the matrix charge collection efficiency as a function of pixel pitch size for different reverse bias voltage.
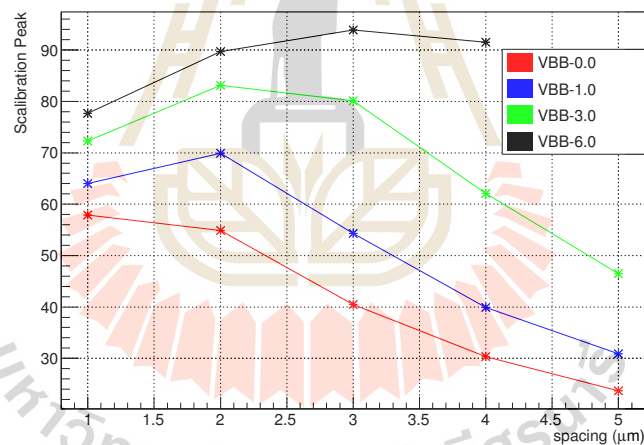
Figure 5.11 Our comparison result of the calibration peak as a function of spacing for different reverse bias voltage.

constructed of two overlapping Gaussian distributions. These following parameters are used to describe the relative depletion volume of the sensors which depends on the following parameters.
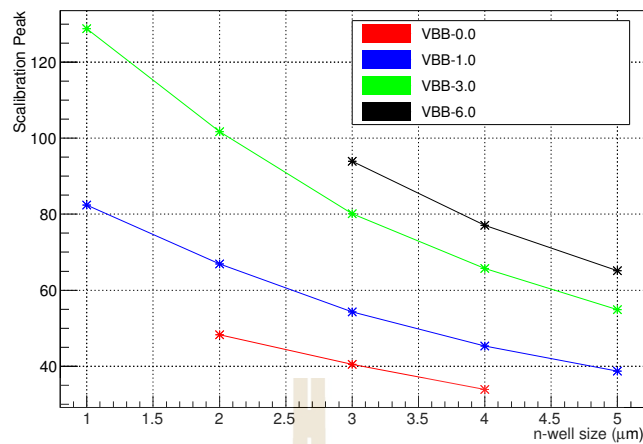
Figure 5.12 Our comparison result of the calibration peak as a function of n-well size for different reverse bias voltage.
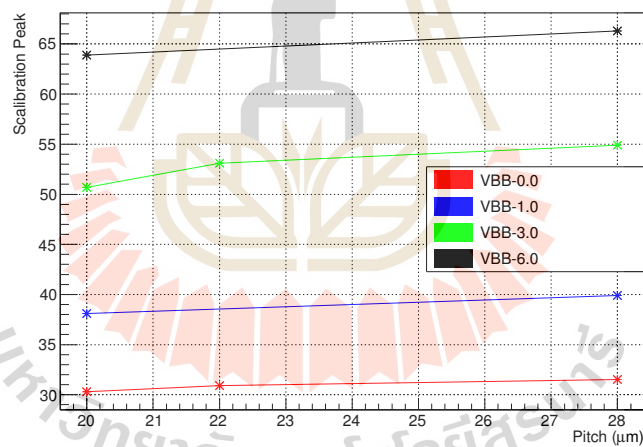
Figure 5.13 Our comparison result of the calibration peak as a function of pixel pitch size for different reverse bias voltage.

5.3.1 Spacing parameter

The depletion region is related to the spacing between n-well and surrounding p-well. The enlargement of the spacing will increase the depletion region. As well as the reverse bias voltage, it has an influence on the extension of the deple-

tion region. Hence, the ratio of the integration of seed signal and matrix signal refers to the amount of the active area, called the relative depletion volume.

Figure 5.14 shows the estimation of the relative depletion volume as a function of spacing for various reverse bias voltage. The relative depletion volume is increased when V_{BB} is increasing. However, the size of the depletion region is not only depending on the reverse bias, but also on a spacing between the n-well and the surrounding p-well. In the other hand, the enlargement of the depletion region leads to the reduction of the pixel input capacitance C_p which can be estimated using Eq. 5.3:

$$C_p = \frac{1640e^-}{V_{calib}^{gc}},$$

(5.3)

where V_{calib}^{gc} is the calibration peak.
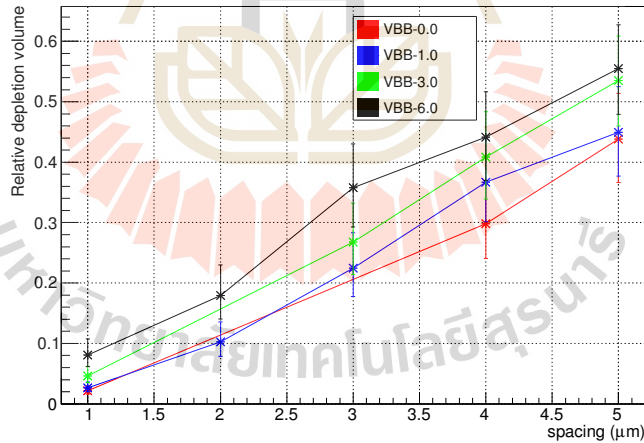
Figure 5.14 Our comparison result of the relative depletion volume as a function of spacing for the different reverse bias voltage.

The reverse-substrate bias voltage V_{BB} influences the extension of the depletion region. The increasing of the V_{BB} will enlarge the depletion volume that leads to a reduction of the pixel input capacitance. Thus, the charge collection

process is more efficient. The larger depletion volume leads to a more significant number of event that the X-rays can be absorbed in the depletion region.

5.3.2 N-well size

The increase of n-well size can extend the size of the depletion region which indicates a change of the pixel input capacitance C_p. The input capacitance of the pixel will be reduced corresponding to the larger n-well size as well as V_{BB}.

The increasing of the n-well size gives a more prominent of the seed signal. The measurement result in Figure 5.15 shows that the distribution of the same collection n-well size is the increasing function of the larger V_{BB}.
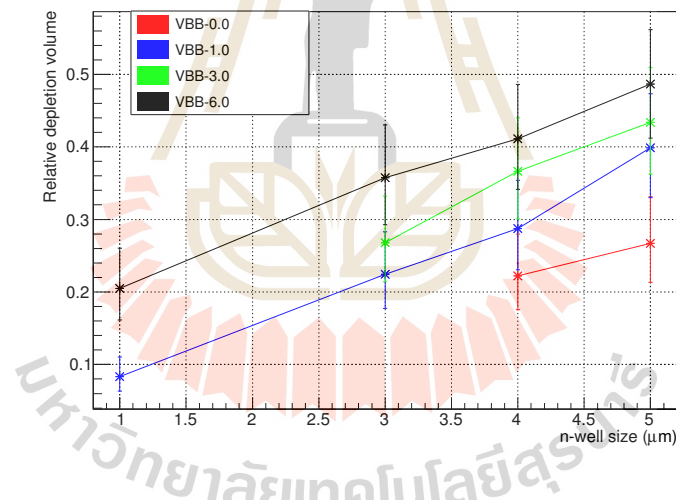
Figure 5.15 Our comparison result of the relative depletion volume as a function of n-well size for the different reverse bias voltage.

The enlargement of the collection n-well size presents the calibration peak more prominent. Because the increase of the collection n-well size can increase the relative depletion volume. The estimation of the relative depletion volume for the four different pixels as a function of the collection n-well can be identified that increasing of the n-well size leads to an enlargement of the depletion volume for

all reverse bias values. Therefore, the size of the depletion region does not only depend on the reverse bias, but also geometrical parameters such as collection n-well size.

5.3.3   Pitch size

The increasing of the pixel pitch with maintaining the collection electrode geometry remains unchanged for the seed signal (calibration peak). It indicates that the pixel pitch has no effect on the pixel input capacitance, but the distinctness of the collection peak of seed signal will be reduced due to the charge sharing effect. In the same context, the reduction of V_{BB} gives the same trend of seed signal with a larger pitch.

Therefore, the case of three different pixel pitches with the same collection electrode geometry give the same position of the calibration peak. In this consequence, the larger pixel pitch size does not affect the pixel input capacitance, but the increase of the reverse bias can improve the magnitude of the calibration peak signal. The measurement is shown in Figure 5.16.

Thus, the relative depletion volume can be expected to decrease when increasing the pixel pitch. At the same time, the more substantial reverse bias leads to an extension of depletion volume.

5.4   Summary

The study of the influence parameter of the pixel sensor is to provide the required charge collection efficiency. A large reverse bias on the collection diode performs both a reduction of pixel input capacitance and charge sharing effect as a result of an increased depletion volume. For the pixel pitch is raised, the charge will be shared over more pixels due to the involved increase of the non-depleted
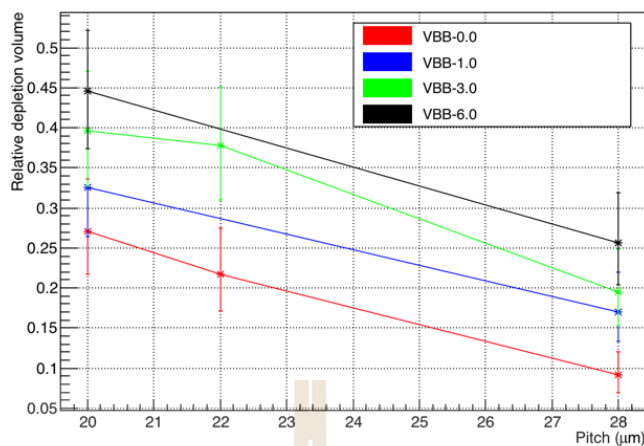
Figure 5.16 Our comparison result of the relative depletion volume as a function of pixel pitch size for the different reverse bias voltage.

volume in the epitaxial layer. In case of pixels with small collection n-well and large spacing between the collection n-well and the surrounding p-well, they gain more signal from an increase of the reverse substrate bias regarding the reduction of pixel input capacitance.

The measurement results of all observable parameters can be used to provide the optimization of the sensor parameters, e.g., pixel pitch, collection electrode geometry, and epitaxial thickness. From such settings, the ALPIDE generation can be developed for the best performance of the pixel detector. The optimized parameters of the sensitive layer and the charge collection electrode for the ALPIDE development are summarized in Table 5.4.

Table 5.4 ALPIDE series developments.

Parameters	pALPIDE-1	pALPIDE-2	pALPIDE-3	ALPIDE
Pixel matrix	512 rows $\times$ 1024 columns			
Pixel pitch size	28 μm $\times$ 28 μm		29.24 μm $\times$ 26.88 μm	
The collection n-well diameter	2,3 μm	2 μm	2 μm	2 μm
Collection electrode to P-well spacing	1,2,4 μm	2,4 μm	2,3 μm	3 μm
Epitaxial layer thickness	18, 25, 30 μm	25, 30 μm	18, 25, 30 μm	25 μm

CHAPTER VI

FULL SCALE PROTOTYPE pALPIDE-3

CHARACTERIZATION

In this chapter, we will present the testing of the full-scale prototype sensors pALPIDE-3. The main goal is to study the characteristic of the sensor such as pixel by pixel threshold variation, noise behavior, detection efficiency, and spatial resolution to determine its performance.

The first part of this chapter is dedicated to a description of the ALPIDE sensor readout system. Secondly, the laboratory measurement for the characteristic of pALPIDE-3 will be presented on the behavior concerning the bias parameters. The last part of the chapter will provide the performance of the prototype via the test beam.

6.1 Readout System

The readout system of pALPIDE prototype consists of a single DAQ card (size 12 cm×10 cm) which connect to the pALPIDEfs carrier board (see Figure 6.1) through a PCI Express connector. It is used for the functional test in the laboratory measurements. The controlled signal generated from the computer will be sent to the DAQ card via a LEMO connector to ensure proper synchronization of the system.

The DAQ architecture is operated by three different clock signal derived to the testing components: 80 MHz clock to the FPGA modules, 80 MHz clock to
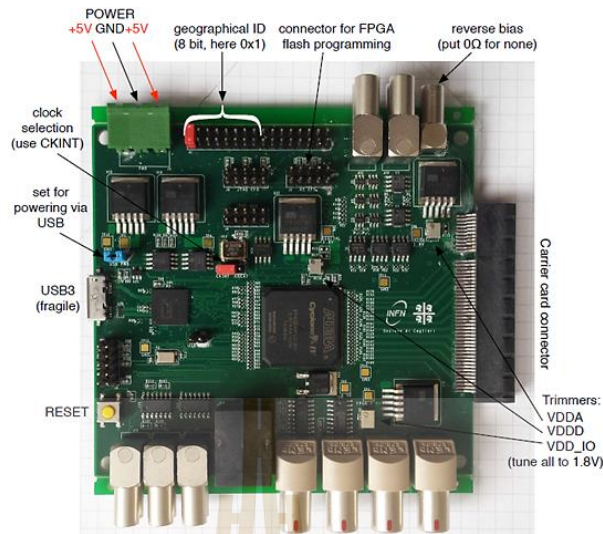
Figure 6.1 pALPIDEfs readout DAQ card (ALICE Collaboration, 2012).

the FX3, and 40 MHz clock to the sensor.

The front-end controlled parameters have been studied for the influence on the various V_{BB} and the threshold parameters. The front-end parameters used in this testing are given below.

- **PMOS Cascode Voltage (V_{CASP})**: used to amplify an analog circuit. The default setting of V_{CASP} is 0.6V

- **Diode Reset (V_{RST})**: used to prevent a larger voltage drop in a circuit. It was set to 1.6V (above a minimum circuit voltage around 1.4V) as default

- **Reverse Substrate Bias Voltage (V_{BB})**: used for the extension of the depletion region which can be operated between 0–6V

- **Charge Threshold Setting (I_{THR} and V_{CASN})**: main parameters influence on charge threshold and noise. The reduction of the threshold is corresponding to the increase of V_{CASN} and a decrease of I_{THR}.

These parameters above will be adjusted as the input parameter to see the

behavior of the prototype sensor. Next, the functional testing of the sensor will be explained.

6.2 Laboratory Measurements

pALPIDE-3 chips are tested in the laboratory to first check for their proper working. These chips are mounted on carrier board which connected to the read-out boards linked by USB cable to a computer, as sown in Figure 6.2.
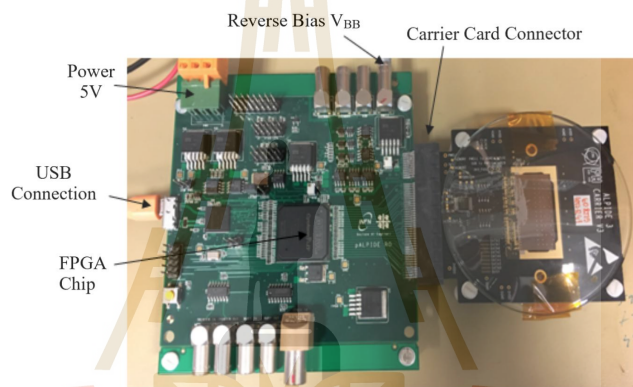
Figure 6.2 DAQ card read-out connected to the carrier boad of pALPIDE-3 (Keil, 2014).

The DAQ board is controlled through the ALPIDE software provided all functionality test. The measurement can be done with a dedicated command line for each function. The main functions to perform the chip testing are described in the following (Keil, 2014)

- Powering test: measurement of power consumption

- FIFO scan: quick test to verify the communication with the control interface of the chip

- DAC scan: measurement of the onboard voltage output obtained by looping over the values from 0 to 255 injected charges for each digital-analog

converter (DAC)

- Threshold scan: measurement of the number of hits for each charge point performed by 50 analog injections (measurement limit to 1% of the pixel)

- Noise scan: evaluation of the number of noisy pixels returned from 100k events of random triggers

6.2.1 Threshold Measurement

The charge threshold of the front-end circuit of pALPIDE-3 is the most important characteristic for the chip performance. The values obtained from the threshold refer to the detection efficiency and the quality of the position resolution due to a reduction of the number of cluster multiplicity. The charged threshold can be determined by using the front-end bias settings (I_{THR} and V_{CASN}) to perform negative voltage step on the injected capacitor (C_{inj}) that refers to the pixel input capacitance (C_p). Then, the range of test charges has been produced and injected in the pixel. A range of test charge is defined by

$$Q_{inj} = \frac{C_{inj}}{V_{REF}/step} \quad [C]$$
$$= \frac{C_{inj}}{V_{REF} \cdot 1.6 \times 10^{-19}} \quad [e^- /DACstep], \tag{6.1}$$

where C_{inj} is the capacitance depends on the amplitude of the voltage pulse, V_{REF} is the voltage provides a resolution of 256 steps over.

If a range of test charge Q_{inj} is injected for N times in a pixel and number of times the pixel has registered a hit N_{hit} is measured, then the charge threshold can be measured in term of the response function $r(Q_{inj})$ of the front-end circuit.

$r(Qinj)$ is given in the following equation (van Hoorn, 2015).

$$r(Q_{inj}) = \frac{N_{hit}(Q_{inj})}{N}.$$

(6.2)

The threshold distribution of pixel depends on the bias setting parameters will be presented in the next section. The threshold measurement of pALPIDE-3 will be performed for 1% (as the sample) of each pixel matrix and the nominal setting for various V_{BB} are separated in Table 6.1.

Table 6.1 Nominal DAC values for three reverse substrate bias voltages V_{BB}.

DAC	$V_{BB} = 0$	$V_{BB} = 3$	$V_{BB} = 6$
I_{THR}	50	50	50
I_{DB}	29	29	29
I_{RESETD}	147	147	170
V_{CASN}	52	107	137
V_{CASN2}	64	119	149
V_{RESETP}	117	117	117
V_{CLIP}	0	60	100
$STROBE\_B$	10	10	10

6.2.2 Influence of I_{THR} and V_{CASN} for charge threshold

The thresholds distribution of the pixel chips depends on the varying of the front-end bias parameters I_{THR} and V_{CASN}. The measurement results show that the threshold increases almost linearly with increasing I_{THR}. Whereas, the increasing of the V_{CASN} leads the threshold slightly reduce. The pALPIDE-3 chip threshold distribution as a function of both bias parameters are presented in Figure 6.3.

From the results, the increase of I_{THR} leads to a high pulse and narrow width. In contrast, the increase of V_{CASN} effects to the rise of the baseline volt-

(a)

(b)
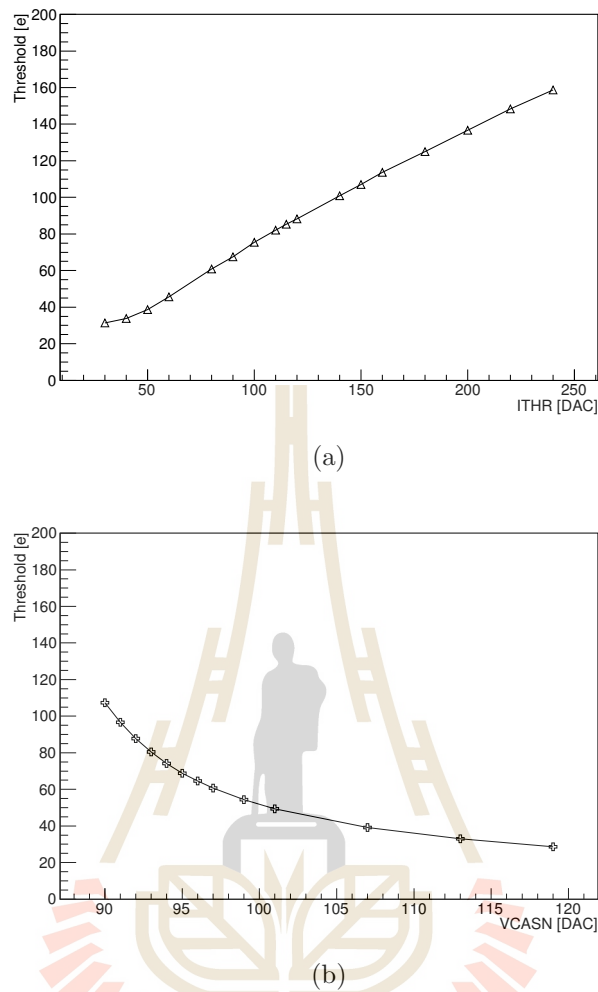
Figure 6.3 Threshold distribution plotted with the increasing of (a) I_{THR} and (b) V_{CASN}.

age closer to the critical voltage for driving the output node. Thus, the charge threshold will be increased with ascending I_{THR} and reducing V_{CASN}.

6.2.3 Fake-hit rate

One of the critical property of the pixel chip, regarding the chip performance, is the fake-hit rate. It is produced from a few pixels that do not exhibit a response function. The fake hit rate is the rate at which pixels show a hit even without any providing particles. Due to its strong effect on the performance of

tracking device, the fake hit rate is limited under 10^{-5}/event/pixel leads to an occupancy of 5 hits/event/cm^2 required by the ALICE ITS upgrade. According to the time-dependent of fake-hit, the larger integration time will increase the probability of a registered hit. The average fake-hit rate R_{FH} is calculated by the following

$$R_{fh} = \frac{N_{fh}}{N_{pix} \cdot N},\qquad(6.3)$$

where N is the number of recorded events (120000), N_{pix} is the number of pixels in a sector (i.e., $512/8 \times 1024$), and N_{fh} is a total number of fake-hit pixels in each sector. In the next section, the influence of I_{THR} and V_{CASN} will be discussed.

6.2.4 Influence of I_{THR} and V_{CASN} for Fake-hit rate

The fake-hit rate as a function of I_{THR} and V_{CASN}, shown in Figure 6.4(a), is seen that it drop with increasing I_{THR}. According to the higher I_{THR}, it can increase the threshold represents the pixel has to reach the higher threshold level in order to be recorded as a hit. Hence, the number of fake-hit, equivalent value of R_{fh}, is reduced. In the other hand, the decrease of the threshold due to the increase of V_{CASN} (see Figure 6.4(b)) leads to higher fake hit rate. Because the relative baseline voltage of increasing V_{CASN} will shorter exceed the critical voltage and produces more hit. Figure 6.4 shows fake-hit rate distribution as function of I_{THR} and V_{CASN} measured at $V_{\mathrm{BB}} = 3$V. The results show that the increase of the I_{THR} will reduce the fake-hit rate while the increase of the V_{CASN} will increase the fake-hit rate.
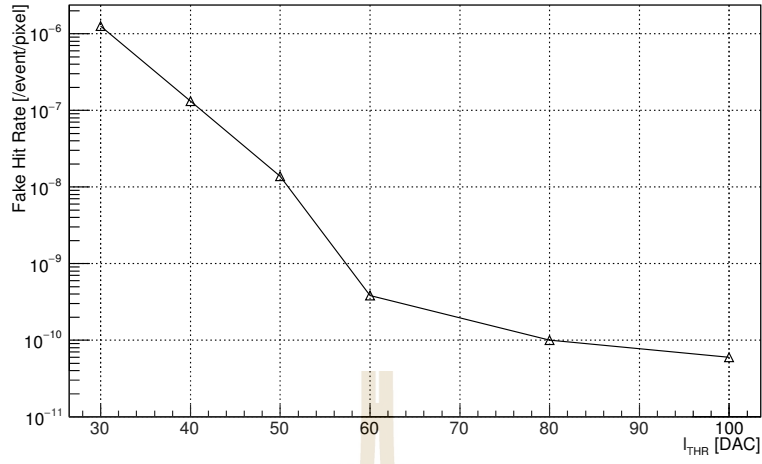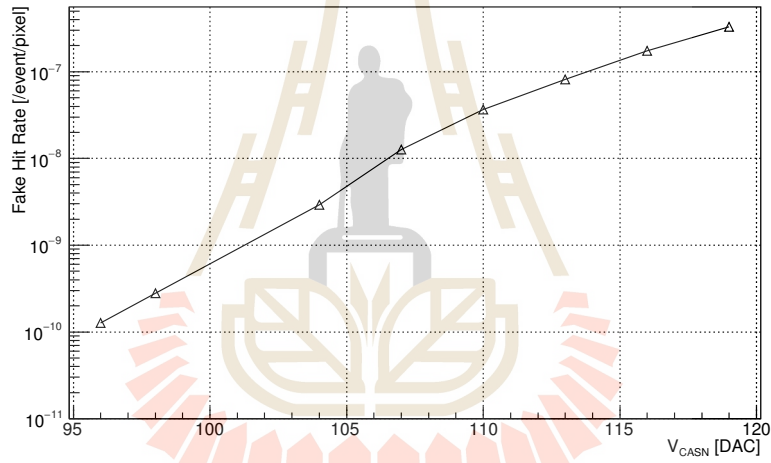
Figure 6.4 Fake-hit rate plotted with the increasing of (a) I_{THR} and (b) V_{CASN}. They are measured at $V_{\text{BB}} = 3\text{V}$.

6.2.5 Summary

The most essential biasing parameters are the I_{THR} current and the V_{CASN} voltage. As a result, decreasing the I_{THR} value reduces the electron threshold. It indicates that the threshold increases as a function of the I_{THR} current. The threshold corresponds to the minimum charge collection for a pixel to be registered as a hit. On the other hand, a lower V_{CASN} voltage leads to the same result. For the fake-hit rate, the results are in the opposite. This measurement help to determine

which is the optimized values of I_{THR} and V_{CASN}.

6.3 Test beam measurement

In this section, we will study the sensor performance in terms of the detection efficiency, spatial resolution, and environmental effects to understand, predict, and optimize the chip behavior. To obtain the characteristic response of the prototype, it will be tested with the test beam. The general information of the test beam analysis will be presented.

6.3.1 Experimental setup

The test beam has been set up at CERN PS with a pion beam of 6 GeV/c to characterize pALPIDE-v3 chips. A set of testing chip, called telescope, is surrounded by two scintillators at the front and at the back of the scintillators which are used as a trigger for the data taking. On the Figure 6.5 the beam is coming from the left, crosses the two scintillators (in black), the telescope and the final scintillator. The telescope composed of 7 planes of pALPIDE-3, as shown in Figure 6.6. The chips are inserted in three boxes to shield them from the light (black boxes in the bottom of the picture), while the read-out electronics are visible in the figure. Two separate boxes on the left and the right contain each three reference planes of the sensor, which are at 18 mm distance from each other. The box in the center contains the DUT called DUT for Device Under Testing), which is at 36 mm distance from the closest reference planes. This setup allows replacing the DUT without moving the reference planes. To avoid too much material and, hence, multiple scattering between the DUT and the reference planes, the boxes have a hole in the area correspondent to the sensors that is covered with aluminum foils. A back-bias of -3 V is applied to the reference planes

to improve their performances.
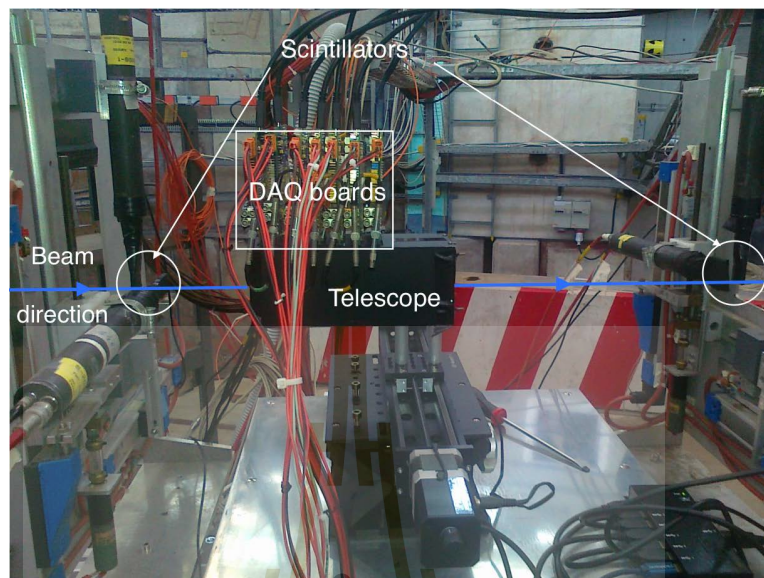
Figure 6.5 Experimental setup for test beam at PS (Kofarago, M., 2016).

Figure 6.6 Telescope setup at CERN PS (Kofarago, M., 2016).

6.3.2   EUTelescope framework

The propose of test beam measurements is to characterize the sensor using the tracking information. For this reason, during the measurement, the chip which is being tested (DUT) is placed between tracking planes. The whole setup is

adjustable manually or remotely in x and y to the center of the beam, called telescope (see Figure 6.7). The data-taking is done by EUDAQ software designed for data taking during the test beam. It provides a run control window to control chip powering, and configuration and a log window display information on the current run status. The data taking is automatic, and the setting files indicate the parameter values to use for each run. It stops and goes to the next run when the specified number of events is reached. Some plots are updated online such as hit maps so the user can check if data is recorded.
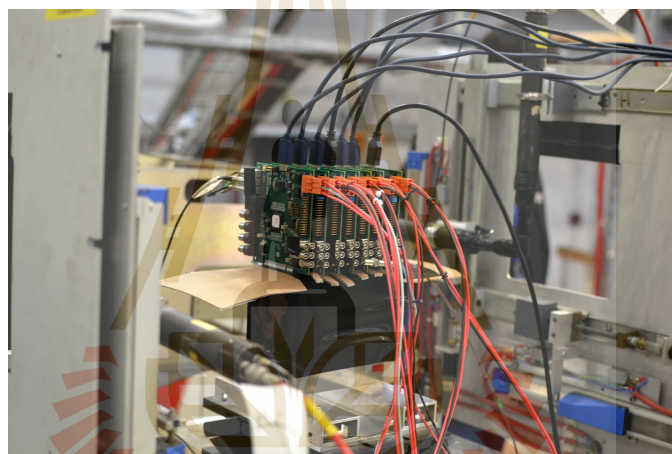
Figure 6.7 Telescope data-taking setup (Kofarago, M., 2016).

The data taken from EUDAQ will be analysed with EUTelescope software. It is a generic pixel telescope data analysis framework provides several processors implementing algorithms necessary for a full track reconstruction and data analysis of beam test experiments. The analysis method is summarized in the Figure 6.8. The raw data from each plane of the telescope are converted in the LCIO format, a Linear Collider IO event-based data format. Then, the clusters are detected and their hits are calculated. Subsequently, hits in the planes are written in the global reference system of the telescope using the information passed through the gear file, that contains the geometry description of the telescope. The alignment parameters

are calculated from straight tracks. The aligned hits are then used to construct tracks, the fitting procedure, in this case, uses broken lines. Subsequently, the reconstructed tracks are associated with a hit in the DUT in order to perform the final analysis.
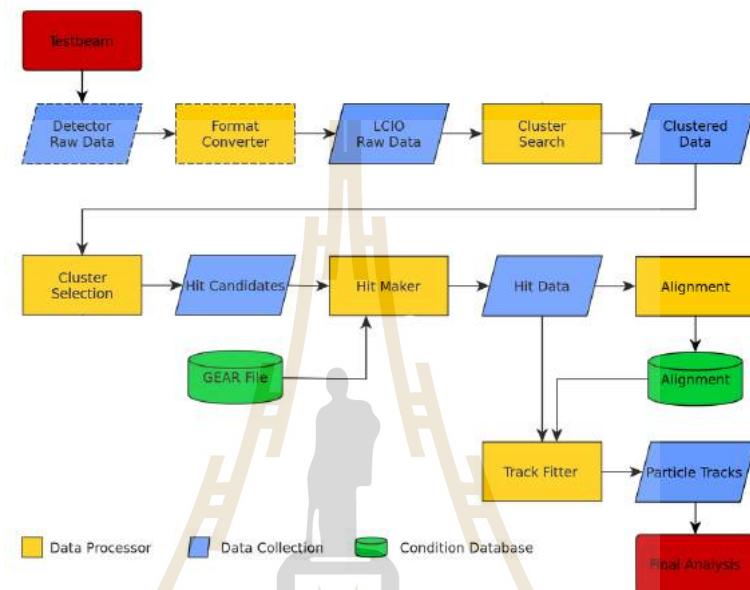
Figure 6.8 Diagram of the analysis steps of EUTelescope.

The main goal of the analysis is to calculate the detection efficiency, the spatial resolution, the cluster size and the noise occupancy of the chip. Tracks are fitted to the hits in the outer planes, and the tracks are interpolated to the DUT as can be seen in Figure 6.9. In the DUT hits are then matched to the tracks, and the detection efficiency and spatial resolution of the chip is calculated. Details of the calculation can be seen in the nest section.

In the analysis method, the raw data files generated from the EUDAQ software are evaluated for the run is noise or data. In case of noise, we will calculate the noise occupancy then the raw hitmaps including hot pixels are plotted. If it is a data run, then we go through the following procedure :

- measurement of cluster and correlation between the cluster of the pixels
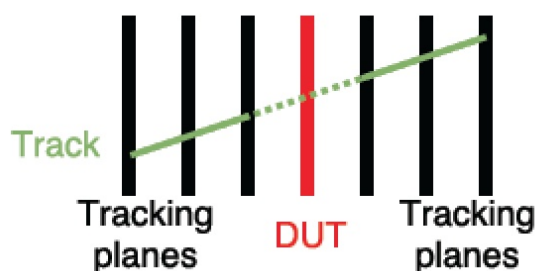
Figure 6.9 Schematic drawing of the tracking principle (Kofarago, M., 2016).

- calculation of the center of Hit

- performing the precise reconstruction by tuning up the alignment parameters

- calculation of shift in x and y direction and rotation around z will be calculated

- tracks reconstruction, fitted to the hits

- calculation of efficiency, resolution, and cluster size obtained from the measurement

6.3.3 Detection efficiency

The detection efficiency ϵ_{det} is the probability of particle which can be detected in the sensor. It is determined by two effects: first, the charge collected in the seed pixel which depends on the particle type and energy; second, the charge threshold. Consequently, lowering the threshold is beneficial for the detection efficiency, which is limited by the involved increase of the fake-hit rate.

The detection efficiency is measured using MIPs from a test beam facility move forward to the several planes of the sensor, called telescope. This telescope is formed by several high-resolution position sensitive detectors, the so-called ref-

erence planes. The device-under-test (DUT) is typically placed in the center of the telescope. The detection efficiency of the DUT is evaluated as follows (Xu and Ullrich, 2012):

$$\epsilon_{det} = \frac{\text{Number of tracks associated to a hit in DUT}}{\text{Number of tracks crossing DUT}}. \tag{6.4}$$

The detection efficiency results have been obtained from telescope equipped with pALPIDE-3 chips as a DUT. During the measurement, the reference planes are set at a fixed value of the applied bias while DUT can be varied. The hit information obtained from the reference planes will be used for track fitting. The analysis has been performed using the EUTelescope framework in considering of the multiple-scattering effects in all planes.
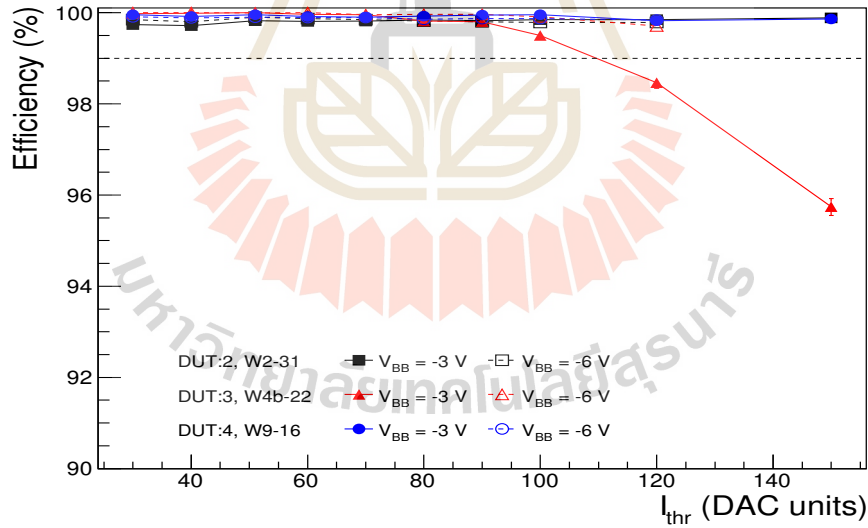
Figure 6.10 Change of detection efficiency with increasing of I_{THR}.

Figure 6.10 presents the results for the detection efficiency as a function of I_{THR} and Figure 6.11 presents the results as a function of V_{CASN} for two values of reverse substrate bias, measured with a 6 GeV pion beam at CERN PS.

The detection efficiency ϵ_{det} determined by the charge threshold of DUT
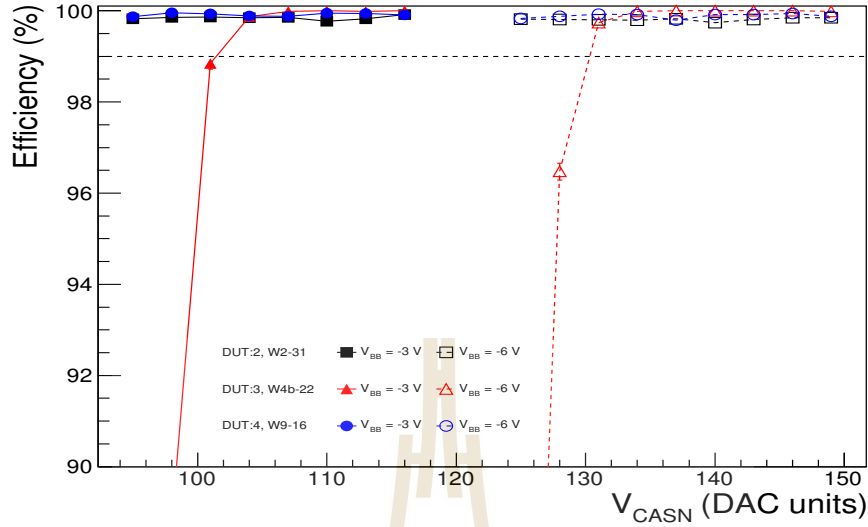
Figure 6.11 Change of detection efficiency with increasing of V_{CASN}.

depends on increasing of I_{THR} and V_{CASN}. The ϵ_{det} decreases with increasing I_{THR} while increases with increasing V_{CASN}. Thus, the front-end bias settings do not influence the charge collection process. For V_{BB}, it influences the extension of the depletion region effected on the junction capacitance C_d and the characteristics of the charge collection process. Hence, an increase of V_{BB} has been increased the Q/C ratio of the sensor and consequently the detection efficiency.

6.3.4 Average cluster size

As a charged particle passes through the epitaxial layer in the monolithic sensor, it creates electron-hole pairs. These electrons and holes are then collected on the front and back of the sensor, where they are registered at the corresponding pixel. The beam particle comes in with a certain angle, θ, in both X and Y directions, which determines the number of pixels that give a signal through the

formula

$$NP = \frac{th}{PR} \cdot \cos\theta, \qquad (6.5)$$

where NP is the number of pixels that give a signal, PR is the pixel resolution, and th is the thickness of the epitaxial layer. A clear picture of the process of a charged particle passing through a sensor can be seen in Figure 6.12. There is also some amount of noise from cosmic radiation, scattered particles, and other sources, that can alter the number of pixels fired.
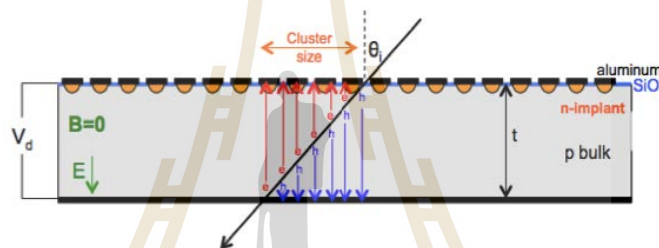
Figure 6.12 How a cluster of pixels is formed through creation of electron-hole pairs as a charged particle passes through the sensor (Source: Gregor, Ingrid-Maria. Detectors for High Energy Physics, Summer Student Lecture, 2013).

Studying the resolution of the sensors for different cluster sizes can give information about how accurately the sensors operate as the cluster size grows larger. Since the good resolution is an important feature of tracking detectors, this could help in determining a track's actual position and further improve the qualification of a DUT. The residual for a sensor plane is the difference of location for the fitted track and the actual hit of the particle. The resolution is here defined as the root mean squared (RMS) of the residual distribution. Such a residual distribution with a fitted Gaussian can be seen in Figure 6.13. The resolution is then the RMS value given in the statistics box to the right.
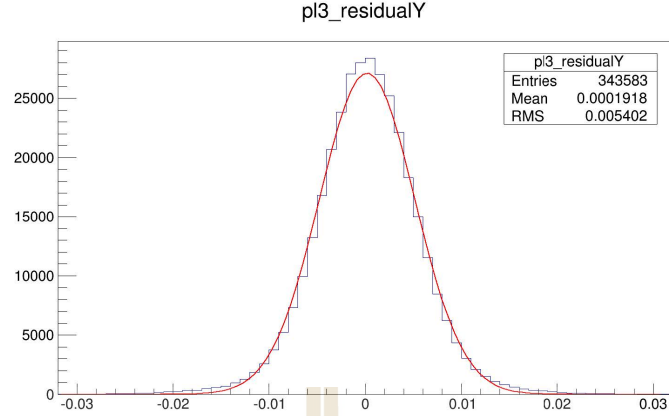
Figure 6.13 A residual plot for the third plane for a straight tracks. The distribution has been fitted with a Gaussian, and the resolution is given by the RMS value.

6.3.5 Position resolution

The resolution of the chip cannot be measured directly, only its residual, which also contains the uncertainty of the tracking. The residual (σ) has two contributions: the resolution of the chip (σ_{DUT}) and the uncertainty of the track interpolation to the DUT (σ_{track}). It can be written as the following

$$\sigma^2 = \sigma_{DUT}^2 + \sigma_{track}^2. \tag{6.6}$$

The interpolation uncertainty comes from two sources such as the scattering of the particles in the material of the telescope layers and the resolution of the telescope layers. It can be calculated from the simulations with the tracking plane resolution calculated from the iterative procedure. For the residual, it is measured by calculating the distance of the impinging point of the track to the associated hit in both the x and y direction. A typical distribution is then fitted with a Gaussian function in both directions.

The telescope settings used for the determination of the tracking uncer-

tainty was $V_{BB} = 0$ V, $I_{THR} = 30$ DAC units and $V_{CASN} = 57$ DAC units, and only tracks passing through the hole in the carrier card of the DUT were considered for resolution measurements. The estimation of the tracking uncertainty was done from the data taken at the PS with 6 GeV/c π^- particles.

6.4 Analysis results

In this section, the characterization of pALPIDEfs-3b of 25 µm thickness has been mentioned.

6.4.1 Detection efficiency and fake-hit rate

The detection efficiency has been used to present the performance of the non-irradiated chip. Figure 6.14–6.15 show the detection efficiency distribution as a function of I_{THR} with $V_{BB} = $ -3V and -6V. For both cases, detection efficiency is $\sim 100\%$ at the small value of I_{THR}. But for $V_{BB} = $ -3V, it decreases when increasing I_{THR}. Because the detection efficiency has an influenced on charge collection efficiency.

Figure 6.16–6.17 present the detection efficiency as a function of V_{CASN} with $V_{BB} = $ -3V and -6V respectively. The detection efficiency is significantly affected by the lower V_{CASN}. With the $V_{BB} = $ -3V, the detection efficiency decreases to 89% below the required value of 99% for low V_{CASN}. The higher value of V_{CASN} from 104 DAC can increase the detection efficiency exceeds 99%. For $V_{BB} = $ -6V, a detection efficiency increases to 99% hence the value of V_{CASN} is higher than 134 DAC.

For the fake-hit rate that refers to the number of fired pixels per events divided by the total number of pixels and the number of events. It is measured in the laboratory with DAQ scan (without beam) about 50000 events for each
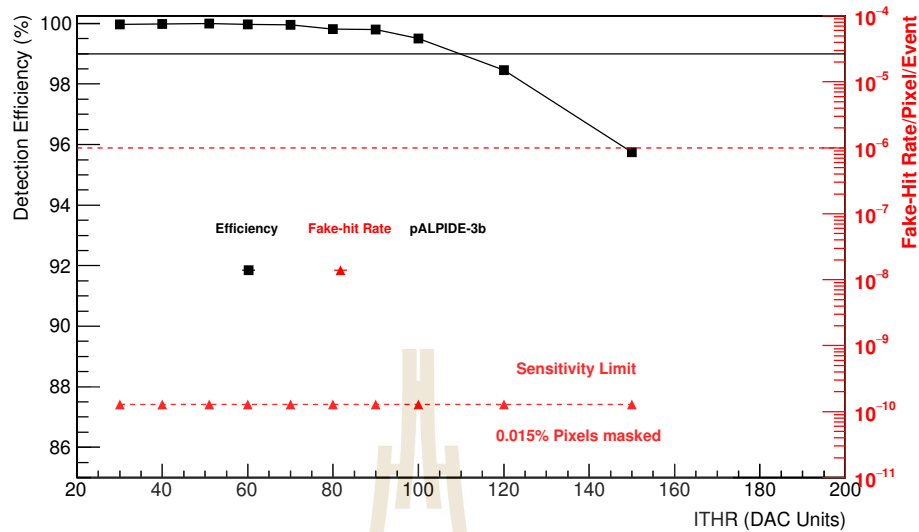
Figure 6.14 Detection efficiency and fake-hit-rate plotted with the increasing of I_{THR} with $V_{\text{BB}} = $ -3V.
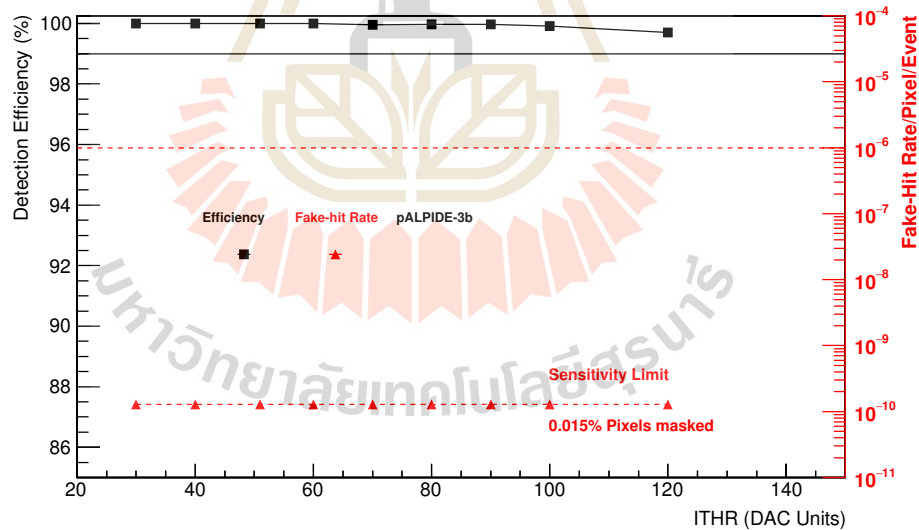
Figure 6.15 Detection efficiency and fake-hit-rate plotted with the increasing of I_{THR} with $V_{\text{BB}} = $ -6V.

run. Figure 6.14 presents a certain fake-hit rate as a function of I_{THR} with -3V of V_{BB} and nominal V_{CASN}. It has been observed that the minimum fake-hit rate of 10^{-9}/event/pixel can be obtained for all values of I_{THR}. The number of pixels
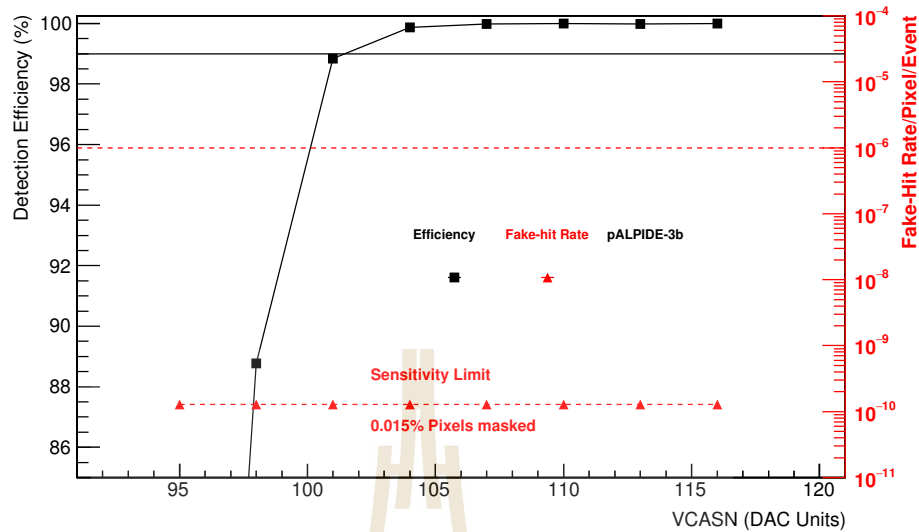
Figure 6.16 Detection efficiency and fake-hit-rate plotted with the increasing of V_{CASN} with V_{BB} = -3V.
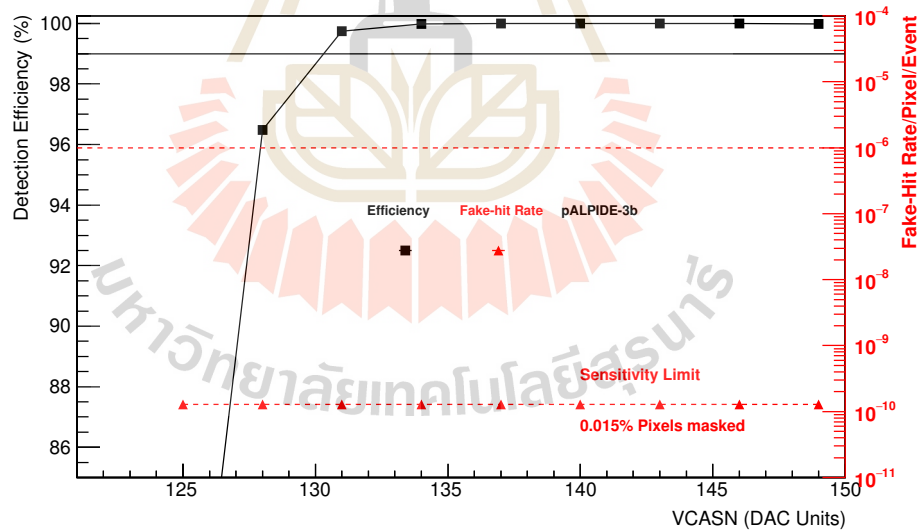
Figure 6.17 Detection efficiency and fake-hit-rate plotted with the increasing of V_{CASN} with V_{BB} = -6V.

masked in this measurement is only 0.015%.

The Fake-Hit rate as a function of I_{THR} at -6V of V_{BB} remains the same behavior of -3V, as shown in Figure 6.15. At the same number of masks less than

100 pixels (which is less than 1% of the pixels in a sector), the fake-hit rate can be reduced with the larger thresholds.

6.4.2 Position resolution and average cluster size

The spatial resolution of DUT has been evaluated from the residual distributions of the hits associated to a track. Figure 6.18–6.19 present a comparison of the position resolution and average cluster size as function of I_{THR} for two values of reverse substrate bias, each at nominal V_{CASN}. At V_{BB} = -3V, there are several different I_{THR} present the minimum resolution (~ 5 μm). The position resolution is below 5 μm for long range of I_{THR} at V_{BB} = -6V. However, the position resolution reaches 5 μm when cluster size is ~ 2 μm, similar for both reverse substrate bias.
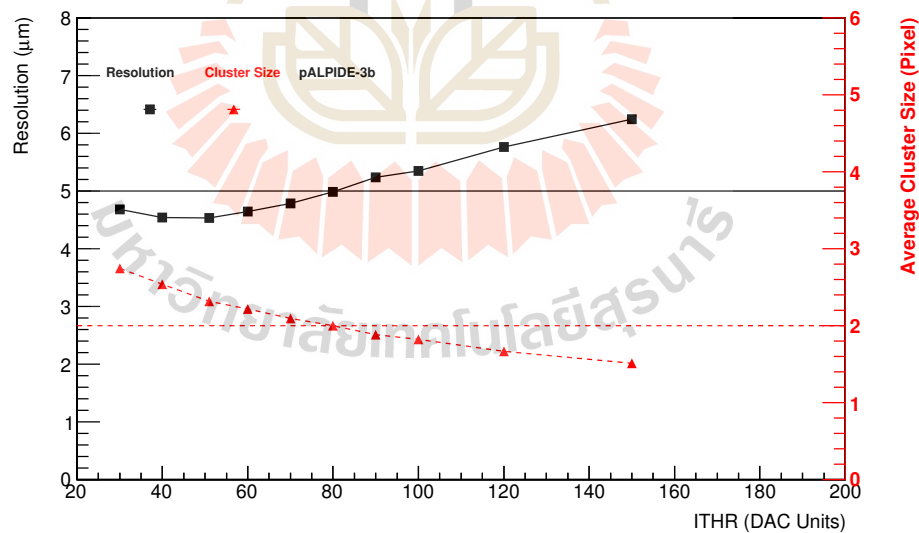
Figure 6.18 Spatial resolution and average cluster size plotted with the increasing of I_{THR} with V_{BB} = -3V.

For the influence of other V_{CASN}, the comparison between the position resolution and cluster size of DUT has been plotted as function of V_{CASN}. Fig-
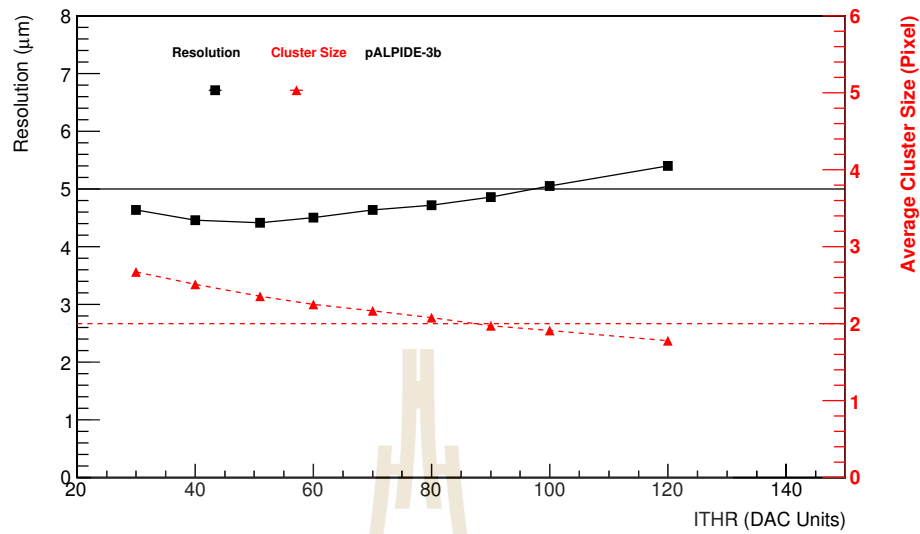
Figure 6.19 Spatial resolution and average cluster size plotted with the increasing of I_{THR} with 25 V_{BB} = -6V.

ure 6.20–6.21 present these comparison for two different reverse substrate bias, each at nominal I_{THR}.
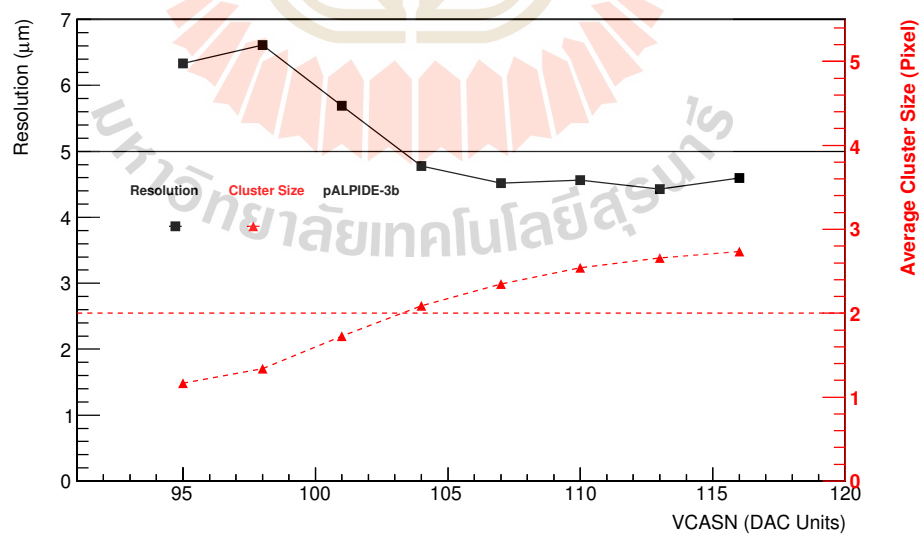
Figure 6.20 Spatial resolution and average cluster size plotted with the increasing of V_{CASN} with V_{BB} = -3V.

For V_{BB} = -3V, the results show a comparable performance in terms of
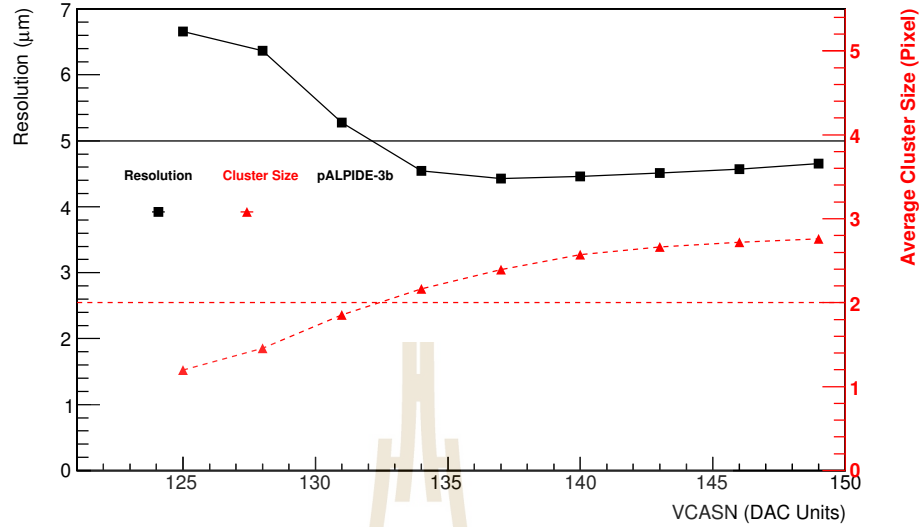
Figure 6.21 Spatial resolution and average cluster size plotted with the increasing of $V_{\rm CASN}$ with $V_{\rm BB} = $ -6V.

position resolution, which ranges between 7 μm for $V_{\rm CASN} = 95$ DAC counts and decreases to around 4.5 μm for $V_{\rm CASN}$ larger than ∼100 DAC counts. At this reverse substrate bias, the improved charge collection performance does not affect the position resolution. In this measurement, pALPIDE-3 performs well a position resolution below the required 5 μm after. Eventually, position resolution starts to drop at $V_{\rm CASN}$=115 because the fake-Hit rate increases with the increasing of $V_{\rm CASN}$. For the effect of increasing the reverse substrate bias, there are a small margin for the resolution due to the low threshold. The higher back bias also gives lot of margin in detection efficiency and Fake-hit rate.

The results show that the performance of the pALPIDE-3 in terms of the detection efficiency, position resolution, cluster size and fake-hit rate are in the required value as expected by the ALICE ITS upgrade.

6.5   Summary

In this section, the pALPIDE-3 pixel sensor is studied for the operational behavior of the analog part of the front-end on the effect of the two input bias parameters I_{THR} and V_{CASN}. The performance of the pixels can be obtained from the laboratory measurement and test beam measurement.

For the results from the laboratory measurement, I_{THR} and V_{CASN} are keys adjustable values for charge threshold. The threshold will be increased with the increase of I_{THR} or the decrease of V_{CASN} since the combinations of both parameters can be applied for the required threshold.

The improve of a reverse substrate bias voltage can increase the sensor performance, because it can increase Q/C ratio leads to the reducing of the charge threshold.

The fake-hit of pALPIDE-3 is very low depends on a small fraction of hot pixels. This underestimate results value of 10^{-6}/event/pixel can be reached for thresholds equivalent to $I_{\text{THR}} \gtrsim 40$ DAC counts and nominal V_{CASN} for $V_{\text{BB}} =$ -3V. Moreover, the rate below 10^{-9}/event/pixel can be exceeded for $I_{\text{THR}} \gtrsim 70$ DAC with 0.015% pixels masked.

For the test beam measurement, the detection efficiency, at $V_{\text{BB}} =$ -3V and nominal V_{CASN}, can be improved beyond 99% for $I_{\text{THR}} \lesssim 100$ DAC counts by an increase of V_{CASN} or the reverse substrate bias voltage. For $V_{\text{BB}} =$ -6V and nominal V_{CASN}, the detection efficiency is above 99% for all I_{THR} (assume up to $I_{\text{THR}} \approx 240$ DAC counts) while the fake-hit rate is lower than 10^{-6}/event/pixel with masking about 0.015% of the pixels. Moreover, this reverse bias voltage can perform 5.2 µm of the position resolution.

CHAPTER VII

CONCLUSION AND OUTLOOK

In this thesis, the implementation of the ALICE ITS and ALPIDE proto-type sensor characterization were taken into account. Using of lightweight carbon structure with polyimide cooling pipes can reduce the material budget. The ALI-ROOT simulation shows encouraging results for the estimation of the material budget to 0.3% per layer in the ITS stave prototype model 2. Therefore, it has been chosen for the final production of ITS upgrade. Although its material budget is not the lowest, it provides the optimal production cost and better thermal conductivity than other models. A completeness version of model 2 has been revised in model 4. Final version stave is currently ongoing for the production and assembly of the detector module (ALICE Collaboration, 2014a). The addition of an innermost layer and the use of smaller pixel size CMOS sensors can extend the coverage radius and perform the coverage pseudo-rapidity ($|\eta|$) $\leq$ 1.22. Adding a detection layer also provides continuous coverage for charged particle multiplicity measurement.

Pixel sensor prototypes used in the ITS upgrade were characterized with the laboratory test and the test beam. It manufactured by TowerJazz using the 180nm CMOS Imaging Sensor process. The observable results provide the expected performance of the upgraded ITS. The characterization of pALPIDE-3 prototypes carried out in this thesis provided the functionality operation in terms of the charge threshold and noise occupancy of bias front-end parameter dependence, I_{thr} and V_{CASN}. In other hands, the test beam measurement, The 6 GeV

proton beam has been used to verify the performance of the prototype. The results show that its detection efficiency can reach the upgrade required at 99%, fake-hit rate below 10^{-6} /pixel/event, and position resolution around 5 µm. pALPIDE-3 feature the high-speed readout, Diode/PMOS pixel resetting mechanism, and the multiple in-pixel hits that allowed shorter pulse widths and reducing the power consumption. Its advantage will be transferred to the implemented version in ALPIDE.

With the series of pALPIDE prototypes development, ALPIDE sensor became the final version used in the ITS Upgrade which will be installed during the second long shut down in 2019 and 2020. The performance of the prototypes has been performed with a 6 GeV proton beam, supplemented with laboratory tests for the noise occupancy. The prototypes show a detection efficiency, a fake hit rate, and a spatial resolution meet the requirement. The summary of the simulation for the ITS upgrade performance is shown in the Table 7.1.

Table 7.1 Simulation results compared with the upgraded ITS requirement.

Parameter	Requirement	Performed
Material Bdg. (inner)	0.3 %	0.303 %
Material Bdg. (outer)	0.813 %	0.816 %
Chip size (mm x mm)	15 x 30	15 x 30
Chip thickness (µm)	50	50
Spatial resolution (µm)	5	<5
Detection efficiency	>99%	>99%
Fake hit rate	$< 10^{-5}$ evt^{-1} pixel^{-1}	$< 10^{-9}$ evt^{-1} pixel^{-1}
Cluster size (µm)	> 2	> 2

Although pALPIDE-3 MAPS prototypes fulfill the requirements concerning detection efficiency, fake-hit rate, and position resolution, the idea to further reduce the material budget and facilities implementation are still considering. To reach the future goal, using of silicon-only Inner Barrel has been proposed. The electric

substrate and all power distribution will be removed and only four large chips would then be built a layer. The chips thickness would be thinned down to 50 µm allowing them to be bend to half-cylinders. The air flow will be taken as the cooling system which can reduce the overall material budget and eliminate the stave overlapping themselves. This idea is in the study available for the new commission.
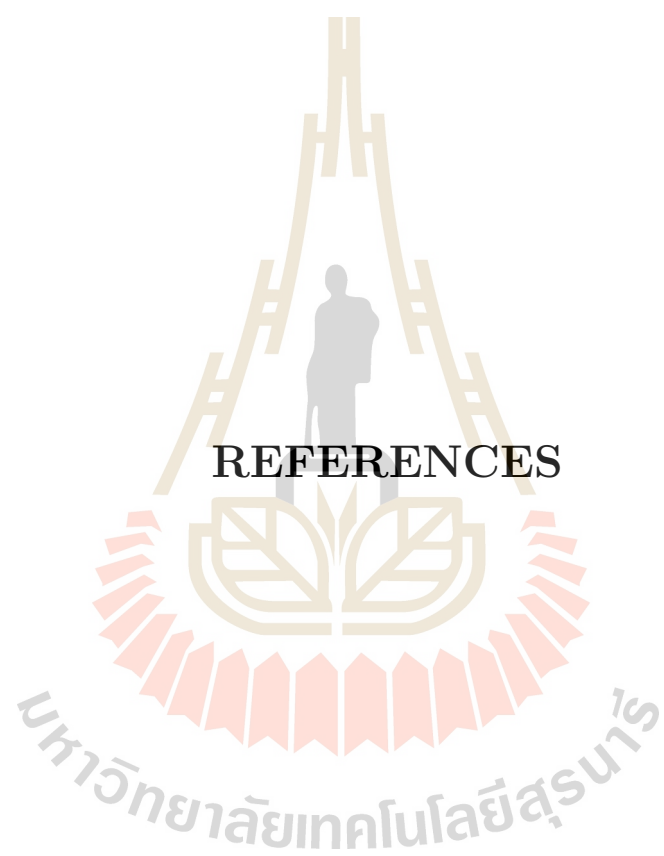
REFERENCES

REFERENCES

ALICE Collaboration (2012). Upgrade of the Inner Tracking System Conceptual Design Report. **Tech. Rep.** CERN-LHCC LHCC-P-005.

ALICE Collaboration (2014a). Technical Design Report for the Upgrade of the ALICE Inner Tracking System. **J. Phys.** G41: 087002.

ALICE Collaboration (2014b). Upgrade of the ALICE Experiment: Letter of Intent. Technical report.

Bé, M., Chisté, V., Dulieu, C., Mougeot, X., Chechev, V., Kondev, F., Nichols, A., Huang, X., and Wang, B. (2006). Table of Radionuclides. **Monographie BIPM** 5(3).

Beringer, J., Arguin, J. F., Barnett, R. M., and Copic, K. (2012). Review of Particle Physics. **Phys. Rev.** D86: 010001.

Berzano, D. (2015). Welcome to the home page of the ALICE Off-line Project [Online]. Available: http://http://alice-offline.web.cern.ch.

Besson, A., Pérez, A., Spiriti, E., Baudot, J., Claus, G., Goffe, M., and Winter, M. (2017). From vertex detectors to inner trackers with CMOS pixel sensors. **Nuclear Instruments and Methods in Physics Research Section** A845: 33–37.

Evans, L. (2009). The Large Hadron Collider : A Marvel of Technology. SEPFL Press/Lausanne 2009, 216p.

Gupta, M. (2010). Calculation of radiation length in materials. **PH-EP-Tech-Note-2010-013**.

Havránek, M., Hemperek, T., Krüger, H., and Fu, Y. (2015). DMAPS: a fully depleted monolithic active pixel sensor-analog performance characterization. **Journal of Instrumentation** 10(02): 02013.

Henke, B., Gullikson, E., and Davis, J. (1993). X-ray interactions: photoabsorption, scattering, transmission, and reflection at E=50-30000 eV, Z=1-92. **Atomic Data and Nuclear Data Tables** 54(2): 181—-342.

Hillemanns, H., Aimo, I., Bedda, C., Cavicchioli, C., Collu, A., Giubilato, P., Junique, A., Kugathasan, T., La Rocca, P., Mager, M., Marin Tobon, C., Martinengo, P., Mattiazzo, S., Musa, L., Pappalardo, G., Puggioni, C., Reidt, F., Riedler, P., Santagati, G., Siddhanta, S., Snoeys, W., and van Hoorne, J. (2013). Radiation hardness and detector performance of new 180nm CMOS MAPS prototype test structures developed for the upgrade of the ALICE Inner Tracking System. **IEEE Nuclear Science Symposium and Medical Imaging Conference**: 1–5.

Hu-Guo, C., Baudot, J., Bertolone, G., Besson, A., Claus, G., Colledani, C., Dorokhov, A., Doziere, G., Dulinski, W., Fang, X., Goffe, M., Himmi, A., Jaaskelainen, K., Morel, F., Senyukov, S., Specht, M., Szelezniak, M., Pham, H., Valin, I., Wang, T., and Winter, M. (2013). Development of the MISTRAL amp; ASTRAL sensors for the upgrade of the Inner Tracking System of the ALICE experiment at LHC. **IEEE Nuclear Science Symposium and Medical Imaging Conference** G37: 1–7.

Keil, M. (2014). pALPIDEfs software - Installation and command line interface. **rev.** 1.

Kofarago, M. (2015). Upgrade of the Inner Tracking System of ALICE. **arXiv:1511.08368**.

Kofarago, M. (2016). Summary of the test beam results of the pALPIDE-3. CERN public note, Switzerland.

Landau, L. (1944). On the energy loss of fast particles by ionization. **J. Phys.(USSR)** 8: 201–205.

Leo, W. R. (1987). **Techniques For Nuclear And Particle Physics Experiments**. Springer.

Mazur, R. and Dickey, D. (1966). A Spreading Resistance Technique for Resistivity Measurements in Si. **J. Electrochem. Soc.** 113: 255.

Nakamura, K., Hagiwara, K., Hikasa, K., and Murayama, H. (2010). Review of Particle Physics, 2010-2011. Review of Particle Properties. **J. Phys.** G37(7A): 075021.

Olive, K. A. (2014). Review of Particle Physics. **Chin. Phys.** C38: 090001.

Poonsawat, W., Kobdaj, C., Sitta, M., and Yan, Y. (2019). Stave module design and development of the new ALICE Inner Tracking System. **Journal of Instrumentation** 14(05): 05003.

Prabket, J., Poonsawat, W., Kobdaj, C., Naeosuphap, S., Yan, Y., Jeamsaksiri, W., Yamwong, W., Chaowicharat, E., Hruanun, C., and Poyai, A. (2019). Resistivity profile of epitaxial layer for the new ALICE ITS sensor. **Journal of Instrumentation** 14(05): 05006.

Rinella, G. (2017). The ALPIDE pixel sensor chip for the upgrade of the ALICE Inner Tracking System. **Nucl. Instrum. Meth.** A:583–587.

Rossegger, S. (2013). Upgrade of the ALICE inner tracking system. **Nucl. Instrum. Meth.** A731: 40–46.

Rossi, L., Fischer, P., Rohe, T., and Wermes, N. (2006). Pixel detectors: from fundamentals to applications.

Schambach, J., Anderssen, E. band Contin, G., Greiner, L., Silber, J., Stezelberger, T., Sun, X., Szelezniak, M., Videbaek, F., Vu, C., Wieman, H., and Woodmansee, S. (2015). A MAPS Based Micro-Vertex Detector for the STAR Experiment. **Physics Procedia** 66: 514–519.

Sentech Instruments (1994). Technical Handbook of the Spreading Resistance Measuring Desk SR 210. Berlin, Geramany.

Thompson, A. C., Attwood, T., Gullikson, M., Howells, R., Kortright, B., Robinson, L., and Underwood, H. (2001). *X-ray Data Booklet; 2nd ed.* Lawrence Berkeley National Laboratory, University of California, California.

Treberspurg, W., Bergauer, T., Dragicevic, M., Hrubec, J., Krammer, M., and Valentan, M. (2012). Measuring doping profiles of silicon detectors with a custom-designed probe station. **Journal of Instrumentation** 7 (11): 11009.

Valin, I., Hu-Guo, C., Baudot, J., Bertolone, G., Besson, A., Colledani, C., Claus, G., Dorokhov, A., Dozière, G., Dulinski, W., Gelin, M., Goffe, M., Himmi, A., Jaaskelainen, K., Morel, F., Pham, H., Santos, C., Senyukov, S., Specht, M., Voutsinas, G., Wang, J., and Winter, M. (2012). A reticle size CMOS pixel sensor dedicated to the STAR HFT. **JINST** 7(01): 01102.

van Hoorn, J. W. (2015). Study and Development of a novel Silicon Pixel Detector for the Upgrade of the ALICE Inner Tracking System. **CERN-THESIS-2015-255**.

van Hoorne, J. W., Krammer, M., and Riedler, P. (2015). Study and Development of a novel Silicon Pixel Detector for the Upgrade of the ALICE Inner Tracking System. PhD thesis, TU Vienna.

Xu, Z. and Ullrich, T. (2012). Treatment of Errors in Efficiency Calculations.
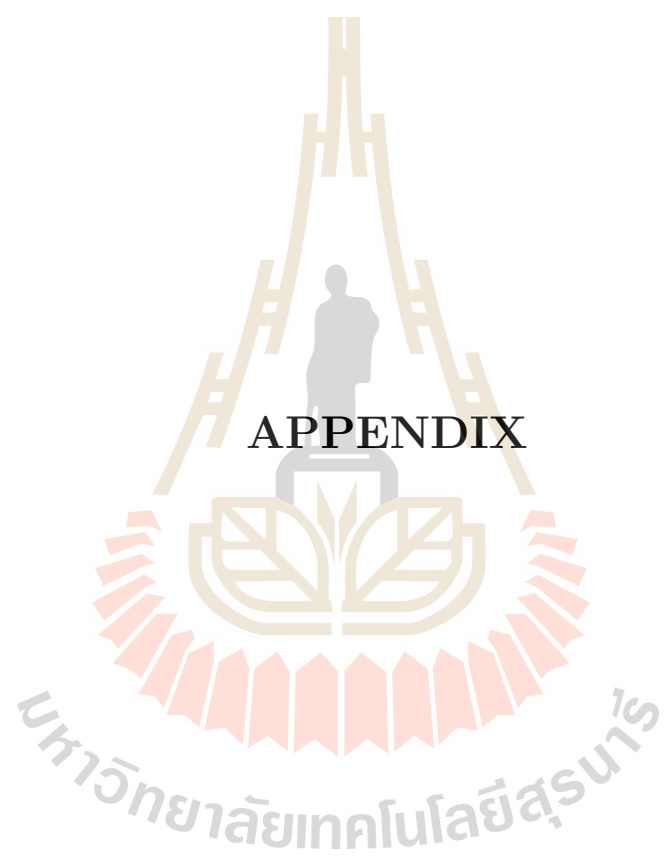
APPENDIX

APPENDIX

MANUSCRIPT PROGRAM ALIROOT

The Inner Barrel stave can be simulated with the ALICE Off-line framework, called AliRoot. It is the Off-line framework for simulation, reconstruction and analysis. Except for large existing libraries, such as GEANT3.21 and Jetset, and some remaining legacy code, this framework is based on the Object Oriented programming paradigm, and it is written in C++. To measure the material budget of the new ITS satve, the geometrical structure will be created with the following ALIROOT simulation code.

*Written by Mr.Wanchaloem Poonsawat

```
TGeoVolume* AliITSUv1Layer::CreateStaveModelInnerB22(const Double_t xsta,
                                                     const Double_t zsta,
                                                     const TGeoManager *mgr){

    // Materials defined in AliITSUv1
    TGeoMedium *medAir       = mgr->GetMedium("ITS_AIR$");
    TGeoMedium *medWater     = mgr->GetMedium("ITS_WATER$");

    TGeoMedium *medM60J3K       = mgr->GetMedium("ITS_M60J3K$");
    TGeoMedium *medKapton       = mgr->GetMedium("ITS_KAPTON(POLYCH2)$");
    TGeoMedium *medGlue         = mgr->GetMedium("ITS_GLUE$");
    TGeoMedium *medFlexCable    = mgr->GetMedium("ITS_FLEXCABLE$");
    TGeoMedium *medK13D2U2k     = mgr->GetMedium("ITS_K13D2U2k$");
    TGeoMedium *medFGS003       = mgr->GetMedium("ITS_FGS003$");
    TGeoMedium *medCarbonFleece = mgr->GetMedium("ITS_CarbonFleece$");

    // Local parameters
    Double_t kConeOutRadius =(0.1024+0.0025)/2;//0.107/2;
    Double_t kConeInRadius = 0.1024/2;//0.10105/2
    Double_t kStaveLength = zsta;
```

```
Double_t kStaveWidth = xsta*2;

Double_t kWidth = (kStaveWidth)/4;

Double_t kStaveHeight = 0.283;//0.33;

Double_t kHeight = (kStaveHeight)/2;

Double_t kAlpha = 57;//56.31;

Double_t kTheta = kAlpha*TMath::DegToRad();

Double_t kS1 = ((kStaveWidth)/4)/TMath::Sin(kTheta);

Double_t kL1 = (kStaveWidth/4)/TMath::Tan(kTheta);

Double_t kS2 = sqrt(kHeight*kHeight + kS1*kS1);//TMath::Sin(kThe2);

Double_t kThe2 = TMath::ATan(kHeight/(0.375-0.036));

Double_t kBeta = kThe2*TMath::RadToDeg();

Double_t klay1 = 0.003;//Amec carbon

Double_t klay2 = 0.002;//C Fleece carbon

Double_t klay3 = 0.007;//CFplate K13D2U carbon

Double_t klay4 = 0.007;//GluekStaveLength/2

Double_t klay5 = 0.01;//Flex cable

Double_t kTopVertexMaxWidth = 0.072;

Double_t kTopVertexHeight = 0.04;

Double_t kSideVertexMWidth = 0.052;

Double_t kSideVertexHeight = 0.11;


Int_t  loop = (Int_t)(kStaveLength/(2*kL1));


char volname[30];
snprintf(volname, 30, "%s%d_StaveStruct", AliITSUGeomTGeo::GetITSStavePattern(),
fLayerNumber);


Double_t z=0, y=-(2*kConeOutRadius)+klay1+klay2+fSensorThick/2-0.0004, x=0;


TGeoVolume *mechStavVol = 0;


if (fBuildLevel < 5) {
  // world (trapezoid)
  TGeoXtru *mechStruct = new TGeoXtru(2); //z sections
  Double_t xv[6] = {kStaveWidth/2,kStaveWidth/2,0.012,-0.012,-kStaveWidth/2,
  -kStaveWidth/2};
  Double_t yv[6] = {-(kConeOutRadius*2)-0.07295,0-0.02,kStaveHeight+0.01,
  kStaveHeight+0.01,0-0.02,-(kConeOutRadius*2)-0.07295};
  // (kConeOutRadius*2)-0.064
  mechStruct->DefinePolygon(6,xv,yv);
```

```
mechStruct−>DefineSection(0,−kStaveLength,0,0,1.);
mechStruct−>DefineSection(1,kStaveLength,0,0,1.);


mechStavVol = new TGeoVolume(volname, mechStruct, medAir);
mechStavVol−>SetLineColor(12);
mechStavVol−>SetFillColor(12);
mechStavVol−>SetVisibility(kTRUE);


//Polyimide Pipe Kapton grey−35
TGeoCone *cone1 = new TGeoCone(kStaveLength,kConeInRadius,
kConeOutRadius−0.0001,kConeInRadius,kConeOutRadius−0.0001);
TGeoVolume *volCone1= new TGeoVolume("PolyimidePipe", cone1, medKapton);
volCone1−>SetFillColor(35);
volCone1−>SetLineColor(35);
mechStavVol−>AddNode(volCone1,1,new TGeoTranslation(x+0.25,y,z));
mechStavVol−>AddNode(volCone1,2,new TGeoTranslation(x−0.25,y,z));
}


if (fBuildLevel < 4) {
TGeoTube *coolTubeW = new TGeoTube(0.,kConeInRadius−0.0001,kStaveLength);
TGeoVolume *volCoolTubeW= new TGeoVolume("Water", coolTubeW, medWater);
volCoolTubeW−>SetFillColor(4);
volCoolTubeW−>SetLineColor(4);
mechStavVol−>AddNode(volCoolTubeW,0,new TGeoTranslation(x−0.25,y,z));
mechStavVol−>AddNode(volCoolTubeW,1,new TGeoTranslation(x+0.25,y,z));
}


if (fBuildLevel < 3) {
//top fillament
// Top filament M60J black−12 Carbon structure TGeoBBox
(length,thickness,width)
TGeoBBox *t2=new TGeoBBox(kS2−0.028,0.02/2,0.02/2);
TGeoVolume *volT2=new TGeoVolume("TopFilament", t2, medM60J3K);
volT2−>SetLineColor(12);
volT2−>SetFillColor(12);
for(int i=0;i<loop;i++){// i<28;i++{
    // 1) Front Left Top Filament
    mechStavVol−>AddNode(volT2,i*4+1,new TGeoCombiTrans(x+kWidth+0.0036,
    y+kHeight+0.01,z−kStaveLength+0.1+(i*4*kL1)+kS1/2,
    new TGeoRotation("volT2",90,90−kAlpha,90−kBeta)));
```

```
// 2) Front Right Top Filament
mechStavVol->AddNode(volT2,i*4+2,new TGeoCombiTrans(x-kWidth-0.0036,
y+kHeight+0.01,z-kStaveLength+0.1+(i*4*kL1)+kS1/2,
new TGeoRotation("volT2",90,-90+kAlpha,-90+kBeta)));
// 3) Back Left   Top Filament
mechStavVol->AddNode(volT2,i*4+3,new TGeoCombiTrans(x+kWidth+0.0036,
y+kHeight+0.01,z-kStaveLength+0.1+2*kL1+(i*4*kL1)+kS1/2,
new TGeoRotation("volT2",90,-90+kAlpha,90-kBeta)));
// 4) Back Right Top Filament
mechStavVol->AddNode(volT2,i*4+4,new TGeoCombiTrans(x-kWidth-0.0036,
y+kHeight+0.01,z-kStaveLength+0.1+2*kL1+(i*4*kL1)+kS1/2,
new TGeoRotation("volT2",90,90-kAlpha,-90+kBeta)));
}


//Vertex   structure
//top ver trd1
TGeoTrd1 *trd1 = new TGeoTrd1(0,kTopVertexMaxWidth/2,kStaveLength,
kTopVertexHeight/2);
TGeoVolume *ibdv = new TGeoVolume("TopVertex",trd1,medM60J3K);
ibdv->SetFillColor(12);
ibdv->SetLineColor(12);
mechStavVol->AddNode(ibdv,1,new TGeoCombiTrans(x,y+kStaveHeight+0.03,z,
new TGeoRotation("ibdv",0.,-90,0)));//y+kStaveHeight+0.056


//left trd2
TGeoTrd1 *trd2 = new TGeoTrd1(0,kSideVertexMWidth/2,kStaveLength,
kSideVertexHeight/2);
TGeoVolume *ibdv2 = new TGeoVolume("LeftVertex",trd2,medM60J3K);
ibdv2->SetFillColor(12);
ibdv2->SetLineColor(12);
mechStavVol->AddNode(ibdv2,1,new TGeoCombiTrans(x+kStaveWidth/2-0.06,
y-0.0348,z,new TGeoRotation("ibdv2",-103.3,90,0)));


//right trd3
TGeoTrd1 *trd3 = new TGeoTrd1(0,kSideVertexMWidth/2,kStaveLength,
kSideVertexHeight/2);
TGeoVolume *ibdv3 = new TGeoVolume("RightVertex",trd3,medM60J3K);
ibdv3->SetFillColor(12);
ibdv3->SetLineColor(12);
mechStavVol->AddNode(ibdv3,1,new TGeoCombiTrans(x-kStaveWidth/2+0.06,
```

```
y−0.0348,z ,new TGeoRotation("ibdv3",103.3,90,0)));


//Carbon Fleece
 TGeoConeSeg *cons2 = new TGeoConeSeg(zsta ,kConeOutRadius+klay1 ,
 kConeOutRadius+klay1+klay2 ,kConeOutRadius+klay1 ,
 kConeOutRadius+klay1+klay2 ,0 ,180);
 TGeoVolume *cone12 = new TGeoVolume("CarbonFleecePipeCover",
 cons2 ,medCarbonFleece);
 cone12−>SetFillColor(28);
 cone12−>SetLineColor(28);
 mechStavVol−>AddNode(cone12 ,1 ,new TGeoCombiTrans(x+0.25,y,z,
 new TGeoRotation("cone12",0,0,0)));
 mechStavVol−>AddNode(cone12 ,2 ,new TGeoCombiTrans(x−0.25,y,z,
 new TGeoRotation("cone12",0,0,0)));


 TGeoBBox *box3 = new TGeoBBox((0.50−(2*(kConeOutRadius+klay1)))/2 ,
 klay2/2 ,zsta); //kStaveLength−0.50);
 TGeoVolume *plate3 = new TGeoVolume("CarbonFleeceMiddle",
 box3 ,medCarbonFleece);
 plate3−>SetFillColor(28);
 plate3−>SetLineColor(28);
 mechStavVol−>AddNode(plate3 ,1 ,new TGeoCombiTrans(x,
 y−kConeOutRadius+klay1+(klay2/2) ,z ,new TGeoRotation("plate3",0,0,0)));


 TGeoBBox *box31 = new TGeoBBox((0.75−0.25−kConeOutRadius−klay1)/2
 +0.0025,
 klay2/2 ,zsta);
 TGeoVolume *plate31 = new TGeoVolume("CarbonFleeceLeftRight",
 box31 ,medCarbonFleece);
 plate31−>SetFillColor(28);
 plate31−>SetLineColor(28);
 mechStavVol−>AddNode(plate31 ,1 ,new
 TGeoCombiTrans(x+0.25+kConeOutRadius+klay1+(0.75−0.25−kConeOutRadius
 −klay1)/2 ,
 y−kConeOutRadius+klay1+(klay2/2) ,z ,new TGeoRotation("plate31",0,0,0)));
 mechStavVol−>AddNode(plate31 ,2 ,new
 TGeoCombiTrans(x−0.25−kConeOutRadius−klay1 −(0.75−0.25−kConeOutRadius
 −klay1)/2 ,
 y−kConeOutRadius+klay1+(klay2/2) ,z ,new TGeoRotation("plate31",0,0,0)));
```

```
TGeoBBox *box32 = new TGeoBBox((klay2/2),(kConeOutRadius−klay1)/2,
zsta);
TGeoVolume *plate32 = new TGeoVolume("CarbonFleeceVertical",box32,
medCarbonFleece);
plate32−>SetFillColor(28);
plate32−>SetLineColor(28);
mechStavVol−>AddNode(plate32,1,new
TGeoCombiTrans(x+0.25+kConeOutRadius+klay1+(klay2/2),y+(klay1
−kConeOutRadius)/2,
z,new TGeoRotation("plate32",0,0,0)));
mechStavVol−>AddNode(plate32,2,new
TGeoCombiTrans(x+0.25−kConeOutRadius−klay1−(klay2/2),y+(klay1
−kConeOutRadius)/2,
z,new TGeoRotation("plate32",0,0,0)));
mechStavVol−>AddNode(plate32,3,new
TGeoCombiTrans(x−0.25+kConeOutRadius+klay1+(klay2/2),y+(klay1
−kConeOutRadius)/2,
z,new TGeoRotation("plate32",0,0,0)));
mechStavVol−>AddNode(plate32,4,new
TGeoCombiTrans(x−0.25−kConeOutRadius−klay1−(klay2/2),y+(klay1
−kConeOutRadius)/2,
z,new TGeoRotation("plate32",0,0,0)));


//Amec Thermasol red−2 cover tube FGS300 or Carbon Paper
TGeoConeSeg *cons1 = new TGeoConeSeg(zsta,kConeOutRadius,
kConeOutRadius+klay1 −0.0001, kConeOutRadius,kConeOutRadius+klay1
−0.0001,0,180);
TGeoVolume *cone11 = new TGeoVolume("ThermasolPipeCover",cons1,
medFGS003);
cone11−>SetFillColor(2);
cone11−>SetLineColor(2);
mechStavVol−>AddNode(cone11,1,new TGeoCombiTrans(x+0.25,y,z,
new TGeoRotation("cone11",0,0,0)));
mechStavVol−>AddNode(cone11,2,new TGeoCombiTrans(x−0.25,y,z,
new TGeoRotation("cone11",0,0,0)));


TGeoBBox *box2 = new TGeoBBox((0.50−(2*kConeOutRadius))/2,
(klay1/2),zsta); //kStaveLength−0.50);
TGeoVolume *plate2 = new TGeoVolume("ThermasolMiddle",box2,
medFGS003);
```

```
plate2->SetFillColor(2);
plate2->SetLineColor(2);
mechStavVol->AddNode(plate2,1,new TGeoCombiTrans(x,
y-kConeOutRadius+(klay1/2),z,new TGeoRotation("plate2",0,0,0)));


TGeoBBox *box21 = new TGeoBBox((0.75-0.25-kConeOutRadius-klay1)/2
+0.0025,
(klay1/2),zsta);
TGeoVolume *plate21 = new TGeoVolume("ThermasolLeftRight",box21,
medFGS003);
plate21->SetFillColor(2);
plate21->SetLineColor(2);
mechStavVol->AddNode(plate21,1,new
TGeoCombiTrans(x+0.25+kConeOutRadius+(0.75-0.25-kConeOutRadius)/2
-(klay1/2)+0.0025,
y-kConeOutRadius+(klay1/2),z,new TGeoRotation("plate21",0,0,0)));
mechStavVol->AddNode(plate21,2,new
TGeoCombiTrans(x-0.25-kConeOutRadius-(0.75-0.25-kConeOutRadius)/2
+(klay1/2)-0.0025,
y-kConeOutRadius+(klay1/2),z,new TGeoRotation("plate21",0,0,0)));


TGeoBBox *box22 = new TGeoBBox((klay1/2),kConeOutRadius/2,zsta);
TGeoVolume *plate22 = new TGeoVolume("ThermasolVertical",box22,
medFGS003);
plate22->SetFillColor(2);
plate22->SetLineColor(2);
mechStavVol->AddNode(plate22,1,new TGeoCombiTrans(x+0.25
+kConeOutRadius
+(klay1/2),
y-kConeOutRadius/2,z,new TGeoRotation("plate22",0,0,0)));
mechStavVol->AddNode(plate22,2,new TGeoCombiTrans(x+0.25
-kConeOutRadius
-(klay1/2),
y-kConeOutRadius/2,z,new TGeoRotation("plate22",0,0,0)));
mechStavVol->AddNode(plate22,3,new TGeoCombiTrans(x-0.25
+kConeOutRadius
+(klay1/2),
y-kConeOutRadius/2,z,new TGeoRotation("plate22",0,0,0)));
mechStavVol->AddNode(plate22,4,new TGeoCombiTrans(x-0.25
-kConeOutRadius
```

```
            −(klay1/2),
        y−kConeOutRadius/2,z,new TGeoRotation("plate22",0,0,0)));


    //K13D2U CF plate
        TGeoBBox *box1 = new TGeoBBox(2*kWidth,(klay3)/2,zsta);
        TGeoVolume *plate1 = new TGeoVolume("CFPlate",box1,medK13D2U2k);
        plate1−>SetFillColor(5);
        plate1−>SetLineColor(5);
        mechStavVol−>AddNode(plate1,1,new TGeoCombiTrans(x,y
        −(kConeOutRadius
        +(klay3/2)),
        z,new TGeoRotation("plate1",0,0,0)));


    //C Fleece bottom plate
        TGeoBBox *box6 = new TGeoBBox(2*kWidth,(klay2)/2,zsta);
        TGeoVolume *plate6 = new TGeoVolume("CarbonFleeceBottom",box6,
        medCarbonFleece);
        plate6−>SetFillColor(2);
        plate6−>SetLineColor(2);
        mechStavVol−>AddNode(plate6,1,new TGeoCombiTrans(x,y
        −(kConeOutRadius
        +klay3+(klay2/2)),
        z,new TGeoRotation("plate6",0,0,0)));

    }
if (fBuildLevel < 2) {
    //Glue klayers and kapton
    TGeoBBox *glue = new TGeoBBox(kStaveWidth/2, (klay4)/2, zsta);
        TGeoVolume *volGlue=new TGeoVolume("Glue", glue, medGlue);
        volGlue−>SetLineColor(5);
        volGlue−>SetFillColor(5);
        // mechStavVol−>AddNode(volGlue, 0, new TGeoCombiTrans(x,
        y−(kConeOutRadius+klay3+klay2+(klay4/2)), z, new
        TGeoRotation("",0, 0, 0)));
        mechStavVol−>AddNode(volGlue, 0, new TGeoCombiTrans(x,
        y−(kConeOutRadius+klay3+klay2+(klay4)/2)+0.00005, z, new
        TGeoRotation("",0, 0, 0)));
    }


    if (fBuildLevel < 1) {
```

```
    //Flex Cable or Bus
    TGeoBBox *kapCable = new TGeoBBox(kStaveWidth/2, klay5/2, zsta);
    TGeoVolume *volCable=new TGeoVolume("FlexCable", kapCable,
    medFlexCable);
    volCable->SetLineColor(28);
    volCable->SetFillColor(28);
    //      mechStavVol->AddNode(volCable, 0, new TGeoCombiTrans(x,
    y-(kConeOutRadius+klay3+klay2+klay4+fSensorThick+(klay5)/2)+0.0002,
    z, new TGeoRotation("",0, 0, 0)));
    mechStavVol->AddNode(volCable, 0, new TGeoCombiTrans(x,
    y-(kConeOutRadius+klay3+klay2+klay4+(klay5)/2), z, new
    TGeoRotation("",0, 0, 0)));
    }
  // Done, return the stave structe
  return mechStavVol;
}
```

CURRICULUM VITAE

NAME   Mr. Wanchaloem Poonsawat

DATE OF BIRTH   August 12, 1981

PLACE OF BIRTH   Prachuap Khiri Khan, Thailand

E-MAIL   nanodoon@yahoo.com

EDUCATION

Master of Science (2006 - 2009)

School of Physics, Institute of Science, Suranaree University of Technology, Nakhon Ratchasima, Thailand

Supervisor: Asst. Prof. Dr. Chinorat Kobdaj

Bachelor of Science (2000 - 2004)

Department of Physics, Faculty of Science, Kasetsart University, Thailand

Supervisor: Prof. Dr. Yupeng Yan